

















Chemodynamics of Boötes I with S^5 : Revised Velocity Gradient, Dark Matter Density, and Galactic Chemical Evolution Constraints

NATHAN R. SANDFORD ¹, TING S. LI ^{1,2,3}, SERGEY E. KOPOSOV ^{4,5}, KOHEI HAYASHI ^{6,7,8}, ANDREW B. PACE ⁹,
DENIS ERKAL ¹⁰, JO BOVY ^{1,2}, GARY S. DA COSTA ¹¹, LARA R. CULLINANE ¹², ALEXANDER P. JI ^{13,14,15},
KYLER KUEHN ¹⁶, DANIEL B. ZUCKER ¹⁷, GUILHERME LIMBERG ¹⁴, GUSTAVO E. MEDINA ^{1,2}, JOSHUA D. SIMON ¹⁸,
YONG YANG ¹⁹
(S^5 COLLABORATION)

¹*Department of Astronomy and Astrophysics, University of Toronto, 50 St. George Street, Toronto ON, M5S 3H4, Canada*

²*Dunlap Institute for Astronomy & Astrophysics, University of Toronto, 50 St George Street, Toronto, ON M5S 3H4, Canada*

³*Data Sciences Institute, University of Toronto, 17th Floor, Ontario Power Building, 700 University Ave, Toronto, ON M5G 1Z5, Canada*

⁴*Institute for Astronomy, University of Edinburgh, Royal Observatory, Blackford Hill, Edinburgh EH9 3HJ, UK*

⁵*Institute of Astronomy, University of Cambridge, Madingley Road, Cambridge CB3 0HA, UK*

⁶*National Institute of Technology, Sendai College, 4-16-1 Ayashi-Chuo, Sendai, Japan*

⁷*Astronomical Institute, Tohoku University, Aoba-ku, Sendai 980-8578, Japan*

⁸*ICRR, The University of Tokyo, Kashiwa, Chiba 277-8582, Japan*

⁹*Department of Astronomy, University of Virginia, 530 McCormick Road, Charlottesville, VA 22904, USA*

¹⁰*Department of Physics, University of Surrey, Guildford GU2 7XH, UK*

¹¹*Research School of Astronomy and Astrophysics, Australian National University, Canberra, ACT 2611, Australia*

¹²*Leibniz-Institut für Astrophysik Potsdam (AIP), An der Sternwarte 16, D-14482 Potsdam, Germany*

¹³*Department of Astronomy & Astrophysics, University of Chicago, 5640 S Ellis Avenue, Chicago, IL 60637, USA*

¹⁴*Kavli Institute for Cosmological Physics, University of Chicago, Chicago, IL 60637, USA*

¹⁵*NSF-Simons AI Institute for the Sky (SkAI), 172 E. Chestnut St., Chicago, IL 60611, USA*

¹⁶*Lowell Observatory, 1400 W Mars Hill Rd, Flagstaff, AZ 86001, USA*

¹⁷*School of Mathematical and Physical Sciences, Macquarie University, Sydney, NSW 2109, Australia*

¹⁸*Observatories of the Carnegie Institution for Science, 813 Santa Barbara St., Pasadena, CA 91101, USA*

¹⁹*Sydney Institute for Astronomy, School of Physics, A28, The University of Sydney, NSW 2006, Australia*

Submitted to ApJ

ABSTRACT

We combine new spectroscopic observations of the ultra faint dwarf galaxy (UFD) Boötes I (Boo I) from the Southern Stellar Stream Spectroscopic Survey (S^5) with ~ 15 years of archival spectroscopic data to create the largest sample of stellar kinematics and metallicities to date in any Milky Way UFD. Our combined sample includes 148 members extending out to ~ 7 half-light radii (r_h), including 24 newly confirmed members, 18 binary candidates, 15 RR Lyrae stars, and 92 [Fe/H] measurements. Using this larger and more spatially extended sample, we provide updated constraints on Boo I's systemic properties, including its radial population gradients. Properly accounting for perspective rotation effects in a UFD for the first time, we detect a 4σ line-of-sight velocity gradient of $1.2 \pm 0.3 \text{ km s}^{-1} r_h^{-1}$ aligned along Boo I's orbit and discuss its potential tidal origins. We also infer a metallicity gradient of $-0.10 \pm 0.02 \text{ dex } r_h^{-1}$ in agreement with previous studies. Using an axisymmetric Jeans model, we provide updated constraints on Boo I's dark matter density profile, which weakly favor a cusped ($\gamma = 1.0^{+0.5}_{-0.6}$) dark matter profile. Lastly, we re-analyze Boo I's metallicity distribution function with a one-zone galactic chemical evolution model and place new constraints on its rapid, inefficient star formation and strong galactic outflows.

Keywords: Dark Matter (353); Dwarf Galaxies (416); Galaxy chemical evolution (580); Local Group (929); Stellar Abundances (1577); Stellar Kinematics (1608); Stellar Populations (1622)

1. INTRODUCTION

Ultra faint dwarf galaxies (UFDs) are among the oldest ($\gtrsim 13$ Gyr), most metal-poor ($[\text{Fe}/\text{H}] \lesssim -2.0$), lowest mass ($M_* \lesssim 10^5 M_\odot$), and dark matter-dominated ($M/L \gtrsim 100$) galaxies in the local universe (e.g., [Simon 2019](#), and references therein). As a result, their stellar populations provide exquisite testing sites for a broad range of astrophysical topics including star formation in the early Universe (e.g., [Frebel & Norris 2015](#)), the nature of dark matter (e.g., [Bullock & Boylan-Kolchin 2017](#); [Battaglia & Nipoti 2022](#)), the role of stellar feedback in low-mass galaxy evolution (e.g., [Collins & Read 2022](#)), and hierarchical galaxy formation (e.g., [Frebel et al. 2010](#)).

In the last two decades, the number of known UFDs around the Milky Way (MW) has dramatically increased, in large part due to wide area imaging campaigns, including the Sloan Digital Sky Survey (SDSS; [York et al. 2000](#); e.g., [Belokurov et al. 2007](#)), the Dark Energy Survey (DES; [Abbott et al. 2018](#); e.g., [Bechtol et al. 2015](#)), the Dark Energy Camera Legacy Survey (DECaLS; [Dey et al. 2019](#); e.g., [Collins et al. 2022](#)), the DECam Local Volume Exploration survey (DELVE; [Drlica-Wagner et al. 2021](#); e.g., [Cerny et al. 2023](#)), and the Ultraviolet Near Infrared Optical Northern Survey (UNIONS; [Ibata et al. 2017](#); e.g., [Smith et al. 2023](#)). However, the majority of these systems are too distant and/or too faint for detailed spectroscopic studies of their stellar populations. UFDs with more than a dozen or so spectroscopic members are incredibly rare, which substantially inhibits analysis of the dynamic and chemical evolution.

As a relatively nearby ($d \sim 66$ kpc; [Dall’Ora et al. 2006](#)) and luminous ($M_V \sim -6$; [Muñoz et al. 2018](#)) UFD, Boötes I (Boo I) has been the subject of enormous observational investment since its early discovery in SDSS ([Belokurov et al. 2006](#)). Deep ground- and space-based imaging have revealed an ancient metal-poor stellar population with an extended and modestly eccentric morphology (e.g., [Okamoto et al. 2012](#); [Brown et al. 2014](#); [Roderick et al. 2016](#); [Muñoz et al. 2018](#); [Durbin et al. 2025](#)).

Meanwhile, spectroscopic observations of Boo I (e.g., [Muñoz et al. 2006](#); [Martin et al. 2007](#); [Norris et al. 2008, 2010b,a](#); [Lai et al. 2011](#); [Koposov et al. 2011](#); [Gilmore et al. 2013](#); [Ishigaki et al. 2014](#); [Frebel et al. 2016](#); [Jenkins et al. 2021](#); [Longeard et al. 2022](#); [Waller et al. 2023](#); [Walker et al. 2023](#)) have measured radial velocities and spectroscopic metallicities for ~ 90 and ~ 70 member stars respectively, which confirm Boo I as a dark matter-dominated ($\sigma_v = 5.1 \text{ km s}^{-1}$; $M/L \sim 400$), metal-poor ($[\text{Fe}/\text{H}] = -2.3$; $\sigma_{[\text{Fe}/\text{H}]} = 0.3$) galaxy ([Jenkins et al.](#)

[2021](#)). Spectroscopic samples of this size are extremely rare in UFDs, making Boo I a particularly valuable laboratory to test theories of dark matter and galaxy evolution in low-mass galaxies and the early Universe.

Boo I’s metallicity distribution function (MDF) as well as the individual elemental abundances of a handful of stars have been the subject of numerous galactic chemical evolution (GCE) studies, seeking to understand the baryonic processes at play during its short-lived episode of star formation (e.g., [Lai et al. 2011](#); [Gilmore et al. 2013](#); [Vincenzo et al. 2014](#); [Romano et al. 2015](#); [Webster et al. 2015](#); [Frebel et al. 2016](#); [Romano et al. 2019](#); [Lacchin et al. 2020](#); [Jenkins et al. 2021](#); [Rossi et al. 2024](#)). Similarly, Boo I’s stellar velocity dispersion has been used to infer its underlying dark matter content and constrain alternative dark matter models (e.g., [Pace & Strigari 2019](#); [Hayashi et al. 2021a,b](#); [Horigome et al. 2023](#)).

Combined with *Gaia* proper motions ([Gaia Collaboration et al. 2022](#)), Boo I’s systemic line-of-sight velocity place its time of infall into the MW as 7–10 Gyr ago (e.g., [Fillingham 2019](#); [Miyoshi & Chiba 2020](#); [Barmantloo & Cautun 2023](#)) with its most recent pericentric passage of 30–40 kpc occurring ~ 300 Myr ago (e.g., [Battaglia et al. 2022](#); [Pace et al. 2022](#)). Boo I’s orbit, in conjunction with its elongated morphology, extended stellar population, and internal dynamics suggest that Boo I is experiencing tidal disruption (e.g., [Roderick et al. 2016](#); [Muñoz et al. 2018](#); [Longeard et al. 2022](#); [Pace et al. 2022](#); see also [Muñoz et al. 2008](#)). However, others have argued that similar features could be indicative of a past dry merger event (e.g., [Koposov et al. 2011](#); [Frebel et al. 2016](#)).

Searching for additional clues to Boo I’s dynamical evolution in the galaxy’s outskirts, an increasing number of studies have undertaken searches for member stars at large radii (e.g., [Vivas et al. 2020](#); [Filion et al. 2020, 2022](#); [Longeard et al. 2022](#); [Waller et al. 2023](#); [Jensen et al. 2024](#); [Tau et al. 2024](#); [Pan et al. 2025](#)). Despite these observational investments, spectroscopic data in Boo I beyond ~ 3 half-light radii (r_h) remains sparse, and our understanding of the galaxy’s chemodynamics is largely limited to its central region.

In this paper, we build upon the existing wealth of observational data in Boo I, combining ~ 15 years of archival spectroscopic data with new data acquired with the Two-degree Field (2dF; [Lewis et al. 2002](#)) fiber-fed AAOmega spectrograph ([Sharp et al. 2006](#)) on the Anglo-Australian Telescope (AAT) as a part of the Southern Stellar Stream Spectroscopic Survey (S^5 ; [Li et al. 2019](#)). This expanded dataset, which extends from the inner half-light radius out to beyond 5 half-light radii and includes over 140 member stars and 90 spectroscopic

[Fe/H] measurements, provides valuable new insight into the chemodynamic evolution of this fossil galaxy.

This paper is organized as follows. In Section 2, we present the collection and analysis of new S^5 spectroscopic observations, the re-reduction of archival AAT observations, and the additional archival datasets analyzed in this paper. In Section 3, we leverage the long time baseline of these observations to identify new binary star systems in Boo I. In Section 4, we present our sample of new and recovered Boo I member stars and Boo I systemic properties inferred through Gaussian mixture modeling. Additional analysis and discussion of radial population trends in Boo I, including stellar velocity and metallicity gradients, are presented in Section 5. In Section 6, we present updated constraints on Boo I’s dark matter density profile using axisymmetric Jeans modeling, and in Section 7, we provide new constraints on the baryonic evolution of Boo I using an analytic galactic chemical evolution model. We summarize and conclude our analysis in Section 8.

2. DATA

2.1. S^5 AAT Observations

Observations of Boo I were obtained as part of S^5 (see Li et al. 2019 for survey details), which uses the dual-arm AAOmega spectrograph (Sharp et al. 2006) fed by the Two-degree Field (2dF; Lewis et al. 2002) fiber positioner facility on the 3.9 meter AAT. The standard S^5 observational setup employs the 580V (3700–5800 Å; $R \sim 1300$) and 1700D (8420–8820 Å; $R \sim 10,000$) AAOmega gratings to combine the metallicity sensitivity of the absorption feature-rich blue optical region with higher resolution calcium triplet (CaT) observations in the red optical for radial velocities. Boo I was observed using three 50-minute exposures of a single AAT pointing on both 2023 March 18 and 19.

When selecting targets in Boo I we first consider all stars from Pace et al. (2022) with membership probabilities `mem_fixed` > 0.1 or `mem_gauss_nospatial` > 0.1 as high priority targets¹. Then additional Boo I targets are selected based on the photometry, proper motions, and parallax from *Gaia* Data Release 3 (DR3; Gaia Collaboration et al. 2022) following the approach described in Li et al. (2019). The selection criteria are as follows: We remove nearby foreground stars by only selecting sources with

$$\varpi - 3\sigma_\varpi < 0, \quad (1)$$

where ϖ and σ_ϖ are the parallax measurements and uncertainties from *Gaia* DR3. A color-magnitude cut is applied by selecting stars within 0.15 magnitude of

either a 10 Gyr-old metal-rich ([Fe/H] = −1.4) or a 12.5 Gyr-old metal-poor ([Fe/H] = −2.2) Dotter isochrone (Dotter 2016). Lastly, we require targets have proper motions ($\mu_{\alpha*}$ and μ_δ)² satisfying

$$\begin{aligned} |\mu_{\alpha*} - \mu_{\alpha*,B}| &< \max(3\sigma_{\mu_{\alpha*}}, 1.0) \text{ mas yr}^{-1} \\ |\mu_\delta - \mu_{\delta,B}| &< \max(3\sigma_{\mu_\delta}, 1.0) \text{ mas yr}^{-1}, \end{aligned} \quad (2)$$

$$(3)$$

where $\mu_{\alpha*,B}$ and $\mu_{\delta,B}$ are the proper motions of Boo I as reported by Pace et al. (2022), and $\sigma_{\mu_{\alpha*}}$ and σ_{μ_δ} are the individual measurement uncertainties from *Gaia*.

The above selection criteria yield a sample of ~ 500 targets in the AAT field, which is used as input to the `configure` fiber allocation software (Miszalski et al. 2006). In total, we observed 320 targets in Boo I, of which 270 are classified as stars with good measurements by our reduction pipeline (i.e., `good_star` = True; Li et al. 2019). Of these, 139 have signal-to-noise (S/N) > 3 pixel^{−1} in the red arm and are used in our analysis.

2.2. Archival AAT Observations

Though the focus of this work is on new S^5 observations, we also consider earlier AAT observations of Boo I that are publicly available on the AAT archive. As summarized in Table 1, this includes ten 15–40 minute exposures taken over 3 nights in May 2006, 25 30-minute exposures taken over 4 nights in April 2007, and six 45-minute exposures taken over 3 nights in June 2020. The archival observations collected in 2006 and 2007 were first analyzed in Norris et al. (2010a) and utilized the 1700B (3700–4500 Å; $R \sim 3500$) and 1700D gratings, while the 2020 observations were first analyzed in Longeard et al. (2022, hereafter L22) and used the 580V and 1700D gratings (the same as S^5).

After applying the same selection cuts adopted for the S^5 observations (see Section 2.1), we are left with archival AAT spectra for 233 unique targets, of which 202 are classified as stars by our reduction pipeline. Of these, 90 have S/N > 3 pixel^{−1}, including 70 that overlap with the S^5 sample.

2.3. AAT Data Reduction and Analysis

The S^5 observations considered in this paper are reduced and analyzed as a part of the S^5 internal data release iDR3.7, which is scheduled to be the second S^5 public data release (DR2; T.S. Li et al. in prep.). As previously described in Ji et al. (2021) and Li et al. (2022), this data release features several improvements to the spectral fitting procedure of the first public data release (DR1; Li et al. 2019). Here, we briefly summarize the most substantial improvements to the pipeline

¹ `mem_fixed` is the membership probability when the background model used by Pace et al. (2022) is fixed to the proper motion distribution of stars at large radii, while `mem_gauss_nospatial` is the membership probability when the background model uses a multivariate Gaussian distribution with free proper motion dispersion terms.

² $\mu_{\alpha*} = \mu_\alpha \cos \delta$

Table 1. AAT/AAOmega-2dF Observations in Boo I

Field	Gratings	Date	Exposures	Reference
BOO-AAT	1700B, 1700D	2006-05-23	1000s, 3×1800 s	Norris et al. (2010a)
BOO-AAT	1700B, 1700D	2006-05-25	3×2000 s	Norris et al. (2010a)
BOO-AAT	1700B, 1700D	2006-05-29	3×2500 s	Norris et al. (2010a)
BOO-AAT-1	1700B, 1700D	2007-04-18	7×1800 s	Norris et al. (2010a)
BOO-AAT-1	1700B, 1700D	2007-04-19	6×1800 s	Norris et al. (2010a)
BOO-AAT-1	1700B, 1700D	2007-04-20	6×1800 s	Norris et al. (2010a)
BOO-AAT-1	1700B, 1700D	2007-04-22	6×1800 s	Norris et al. (2010a)
Field210.0214.5135	580V, 1700D	2020-06-16	2×2700 s	Longeard et al. (2022)
Field210.0214.5135	580V, 1700D	2020-06-17	2×2700 s	Longeard et al. (2022)
Field210.0214.5135	580V, 1700D	2020-06-19	2×2700 s	Longeard et al. (2022)
BootesI-field-0	580V, 1700D	2023-03-18	3×3000 s	This work
BootesI-field-0	580V, 1700D	2023-03-19	3×3000 s	This work

below and refer the reader to the upcoming DR2 paper for a more thorough description of the pipeline and its validation.

As in DR1, the data is analyzed using the `rvspecfit` pipeline (Koposov 2019), which forward-models the stellar spectrum using the PHOENIX-2.0 stellar spectra library (Husser et al. 2013) to determine the radial velocity and stellar parameters (T_{eff} , $\log g$, and $[\text{Fe}/\text{H}]$) of each star. The first notable improvement in this pipeline over DR1 is that we now simultaneously model both the red and blue spectral arms of AAOmega as well as observations taken across multiple nights (with appropriate consideration for the heliocentric corrections). This change substantially improves the recovery of radial velocity measurements for stars observed across multiple nights, especially those near the $\text{S/N} \sim 3 \text{ pixel}^{-1}$ threshold. Another major improvement in this data release is the use of a neural-network interpolator to interpolate the PHOENIX model spectra grid. This substantially alleviates the “gridding” issues of previous releases where the measured parameters tended to cluster around grid points in T_{eff} , $\log g$, and $[\text{Fe}/\text{H}]$.

We reduce and analyze the archival AAT observations (see Section 2.2) similarly to the S^5 observations. This includes applying the measurement calibrations previously determined in Li et al. (2019) of:

$$v_{\text{cal}} = v_{\text{raw}} - 1.11 \text{ km s}^{-1}, \quad (4)$$

$$\sigma_{v,\text{cal}} = [(1.28\sigma_{v,\text{raw}})^2 + 0.66^2]^{1/2}, \text{ and} \quad (5)$$

$$\sigma_{[\text{Fe}/\text{H}],\text{cal}} = 1.3\sigma_{[\text{Fe}/\text{H}],\text{raw}}, \quad (6)$$

where the “raw” and “cal” subscripts refer to the measurements and measurement uncertainties reported directly by `rvspecfit` and those calibrated by analysis of repeat observations, respectively.

For the individual epoch measurements used to identify binary stars in Section 3, we perform a similar reduction except that we only simultaneously model the spectra that were acquired in the same AAT “field” (see Table 1). Because observations in each field were all acquired within a few days, this approach should be suitable for long-period binaries but may lead to unexpected results for binaries with periods on the order of a week or less.

2.4. Literature Datasets

To supplement our observations further, we also consider published datasets from Jenkins et al. (2021, hereafter J21) and Walker et al. (2023, hereafter W23) respectively. The dataset from J21 includes $[\text{Fe}/\text{H}]$ and radial velocity measurements for ~ 70 likely Boo I member stars, which was constructed from a re-analysis of multi-epoch FLAMES/GIRAFFE spectroscopy originally observed by Koposov et al. (2011, hereafter K11) on the Very Large Telescope (VLT). Because of smaller field-of-view of the FLAMES fiber positioner, this sample is nearly entirely located within Boo I’s inner half-light radius. The dataset from W23 includes $[\text{Fe}/\text{H}]$ and radial velocity measurements for ~ 100 red giant branch stars within ~ 0.5 degrees ($\sim 3r_h$) of Boo I from multi-epoch Hectochelle spectroscopy on the MMT. Because W23 does not assign membership probabilities to the stars in their catalog, we identify likely members in this dataset following the same methodology that we adopt for the S^5 and archival AAT datasets.

2.5. Creating a Combined Dataset

Throughout this work, we focus our analysis primarily on two datasets: an S^5 -only dataset, which contains only new S^5 AAT observations taken in 2023, and a “combined” dataset, which includes re-reduced archival

AAT observations, archival MMT measurements from W23, and archival VLT measurements from J21. We limit the combined dataset to high-probability Boo I member stars as determined using a Gaussian mixture model applied to S^5 data (see Section 4) and archival AAT and MMT data (see Appendix B). Member stars for the archival VLT data are taken directly from J21. For stars appearing in multiple datasets, we combine velocity and metallicity measurements and uncertainties using a weighted mean after applying a zero-point correction to each dataset (see Section 3).

2.6. Simulation Dataset

To aid in the dynamical interpretation of our observational data described above, we also consider a mock sample of stars generated from an N -body simulation of Boo I. To generate this dataset, we use GADGET-3, an improved version of the GADGET-2 N -body simulation code (Springel 2005), to simulate the dynamical evolution of a Boo I-mass galaxy on a Boo I-like orbit through a Milky Way-like gravitational potential.

We initialize the phase-space coordinate of the simulated Boo I by rewinding a tracer particle 3.3 Gyr from Boo I’s present-day location through the combined potential of the MW and the Large Magellanic Cloud (LMC). We choose this time since this corresponds to Boo I’s apocenter and because it experiences two pericenters between this time and the present day, allowing for it to be tidally stripped. We model the MW using the MWPotential2014 potential from Bovy (2015). For the LMC, we use a Hernquist profile (Hernquist 1990) with a mass of $1.5 \times 10^{11} M_\odot$ and a scale radius of 17.13 kpc so that the enclosed mass of the LMC within 8.7 kpc matches the observed value of $1.7 \times 10^{10} M_\odot$ (van der Marel & Kallivayalil 2014). The total LMC mass is based on the results of previous fits of the LMC mass with stellar streams (Erkal et al. 2019; Shipp et al. 2021; Vasiliev et al. 2021; Koposov et al. 2023). For the present-day phase-space coordinates of the LMC, we use measurements of its proper motion, distance, and radial velocity from Kallivayalil et al. (2013); Pietrzyński et al. (2019); van der Marel et al. (2002), respectively. We also include the effect of dynamical friction on the LMC from the MW using the prescription in Jethwa et al. (2016).

We model Boo I using a Plummer sphere (Plummer 1911) embedded in an NFW profile using AGAMA (Vasiliev 2019). For the Plummer sphere, we use a mass of $4.81 \times 10^3 M_\odot$, a scale radius of 0.19 kpc, and 10^6 particles, and a softening of 10.1 pc. For the NFW, we use a mass of $10^8 M_\odot$, a concentration of $c_{200} = 21.2$ from Dutton & Macciò (2014), and a Hubble value of $H_0 = 67.9 \text{ km s}^{-1} \text{ Mpc}^{-1}$ (consistent with observations, Planck Collaboration et al. 2020) to set the present-day critical density of the Universe. To avoid artificially extended profiles, we truncate both profiles with an exponential cutoff in density, which is implemented in agama by setting `outerCutoffRadius` to ten times the scale

radius (1.9 kpc) for the Plummer sphere and to the virial radius (9.77 kpc) for the NFW profile (Vasiliev 2019). After evolving the system to the present day, the simulated galaxy is only slightly offset from the correct present-day location of Boo I by 0.02 kpc in heliocentric distance, 0.7° (0.81 kpc) in the plane of the sky, and 3.2 km s^{-1} in velocity.

In order to be able to easily compare to our observed data, we downsample the N -body simulation to approximately match the number and radial distribution of Boo I member stars identified in the S^5 dataset (see Section 4.3). We do this by splitting the sample of simulated stars into 4 elliptical annuli: $r/r_h < 1$, $1 \leq r/r_h < 3$, $3 \leq r/r_h < 5$, and $5 \leq r/r_h < 8$. In each annulus we randomly draw the number of samples equal to the number of S^5 member stars within that annulus. We repeat this sampling 10 times and perform our dynamical analysis on each.

The full results of the N -body simulation are illustrated in Figure 1. Extended tidal features are clearly visible along the galaxy’s orbit. The orientation of these tidal features is similar, though not identical, to the observed position angle of Boo I, which is just slightly misaligned eastward of the galaxy’s orbit. The 10 bootstrapped samples are included as color points in Figure 1.

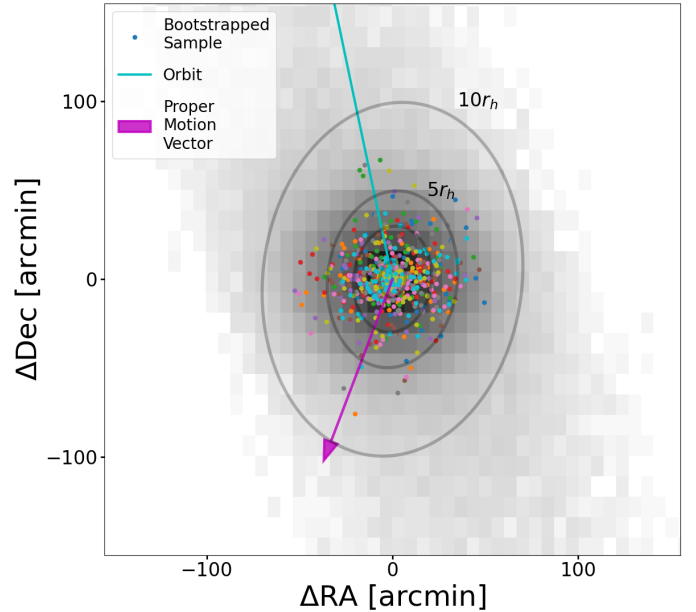


Figure 1. The log-number density of the Boo I N -body simulation. The simulated orbit and apparent proper motion (without Solar reflex correction) of the system are represented by the cyan line and magenta arrow respectively. Ten bootstrapped mock samples are included as colored points. Gray ellipses indicate the observed 1, 3, 5, and 10 half-light radii of Boo I from Muñoz et al. (2018).

3. BINARY IDENTIFICATION

The presence of binary stars in a galaxy, if unaccounted for, can inflate the observed velocity dispersion through their additional orbital motion. This would make a galaxy appear more massive than it truly is and complicate other dynamical analyses. Previous studies by K11 and J21 identified several binaries in Boo I using multi-epoch VLT spectroscopy. However, the time baseline of these observations was only ~ 1 month, limiting the sensitivity of the binary search to systems with $\lesssim 1$ year periods.

We extend this binary search to longer periods by combining our new S^5 observations with archival AAT observations (see Section 2.2) and previously published datasets from VLT and MMT observations (see Section 2.4). This combined dataset contains measurements for ~ 600 stars over a 16-year time span. Roughly one third of these stars were observed more than once, and $\sim 5\%$ were observed between five and 9 times. Fifteen stars previously identified as RR Lyrae (RRL) stars in Clementini et al. (2023) are excluded from this analysis.

Similar to previous binary searches (e.g., Spencer et al. 2017, 2018), we perform null-hypothesis significance testing for each star in our sample with multiple velocity epochs. Here the null hypothesis is that each star has constant velocity and the reduced chi-squared statistic is given by

$$\chi^2_\kappa = \frac{1}{\kappa} \sum_i^n \left(\frac{v_i - \langle v \rangle}{\sigma_i} \right)^2, \quad (7)$$

where $\kappa = n - 1$ is the number of degrees of freedom, n is the number of observations, v_i and σ_i are the individual epoch velocity and velocity uncertainty respectively, and $\langle v \rangle$ is the velocity averaged across all epochs. If the probability, $P(\chi^2, \kappa)$, of exceeding this χ^2_κ for a star given the null hypothesis (i.e., the p -value) is very small ($\lesssim 0.01$), then we can confidently reject the null hypothesis of constant velocity and declare the star a likely binary.

We proceed with binary identification iteratively, first finding all stars with at least weak evidence of variability, $P(\chi^2, \kappa) < 0.1$. These are then temporarily removed from the sample in order to determine the relative zero-point velocity offsets between the datasets, which are calculated using the weighted average velocity differences of shared non-variable stars. We then re-calculate the p -values using the complete sample with applied velocity offsets, and re-determine the zero-point offsets. This process is repeated until the number of candidate binaries and the velocity offsets converge. Metallicity offsets for each archival dataset relative to S^5 are determined analogously from the $[\text{Fe}/\text{H}]$ measurements of shared stars. The zero-points for each dataset and the number of stars used to determine each offset are summarized in Table 2. The final p -value and binary classification for each star is included in Table A1.

Table 2. Offsets Between Datasets

Dataset	Δv (km s $^{-1}$)	$\Delta[\text{Fe}/\text{H}]$	N_*
AAT (BOO-AAT)	0.00	-0.12	10
AAT (BOO-AAT-1)	-0.09	0.02	30
AAT (Field210.0214.5135)	0.00	-0.19	20
VLT	0.14	0.00	10
MMT	-0.26	-0.28	41

NOTE— Velocity and metallicity offsets (Δv and $\Delta[\text{Fe}/\text{H}]$) of each dataset relative to S^5 as well as the number of overlapping stars used in the offset calculations, N_* . Potential binary stars and RR Lyrae were excluded when determining the offsets.

In Figure 2, we show the velocity curves for the 16 sources in our sample, with $P(\chi^2, \kappa) < 0.1$ and $\langle v \rangle$ within ± 50 km s $^{-1}$ of Boo I's systemic velocity. Nine of these sources show strong evidence of velocity variability, $P(\chi^2, \kappa) \leq 0.01$, while seven of these sources show only weak evidence, $0.01 < P(\chi^2, \kappa) < 0.1$. Of the 9 sources with strong evidence for binarity, 8 are newly identified. The ninth, *Gaia* ID 1230834620833562624³, was first identified as a potential binary using individual epoch VLT data over a 4-month baseline by K11 but was later discounted as such in a reanalysis of the data by J21. We believe that this source is a long-period binary, which is why its detection in VLT data is uncertain. This hypothesis is corroborated by preliminary analysis of recent MIKE observations (J. Simon, private communication). We attempt to fit the orbits of these likely binaries using the *Joker*⁴ (Price-Whelan et al. 2017) but are unable to place meaningful constraints on any orbital parameters due to the sparse sampling of the velocity curves.

The seven sources with weak evidence for velocity variability have, on average, fewer and/or less precise measurements. For the three stars with VLT observations, *Gaia* sources 1230849425585454720, 1230847089123220224, and 1230836368884839296⁵, both K11 and J21 previously found no evidence of variability. It is possible that these sources are also in long-period binaries, but additional observations are required to confirm or reject this. We also note that 1230847089123220224 has a mean velocity of ~ 143 km s $^{-1}$, which compared with Boo I's systemic velocity of

³ Source Boo1_30 in K11 and J21.

⁴ <https://thejoker.readthedocs.io/en/latest/index.html>

⁵ Sources Boo1_14, Boo1_20, and Boo1_73 respectively in K11 and J21.

103 km s^{-1} (Jenkins et al. 2021; Longeard et al. 2022) makes its association with Boo I somewhat tenuous.

In Figure 2, we also include the velocity curve of *Gaia* source 1230831597176581248⁶, which was identified as a weak binary candidate based on VLT data in K11 and J21. Preliminary analysis of recent MIKE observations also indicates weak evidence for binarity (J. Simon, private communication). However, we do not find any evidence for velocity variability based on our combined dataset. Additional epochs of high-precision velocity measurements will prove useful in addressing this disagreement. Erring on the side of caution, we treat this star as a binary in our dynamical analysis of Boo I.

Not shown in Figure 2 are three binary candidates identified by J21: *Gaia* IDs 1230853376955406848, 1230833860623898496, and 1230783626686364672⁷. While these three sources were observed with AAT, the acquired spectra do not meet our $S/N > 3$ pixel $^{-1}$ quality cut, and thus do not appear in this analysis.

4. MEMBERSHIP MODELING AND SYSTEMIC PROPERTIES

In this section, we present the identification of Boo I member stars in our S^5 sample and the inference of Boo I's systemic chemodynamic properties. We describe the final quality cuts made to our S^5 dataset in Section 4.1 and introduce the adopted Gaussian mixture model (GMM) and sampling techniques in Section 4.2. We present the results of our analysis, including likely members and systemic properties in Sections 4.3 and 4.4. In Appendix B, we apply the same fitting techniques to the archival AAT and MMT datasets individually and compare those results to the fiducial S^5 -only and combined results.

4.1. Data and Quality Cuts

For the purposes of this analysis, our dataset includes spectroscopic measurements of stellar metallicities, heliocentric line-of-sight (l.o.s.) velocities, and their respective uncertainties ($[Fe/H]$, $\sigma_{[Fe/H]}$, v , σ_v) as well as proper motions, their uncertainties, and their correlation coefficients from *Gaia* DR3 ($\mu_{\alpha*}$, μ_{δ} , $\sigma_{\mu_{\alpha*}}$, $\sigma_{\mu_{\delta}}$, $C_{\mu_{\alpha*}, \mu_{\delta}}$). We also consider the stars' distance from the center of Boo I, r , and the stars' positions along and perpendicular to the axis of Boo I's systemic proper motion, ϕ_{1*} and ϕ_{2*} (not to be confused with their positions along the major and minor axes, ϕ_1 and ϕ_2 .) The structural parameters adopted for these coordinate transformations are summarized together with the inferred parameters from the combined dataset in Table 3.

⁶ Source Boo1_111 in K11 and J21.

⁷ Sources Boo1_26, Boo1_61, and Boo1_114 respectively in K11 and J21.

In addition to requiring all stars to have 1700D spectra with median $S/N > 3$ pixel $^{-1}$ and valid *Gaia* proper motions, we also require all stars to have $|v| < 600$ km s^{-1} . We also require that the *Gaia* renormalized unit weight error (RUWE) and the *Gaia* astrometric excess noise satisfy the conditions **ruwe** < 1.4 and **astrometric_excess_noise** < 2 respectively.

As previously implemented in S^5 studies (e.g., Ji et al. 2021), we require $\sigma_v < 10$ km s^{-1} and $\sigma_{[Fe/H]} < 0.5$ dex as larger uncertainties are frequently indicative of spectral fits impacted by large sky subtraction residuals. Instead of removing these stars entirely, we inflate both their metallicity and velocity uncertainties by an arbitrarily large amount in order to effectively mask out these measurements while still considering the star's proper motion.

Lastly, we account for binary, horizontal branch (HB), and RRL stars in our sample. Binary candidates identified in Section 3 as well as any stars identified as RRL in Clementini et al. (2023) have their velocity uncertainties increased by an arbitrarily large amount so that they do not artificially inflate the inferred velocity dispersion of Boo I. Similarly, we inflate the metallicity uncertainties of all RRL and HB stars in our sample because the metallicities measured by RVSpecFit are less reliable for hotter and variable stars. As a result of this treatment, HB stars contribute only to the proper motion and line-of-sight velocity determination of Boo I, and RRL only contribute to the proper motion determination.

4.2. Gaussian Mixture Model

We determine stellar membership and systemic properties of Boo I using a two-component GMM with one component representing Boo I's stellar population and one component representing MW foreground contaminants. GMMs have been applied extensively over the last ~ 15 years to numerous stellar streams, dwarf galaxies, and other resolved stellar systems (e.g., Koposov et al. 2011; Martinez et al. 2011; Walker & Peñarrubia 2011; Pace et al. 2014; Walker et al. 2016; Caldwell et al. 2017; Pace et al. 2020; Awad et al. 2025; Yang et al. 2025). We direct the interested readers to Pace et al. (2020) for a well-written and detailed description of the methodology.

In brief, the likelihood of a star in our sample can be written as mixture of its likelihood of belonging in the Boo I (\mathcal{L}_B) or MW (\mathcal{L}_{MW}) component of the GMM:

$$\mathcal{L}(\mathbf{D}_i|\theta) = f_B \mathcal{L}_B(\mathbf{D}_i|\theta_B) + (1 - f_B) \mathcal{L}_{MW}(\mathbf{D}_i|\theta_{MW}), \quad (8)$$

where f_B is the fraction of stars in the dataset that are members of Boo I, θ_B and θ_{MW} are the model parameters describing the metallicity, velocity, and proper motion distributions of Boo I and the MW foreground components respectively. Here, \mathbf{D}_i represents the measured quantities of the star in our dataset as described

Table 3. Boo I Systemic Properties

Parameter	Value	Description	Reference
Literature Properties			
α [deg]	210.02	Boo I center RA	Muñoz et al. (2018)
δ [deg]	14.51	Boo I center Dec	Muñoz et al. (2018)
μ [mag]	19.11 ± 0.08	Distance modulus	Dall’Ora et al. (2006)
d [kpc]	$66.4^{+2.5}_{-2.4}$	Distance	Dall’Ora et al. (2006)
r_h [arcmin]	9.97 ± 0.27	Circularized half-light Radius	Muñoz et al. (2018)
b_* [pc]	191 ± 8	Physical Half-light Radius	Muñoz et al. (2018)
$e = (1 - b/a)$	0.30 ± 0.03	Ellipticity	Muñoz et al. (2018)
θ_{PA} [deg]	6 ± 3	Position Angle (East of North)	Muñoz et al. (2018)
Inferred Properties			
$v_{0,B}$ [km s $^{-1}$]	$103.0^{+0.4}_{-0.4}$	Boo I central heliocentric l.o.s. velocity	Section 4.4
$\Delta v_{1,B}$ [km s $^{-1}$ arcmin $^{-1}$]	$0.02^{+0.03}_{-0.03}$	Heliocentric l.o.s. velocity gradient along ϕ_{1*}	Sections 4.4, 5.1
$\Delta v_{2,B}$ [km s $^{-1}$ arcmin $^{-1}$]	$-0.08^{+0.05}_{-0.05}$	Heliocentric l.o.s. velocity gradient along ϕ_{2*}	Sections 4.4, 5.1
$\sigma_{v,B}$ [km s $^{-1}$]	$4.0^{+0.4}_{-0.3}$	Heliocentric l.o.s. velocity dispersion	Sections 4.4, 5.2
$[\text{Fe}/\text{H}]_{0,B}$ [dex]	$-2.28^{+0.05}_{-0.05}$	Boo I central metallicity	Section 4.4
$\Delta[\text{Fe}/\text{H}]_B$ [dex arcmin $^{-1}$]	$-0.010^{+0.003}_{-0.003}$	Radial metallicity gradient	Sections 4.4, 5.3
$\sigma_{[\text{Fe}/\text{H}],B}$ [dex]	$0.28^{+0.03}_{-0.03}$	Metallicity dispersion	Sections 4.4, 5.3
$\langle\mu_{\alpha,*}\rangle_B$ [mas yr $^{-1}$]	$-0.38^{+0.02}_{-0.02}$	Boo I heliocentric proper motion (RA cos δ)	Section 4.4
$\langle\mu_\delta\rangle_B$ [mas yr $^{-1}$]	$-1.08^{+0.01}_{-0.01}$	Boo I heliocentric proper motion (Dec)	Section 4.4
$C_{\langle\mu_{\alpha,*}\rangle, \langle\mu_\delta\rangle}$	-0.08	Correlation between inferred $\langle\mu_{\alpha,*}\rangle_B$ and $\langle\mu_\delta\rangle_B$	Section 4.4
Additional Derived Properties			
$N_{\text{mem},v}$	115	Number of member stars with good velocities	Section 4.3
$N_{\text{mem},[\text{Fe}/\text{H}]}$	92	Number of member stars with good [Fe/H]	Section 4.3
$\langle v_B \rangle$ [km s $^{-1}$]	$103.0^{+0.4}_{-0.4}$	Boo I mean heliocentric l.o.s. velocity	Section 4.4
$\langle[\text{Fe}/\text{H}]_B\rangle$ [dex]	$-2.43^{+0.04}_{-0.04}$	Boo I mean metallicity	Section 4.4
Δv_B [km s $^{-1}$ arcmin $^{-1}$]	$0.09^{+0.05}_{-0.05}$	Magnitude of observed velocity gradient	Section 5.1
$\Delta v'_{1,B}$ [km s $^{-1}$ arcmin $^{-1}$]	$-0.09^{+0.03}_{-0.03}$	Intrinsic l.o.s. velocity gradient along ϕ_{1*}	Section 5.1
$\Delta v'_{2,B}$ [km s $^{-1}$ arcmin $^{-1}$]	$-0.08^{+0.05}_{-0.05}$	Intrinsic l.o.s. velocity gradient along ϕ_{2*}	Section 5.1
$\Delta v'_B$ [km s $^{-1}$ arcmin $^{-1}$]	$0.12^{+0.04}_{-0.03}$	Magnitude of intrinsic velocity gradient	Section 5.1
Dark Matter Properties			
Q	$1.18^{+0.51}_{-0.59}$	Axial ratio of dark matter halo	Section 6
$\log_{10} b_{\text{halo}}$ [pc]	$3.07^{+0.87}_{-0.45}$	Scale radius of dark matter halo	Section 6
$\log_{10} \rho_0 [M_\odot \text{ pc}^{-3}]$	$-1.88^{+0.90}_{-1.51}$	Central density of dark matter halo	Section 6
$-\log_{10}(1 - \beta_z)$	$0.25^{+0.21}_{-0.21}$	Velocity anisotropy parameter	Section 6
α	$1.76^{+0.82}_{-0.81}$	Sharpness of dark matter slope transition	Section 6
β	$6.39^{+2.20}_{-2.12}$	Outer slope of dark matter halo	Section 6
γ	$1.00^{+0.52}_{-0.60}$	Inner slope of dark matter halo	Section 6
i [deg]	$70.47^{+12.83}_{-13.23}$	Inclination angle	Section 6
GCE Properties			
τ_{SFH} [Gyr]	$0.2^{+0.1}_{-0.1}$	Star formation history timescale	Section 7
τ_{SFE} [Gyr]	$13.9^{+7.6}_{-5.3}$	Star formation efficiency timescale	Section 7
t_{trunc} [Gyr]	> 0.5	Time of star formation truncation	Section 7
η	203^{+27}_{-36}	Mass-loading factor	Section 7

NOTE— Selected properties of Boo I from the literature and inferred from our analysis of the combined dataset. Analogous results from the individual datasets are presented in Table 5. The “intrinsic” velocity gradients are the velocity gradients corrected for perspective rotation effects (see Section 5.1). For a discussion of the difference between central and mean systemic velocities and metallicities, see Section 4.4.

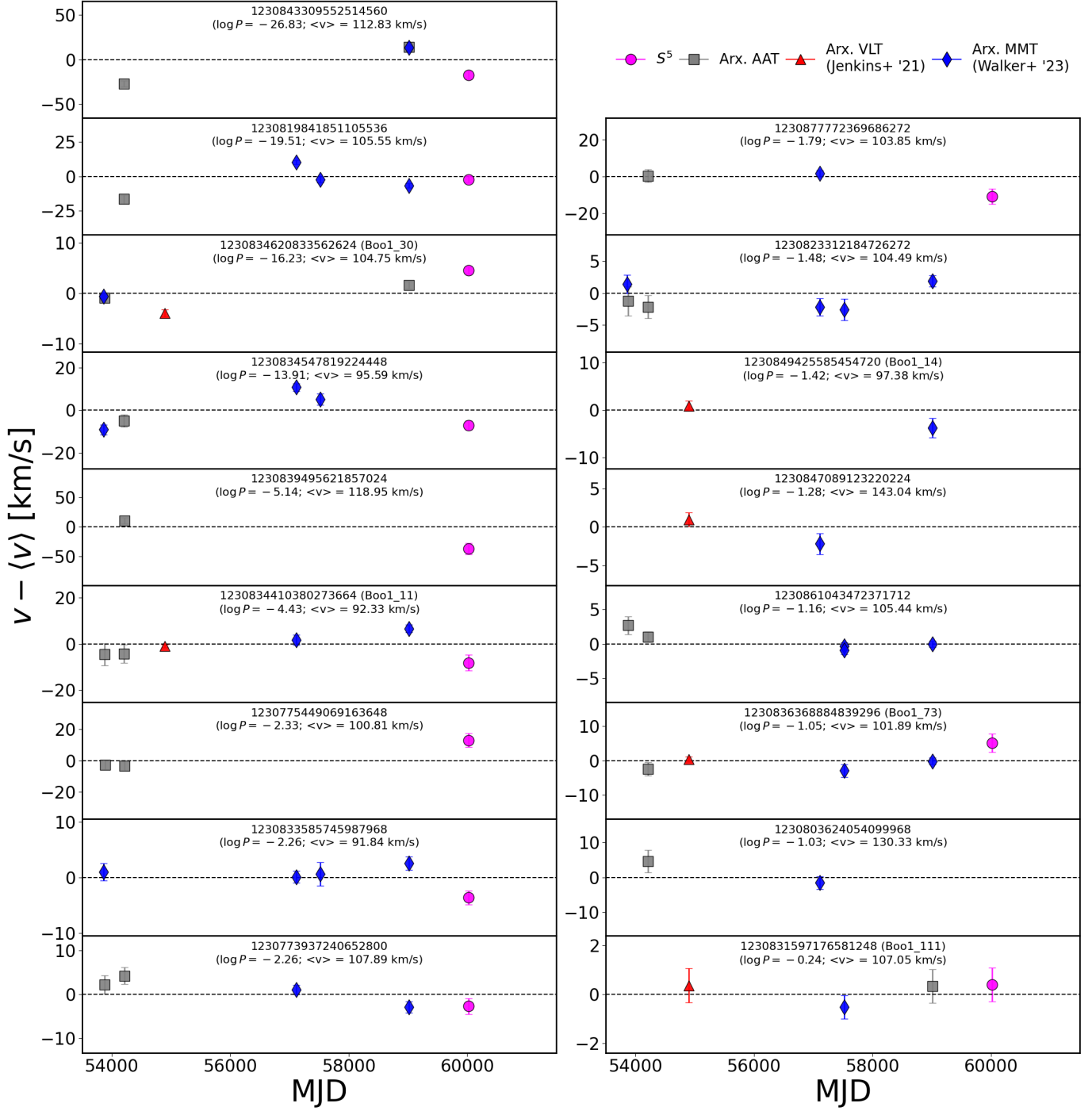


Figure 2. Difference between individual epoch velocity measurements and the mean velocity as a function of time for each of the potential Boo I binary stars in our combined sample. The stars are ordered by decreasing p -value. Star 1230831597176581248 (Boo1_111) is included despite its low binary probability because there is weak evidence of binarity from individual epoch VLT (Koposov et al. 2011; Jenkins et al. 2021) and MIKE observations (J. Simon, private communication).

in Section 4.1. In turn, the probability that a star in the sample belongs to Boo I (as opposed to the MW foreground) is

$$p_{\text{BooI},i} = \frac{f_B \mathcal{L}_B}{f_B \mathcal{L}_B + (1 - f_B) \mathcal{L}_{\text{MW}}}, \quad (9)$$

where the dependence on \mathbf{D}_i and θ have been dropped for brevity.

Under the reasonable assumption that each measurement in our dataset is independent, the total likelihood of our stellar sample given the model is the product of all individual star likelihoods,

$$\mathcal{L}(\mathbf{D}|\theta) = \prod_{i=1}^{N_*} \mathcal{L}(\mathbf{D}_i|\theta). \quad (10)$$

Similarly, if the metallicity, velocity, and proper motion probability distributions are all independent of one another, then the component likelihoods in Equation 8 can be expressed as a product of the three distributions,

$$\mathcal{L}_B(\mathbf{D}_i|\theta_B) = \mathcal{P}_B^{\text{vel}} \mathcal{P}_B^{[\text{Fe}/\text{H}]} \mathcal{P}_B^{\text{PM}} \quad (11)$$

and

$$\mathcal{L}_{\text{MW}}(\mathbf{D}_i|\theta_{\text{MW}}) = \mathcal{P}_{\text{MW}}^{\text{vel}} \mathcal{P}_{\text{MW}}^{[\text{Fe}/\text{H}]} \mathcal{P}_{\text{MW}}^{\text{PM}}. \quad (12)$$

We model the probability distribution of stellar heliocentric l.o.s. velocities in Boo I as a 2D linear function of position along and perpendicular to its on-sky projected direction of motion, ϕ_{1*} and ϕ_{2*} , with Gaussian dispersion:

$$\mathcal{P}_B^{\text{vel}} = \mathcal{N}\left(v_i|v_B(\phi_{1*,i}, \phi_{2*,i}), \sqrt{\sigma_{v,i}^2 + \sigma_{v,B}^2}\right), \quad (13)$$

where $\mathcal{N}(x|\mu, \sigma)$ represents a normal distribution with mean, μ , and standard deviation, σ , evaluated at x . Here the systemic velocity as a function of location is

$$v_B(\phi_{1*}, \phi_{2*}) = \Delta v_{1,\text{BooI}} \phi_{1*} + \Delta v_{2,\text{BooI}} \phi_{2*} + v_{0,B}. \quad (14)$$

In this parameterization, $v_{0,B}$ is the central velocity of Boo I, $\Delta v_{1,\text{BooI}}$ and $\Delta v_{2,\text{BooI}}$ are the components of the velocity gradient along and perpendicular to Boo I's proper motion direction respectively, and $\sigma_{v,B}$ is the intrinsic velocity dispersion. This parameterization differs slightly from that used in previous studies of velocity gradients where the velocity distribution is modeled as a 1D linear function along a free angle (e.g., Ji et al. 2021). We find that Equation 14 produces similar results to the previous parameterization but yields better-behaved (i.e., Gaussian) posteriors. The choice to set the velocity components along ϕ_{1*} and ϕ_{2*} rather than the major and minor axes of Boo I was driven by the expectation that perspective rotation would dominate the observed velocity gradient (see Section 5.1) but does not meaningfully impact the results.

We model the probability distribution of stellar metallicities in Boo I as a linear function of elliptical radius, r , with Gaussian dispersion:

$$\mathcal{P}_B^{[\text{Fe}/\text{H}]} = \mathcal{N}\left([\text{Fe}/\text{H}]_i | [\text{Fe}/\text{H}]_B(r_i), \sqrt{\sigma_{[\text{Fe}/\text{H}],i}^2 + \sigma_{[\text{Fe}/\text{H}],B}^2}\right), \quad (15)$$

where the systemic metallicity as a function of radius is

$$[\text{Fe}/\text{H}]_B(r) = \Delta[\text{Fe}/\text{H}]_B r + [\text{Fe}/\text{H}]_{0,B}. \quad (16)$$

Here the probability distribution is parameterized by the central metallicity of Boo I, $[\text{Fe}/\text{H}]_{0,B}$, its radial metallicity gradient, $\Delta[\text{Fe}/\text{H}]_B$, and its intrinsic dispersion, $\sigma_{[\text{Fe}/\text{H}],B}$. We experimented with non-Gaussian shapes for the metallicity distribution function and found no substantial change to the recovered members or systemic metallicity properties.

Lastly for Boo I, we adopt a bivariate Gaussian proper motion distribution:

$$\mathcal{P}_B^{\text{PM}} = \mathcal{N}_2(\mu_{\alpha*,i}, \mu_{\delta,i} | \langle \mu_{\alpha*} \rangle_B, \langle \mu_{\delta} \rangle_B, \text{Cov}_i), \quad (17)$$

where $\mathcal{N}_2(\mu_1, \mu_2, \text{Cov})$ represents a bivariate normal distribution with means, μ_1 and μ_2 , and covariance matrix, Cov . In this case, the covariance matrix is a combination of measured proper motion uncertainties and correlated errors, $\sigma_{\mu_{\alpha*}}, \sigma_{\mu_{\delta}}$, and $C_{\mu_{\alpha*}, \mu_{\delta}}$, and intrinsic proper motion dispersions, $\sigma_{\mu_{\alpha*},B}$ and $\sigma_{\mu_{\delta},B}$:

$$\text{Cov}_i = \begin{pmatrix} \sigma_{\mu_{\alpha*},i}^2 + \sigma_{\mu_{\alpha*},B}^2 & C_{\mu_{\alpha*}, \mu_{\delta},i} \sigma_{\mu_{\alpha*},i} \sigma_{\mu_{\delta},i} \\ C_{\mu_{\alpha*}, \mu_{\delta},i} \sigma_{\mu_{\alpha*},i} \sigma_{\mu_{\delta},i} & \sigma_{\mu_{\delta},i}^2 + \sigma_{\mu_{\delta},B}^2 \end{pmatrix}. \quad (18)$$

Boo I's proper motion probability distribution is thus parameterized by its mean systemic proper motions, $\langle \mu_{\alpha*} \rangle_B$ and $\langle \mu_{\delta} \rangle_B$, and its intrinsic dispersions, $\sigma_{\mu_{\alpha*},B}$ and $\sigma_{\mu_{\delta},B}$.

The probability distributions for the MW foreground component are simpler in comparison. We assume 1D Gaussian distributions for both the stellar velocity and metallicity distributions of the MW foreground:

$$\mathcal{P}_{\text{MW}}^{\text{vel}} = \mathcal{N}(v_i - \langle v \rangle_{\text{MW}}, \sqrt{\sigma_{v,i}^2 + \sigma_{v,\text{MW}}^2}) \quad (19)$$

and

$$\mathcal{P}_{\text{MW}}^{[\text{Fe}/\text{H}]} = \mathcal{N}\left([\text{Fe}/\text{H}]_i - \langle [\text{Fe}/\text{H}] \rangle_{\text{MW}}, \sqrt{\sigma_{[\text{Fe}/\text{H}],i}^2 + \sigma_{[\text{Fe}/\text{H}],\text{MW}}^2}\right) \quad (20)$$

where $\langle v \rangle_{\text{MW}}$ and $\langle [\text{Fe}/\text{H}] \rangle_{\text{MW}}$ are the mean velocity and metallicity of the foreground, and $\sigma_{v,\text{MW}}$ and $\sigma_{[\text{Fe}/\text{H}],\text{MW}}$ are the velocity and metallicity dispersions of the foreground. Finally, we assume the foreground has a uniform proper motion distribution.

In total, the fiducial GMM has 16 parameters: 11 for the Boo I component, $\theta_B = \{v_{0,B}, \Delta v_{1,B}, \Delta v_{2,B}, \sigma_{v,B}, [\text{Fe}/\text{H}]_{0,B}, \Delta[\text{Fe}/\text{H}]_B, \sigma_{[\text{Fe}/\text{H}],\text{BooI}}, \langle\mu_{\alpha*}\rangle_B, \langle\mu_\delta\rangle_B, \sigma_{\mu_{\alpha*},B}, \sigma_{\mu_\delta,B}\}$, 4 for the MW foreground component, $\theta_{\text{MW}} = \{\langle v\rangle_{\text{MW}}, \sigma_{v,\text{MW}}, \langle[\text{Fe}/\text{H}]\rangle_{\text{MW}}, \sigma_{[\text{Fe}/\text{H}],\text{MW}}\}$, and 1 describing the membership fraction: f_B . We aim to infer all of these parameter models with the exception of Boo I’s intrinsic proper motion dispersions, which is unresolved given current *Gaia* DR3 measurement uncertainties. Instead, we assume that radial and tangential velocity dispersions of Boo I are approximately equal, and set the proper motion dispersions in terms of the heliocentric l.o.s. velocity dispersion as

$$\sigma_{\mu_{\alpha*},B} [\text{mas yr}^{-1}] = \sigma_{\mu_\delta,B} = \frac{\sigma_{v,B}}{4.74d}, \quad (21)$$

where d is the heliocentric distance to Boo I in kpc (66.3 kpc; Dall’Ora et al. 2006). For all other model parameters, we adopt weakly informative or uninformative priors, which are summarized in Table 4. Together, the product of these 14 priors with the likelihood function presented in Equation 8 provides the posterior distribution of model parameters.

To sample this posterior distribution, we employ the *Preconditioned Monte Carlo* (PMC) method for Bayesian inference implemented in the publicly available Python package `pocoMC`⁸ (Karamanis et al. 2022a,b), which uses a combination of a normalizing flow with a sequential Monte Carlo sampling scheme to decorrelate and efficiently sample high-dimensional distributions with non-trivial geometry. We adopt default hyperparameters for `pocoMC` and run the sampler until it has converged (i.e., when the “inverse temperature” $\beta = 1$) and reached an effective sample size of 5,000 samples.

4.2.1. Non-mixture Model for the Combined and N -body Datasets

As described previously in Section 2.5, we also consider in our analysis a combined dataset that includes member stars from S^5 (presented in Section 4.3), member stars from the archival AAT and MMT datasets (presented in Appendix B), and member stars from the archival VLT dataset (presented in J21). The decision to combine the datasets after membership determination was driven by large differences in the targeting strategy of each observing program, which complicates modeling the MW foreground across all datasets.

Assuming all stars in the combined dataset are members, we can model the systemic properties of Boo I using just the Boo I likelihood given in Equation 11

Table 4. Free Model Parameters and Priors

Parameter	Prior
Gaussian Mixture Model	
f_{mem}	$\mathcal{U}(0, 1)$
$v_{0,B}$	$\mathcal{N}(100 \text{ km s}^{-1}, 10 \text{ km s}^{-1})$
$\Delta v_{1,B}$	$\mathcal{U}(-20 \text{ km s}^{-1} \text{ deg}^{-1}, 20 \text{ km s}^{-1} \text{ deg}^{-1})$
$\Delta v_{2,B}$	$\mathcal{U}(-20 \text{ km s}^{-1} \text{ deg}^{-1}, 20 \text{ km s}^{-1} \text{ deg}^{-1})$
$\log_{10}(\sigma_{v,B})$	$\mathcal{U}(0.0, 1.3)$
$[\text{Fe}/\text{H}]_{0,B}$	$\mathcal{N}(-2.4, 1.0)$
$\Delta[\text{Fe}/\text{H}]_B$	$\mathcal{U}(-1 \text{ dex deg}^{-1}, 1 \text{ dex deg}^{-1})$
$\log_{10}(\sigma_{[\text{Fe}/\text{H}],\text{BooI}})$	$\mathcal{U}(-1.0, 0.3)$
$\langle\mu_{\alpha*}\rangle_B$	$\mathcal{N}(-0.4 \text{ mas yr}^{-1}, 0.2 \text{ mas yr}^{-1})$
$\langle\mu_\delta\rangle_B$	$\mathcal{N}(-1.1 \text{ mas yr}^{-1}, 0.2 \text{ mas yr}^{-1})$
$\langle v\rangle_{\text{MW}}$	$\mathcal{N}(0 \text{ km s}^{-1}, 50 \text{ km s}^{-1})$
$\log_{10}(\sigma_{v,\text{MW}})$	$\mathcal{U}(-1.0, 4.0)$
$\langle[\text{Fe}/\text{H}]\rangle_{\text{MW}}$	$\mathcal{U}(-5.0, 1.0)$
$\log_{10}(\sigma_{[\text{Fe}/\text{H}],\text{MW}})$	$\mathcal{U}(-1.0, 0.5)$
Axisymmetric Jeans Model	
Q [Gyr]	$\mathcal{U}(0.1, 2.20)$
$\log(b_{\text{halo}})$ [pc]	$\mathcal{U}(0, 5)$
$\log(\rho_0)$ [$M_\odot \text{ pc}^{-3}$]	$\mathcal{U}(-5, -5)$
$-\log(1 - \beta_z)$	$\mathcal{U}(-1, 1)$
α	$\mathcal{U}(0.5, 3)$
β	$\mathcal{U}(3, 10)$
γ	$\mathcal{U}(0, 2)$
i	$\mathcal{U}(\cos^{-1} q', 90)$
Galactic Chemical Evolution Model	
τ_{SFH} [Gyr]	$\mathcal{U}(0.08, 0.35)$
$\log(\tau_{\text{SFE}})$ [Gyr]	$\mathcal{U}(0, 4)$
t_{trunc} [Gyr]	$\mathcal{U}(0, 2)$
η	$\mathcal{U}(0, 10^4)$

NOTE— Priors adopted for each of the free parameters in the Gaussian mixture model used in Section 4, the axisymmetric Jeans model used in Section 6 and the galactic chemical evolution model used in Section 7. $\mathcal{U}(a, b)$ denotes uniform priors bounded by a and b , while $\mathcal{N}(\mu, \sigma)$ denotes a Gaussian prior centered at μ with standard deviation σ

without the need for a GMM. All functional forms for Boo I’s velocity, metallicity, and proper motion distributions as well as the priors on all relevant model parameters are the same as employed in the GMM applied to the individual datasets.

We also fit a model to the simulated dataset from an N -body simulation of Boo I. As in the combined dataset, the stars in the simulated dataset are all assumed to be

⁸ <https://github.com/minaskar/pocomc>

member stars, so we can once again use the likelihood in Equation 11. However, for the N -body simulation, we only consider the heliocentric l.o.s. velocity information of the sample.

4.3. GMM Results: Membership

The membership probability, p_{mem} , of each star in the S^5 dataset is calculated with Equation 9 using draws from the posterior distribution. The median and 1σ uncertainties on p_{mem} for each star are included in Table A1. Figure 3 shows the distribution of median membership probabilities of this sample. Analogous figures for the archival AAT and MMT data are presented in Appendix B. Adopting a median membership probability threshold of $p_{\text{mem}} > 0.8$, we identify 79 likely member stars. Of these, 56 have good radial velocity measurements (i.e., $\sigma_v < 10 \text{ km s}^{-1}$, $\sigma_{[\text{Fe}/\text{H}]} < 0.5 \text{ dex}$, and neither a binary candidate or RRL star) and 51 have good $[\text{Fe}/\text{H}]$ measurements (i.e., $\sigma_v < 10 \text{ km s}^{-1}$, $\sigma_{[\text{Fe}/\text{H}]} < 0.5 \text{ dex}$ and neither a HB or RRL star).

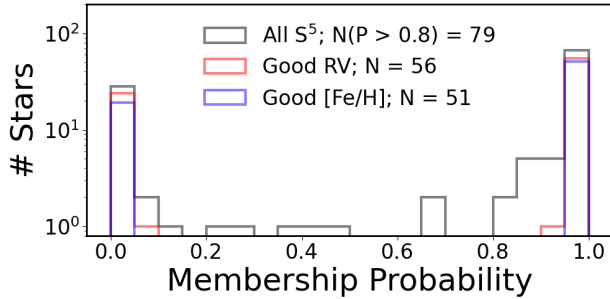


Figure 3. Distribution of median membership probabilities of our S^5 sample. The subset of stars in our sample with good radial velocity measurements (i.e., $\sigma_v < 10 \text{ km s}^{-1}$, $\sigma_{[\text{Fe}/\text{H}]} < 0.5 \text{ dex}$, and neither a binary candidate or RRL star) and good $[\text{Fe}/\text{H}]$ measurements (i.e., $\sigma_v < 10 \text{ km s}^{-1}$, $\sigma_{[\text{Fe}/\text{H}]} < 0.5 \text{ dex}$, and neither a HB or RRL star) are represented by the red and blue histograms respectively. A membership threshold of $p_{\text{mem}} > 0.8$ is adopted in this study to identify high-probability members of Boo I.

Figure 4 shows the distribution of these likely members in several data dimensions, including the color-magnitude diagram (CMD; top left), spatial (top right), proper motion (bottom left), and metallicity and velocity (bottom right). In all panels, large circles represent member stars with good velocity measurements, while triangles, squares, and x's represent RRL stars, binary candidates, and non-member stars respectively. Filled circles denote likely members with good $[\text{Fe}/\text{H}]$ measurements. Superimposed small white circles denote new likely member stars which have not previously been identified as members.

Of the 56 member stars with good velocities, 24 are newly identified by our S^5 observations while 32 were previously identified by Martin et al. (2007), Norris et al.

(2010a), K11, J21, and/or L22. As can be seen in the top right panel of Figure 4, our sample includes likely member stars from the inner half-light radius of Boo I out to $\sim 7r_h$ with the majority of new member stars found beyond one half-light radius.

Merging this S^5 sample of Boo I member stars with those that we (re-)identify from archival AAT and MMT observations and those identified from VLT observations by J21, we create a combined dataset of 148 Boo I members, of which 115 have good non-variable radial velocities suitable for dynamical analyses and 92 have robust $[\text{Fe}/\text{H}]$ measurements suitable for chemical evolution studies. This combined dataset includes 9 and 12 newly identified member stars with good radial velocities from the archival AAT and MMT datasets respectively, though all of these are also present in the S^5 dataset. The distribution of member stars in this combined dataset is presented in Figure 5.

4.4. GMM Results: Systemic Properties

The systemic properties of Boo I inferred from our analysis of the combined data are summarized in Table 3. The inferred properties from the individual S^5 and archival datasets are summarized in Table 5. A more thorough discussion of radially-dependent systemic properties (e.g. gradients) is presented below in Section 5.

The systemic proper motion that we infer from the combined dataset is $\langle \mu_{\alpha,*} \rangle_B = -0.38 \pm 0.02 \text{ mas yr}^{-1}$ in RA and $\langle \mu_\delta \rangle_B = -1.08 \pm 0.01 \text{ mas yr}^{-1}$ in declination. We find nearly identical results for the individual S^5 and archival datasets with the sole exception of the VLT dataset, which lacks bright stars with precise *Gaia* proper motions (see J21 for additional discussion). These values are in good agreement with the recent proper motion measurements of McConnachie & Venn (2020), Martínez-García et al. (2021), Battaglia et al. (2022), Filion et al. (2022), and Pace et al. (2022), but discrepant with the measurements of Li et al. (2021)⁹.

The mean heliocentric l.o.s. velocity of Boo I is not inferred directly in our GMM. Rather, we infer the systemic heliocentric l.o.s. velocity at its center: $v_{0,B} = 103.0_{-0.4}^{+0.4} \text{ km s}^{-1}$ for the combined dataset. We expect the central and mean velocities to be similar if stars are distributed symmetrically about the galaxy's center, which is indeed the case ($\langle v_B \rangle = 103.0_{-0.4}^{+0.4} \text{ km s}^{-1}$). This mean systemic velocity is in good agreement with the mean heliocentric l.o.s. velocity reported by J21 and L22 ($102.6_{-0.8}^{+0.7} \text{ km s}^{-1}$ and $103.0_{-0.6}^{+0.6} \text{ km s}^{-1}$ respectively) as well as the values found for the individual datasets in Appendix B.

⁹ Using *Gaia* EDR3, Li et al. (2021) find $\langle \mu_{\alpha,*} \rangle_B = -0.307 \pm 0.052 \text{ mas yr}^{-1}$ and $\langle \mu_\delta \rangle_B = -1.157 \pm 0.043 \text{ mas yr}^{-1}$.

Table 5. Comparison of Boo I Properties Between Datasets

Parameter	S^5	Arx. AAT	Arx. MMT	Arx. VLT	Combined
Inferred Properties					
f_B	$0.70^{+0.04}_{-0.05}$	$0.81^{+0.05}_{-0.05}$	$0.77^{+0.04}_{-0.05}$
$v_{0,B}$ [km s $^{-1}$]	$103.7^{+0.6}_{-0.6}$	$103.5^{+0.7}_{-0.7}$	$103.5^{+0.7}_{-0.7}$	$102.6^{+0.7}_{-0.8}$	$103.0^{+0.4}_{-0.4}$
$\Delta v_{1,B}$ [km s $^{-1}$ arcmin $^{-1}$]	$0.04^{+0.03}_{-0.03}$	$0.03^{+0.04}_{-0.04}$	$-0.03^{+0.06}_{-0.06}$	$-0.10^{+0.14}_{-0.14}$	$0.02^{+0.03}_{-0.03}$
$\Delta v_{2,B}$ [km s $^{-1}$ arcmin $^{-1}$]	$-0.08^{+0.06}_{-0.06}$	$-0.11^{+0.08}_{-0.08}$	$-0.02^{+0.07}_{-0.07}$	$-0.06^{+0.16}_{-0.16}$	$-0.08^{+0.05}_{-0.05}$
$\sigma_{v,B}$ [km s $^{-1}$]	$3.2^{+0.6}_{-0.5}$	$3.9^{+0.7}_{-0.6}$	$3.7^{+0.6}_{-0.4}$	$5.10^{+0.70}_{-0.80}$	$4.0^{+0.4}_{-0.3}$
[Fe/H] $_{0,B}$ [dex]	$-2.23^{+0.08}_{-0.08}$	$-2.42^{+0.13}_{-0.13}$	$-2.40^{+0.13}_{-0.13}$	$-2.34^{+0.05}_{-0.05}$	$-2.28^{+0.05}_{-0.05}$
$\Delta[\text{Fe}/\text{H}]_B$ [dex arcmin $^{-1}$]	$-0.008^{+0.003}_{-0.003}$	$-0.006^{+0.006}_{-0.007}$	$-0.016^{+0.008}_{-0.008}$...	$-0.010^{+0.003}_{-0.003}$
$\sigma_{[\text{Fe}/\text{H}]_B}$ [dex]	$0.27^{+0.04}_{-0.04}$	$0.40^{+0.06}_{-0.06}$	$0.41^{+0.06}_{-0.05}$	$-0.28^{+0.04}_{-0.03}$	$0.28^{+0.03}_{-0.03}$
$\langle\mu_{\alpha,*}\rangle_B$ [mas yr $^{-1}$]	$-0.39^{+0.02}_{-0.02}$	$-0.39^{+0.02}_{-0.02}$	$-0.39^{+0.02}_{-0.02}$	$-0.45^{+0.04}_{-0.04}$	$-0.38^{+0.02}_{-0.02}$
$\langle\mu_\delta\rangle_B$ [mas yr $^{-1}$]	$-1.07^{+0.01}_{-0.01}$	$-1.07^{+0.01}_{-0.01}$	$-1.07^{+0.01}_{-0.01}$	$-1.13^{+0.03}_{-0.03}$	$-1.08^{+0.01}_{-0.01}$
$C_{\langle\mu_{\alpha,*}\rangle,\langle\mu_\delta\rangle}$	-0.10	-0.10	-0.14	...	-0.08
Additional Derived Properties					
$N_{\text{mem,vel}}$	56	42	37	60	115
$N_{\text{mem},[\text{Fe}/\text{H}]}$	51	41	33	52	92
$\langle v_{\text{BooI}} \rangle$ [km s $^{-1}$]	$103.8^{+0.6}_{-0.6}$	$103.7^{+0.7}_{-0.7}$	$103.4^{+0.6}_{-0.6}$	$102.6^{+0.7}_{-0.8}$	$103.0^{+0.4}_{-0.4}$
$\langle[\text{Fe}/\text{H}]_{\text{BooI}}\rangle$	$-2.38^{+0.05}_{-0.05}$	$-2.51^{+0.07}_{-0.07}$	$-2.60^{+0.10}_{-0.10}$	$-2.34^{+0.05}_{-0.05}$	$-2.43^{+0.04}_{-0.04}$
Δv_B	$0.09^{+0.06}_{-0.04}$	$0.13^{+0.08}_{-0.06}$	$0.08^{+0.05}_{-0.04}$	$0.00^{+0.00}_{-0.00}$	$0.09^{+0.05}_{-0.05}$
$\Delta v'_{1,\text{BooI}}$	$-0.07^{+0.03}_{-0.03}$	$-0.07^{+0.04}_{-0.04}$	$-0.13^{+0.06}_{-0.06}$	$-0.20^{+0.14}_{-0.14}$	$-0.09^{+0.03}_{-0.03}$
$\Delta v'_{2,\text{BooI}}$	$-0.08^{+0.06}_{-0.06}$	$-0.11^{+0.08}_{-0.08}$	$-0.02^{+0.07}_{-0.07}$	$-0.06^{+0.16}_{-0.16}$	$-0.08^{+0.05}_{-0.05}$
$\Delta v'_B$	$0.11^{+0.05}_{-0.04}$	$0.15^{+0.06}_{-0.05}$	$0.15^{+0.06}_{-0.05}$	$0.11^{+0.00}_{-0.00}$	$0.12^{+0.04}_{-0.03}$
Dark Matter Properties					
Q	$1.14^{+0.54}_{-0.58}$	$1.10^{+0.60}_{-0.60}$	$1.18^{+0.51}_{-0.59}$
$\log_{10} b_{\text{halo}}$	$2.85^{+0.92}_{-0.60}$	$3.70^{+0.90}_{-0.80}$	$3.07^{+0.87}_{-0.45}$
$\log_{10} \rho_0$	$-1.54^{+1.44}_{-1.81}$	$-1.80^{+1.20}_{-0.90}$	$-1.88^{+0.90}_{-1.51}$
$-\log_{10}(1 - \beta_z)$	$0.26^{+0.19}_{-0.20}$	$0.10^{+0.50}_{-0.40}$	$0.25^{+0.21}_{-0.21}$
α	$1.63^{+0.89}_{-0.77}$	$1.80^{+0.80}_{-0.80}$	$1.76^{+0.82}_{-0.81}$
β	$6.22^{+2.30}_{-2.11}$	$6.30^{+2.10}_{-2.10}$	$6.39^{+2.20}_{-2.12}$
γ	$1.27^{+0.48}_{-0.74}$	$0.70^{+0.50}_{-0.60}$	$1.00^{+0.52}_{-0.60}$
i	$72.05^{+11.83}_{-13.77}$	$74.20^{+11.20}_{-10.10}$	$70.47^{+12.83}_{-13.23}$
GCE Properties					
τ_{SFH}	$0.2^{+0.1}_{-0.1}$	$0.2^{+0.1}_{-0.1}$
τ_{SFE}	$11.9^{+8.7}_{-5.1}$	$13.9^{+7.6}_{-5.3}$
t_{trunc}	> 0.4	> 0.5
η	170^{+35}_{-46}	203^{+27}_{-36}

NOTE— Properties of Boo I inferred from the analysis of our different datasets. The units of each parameter are the same as in Table 3. Properties for the archival VLT dataset are taken from J21 except for the velocity gradients which are determined analogously to the combined dataset and the dark matter properties which are taken from Hayashi et al. (2023).

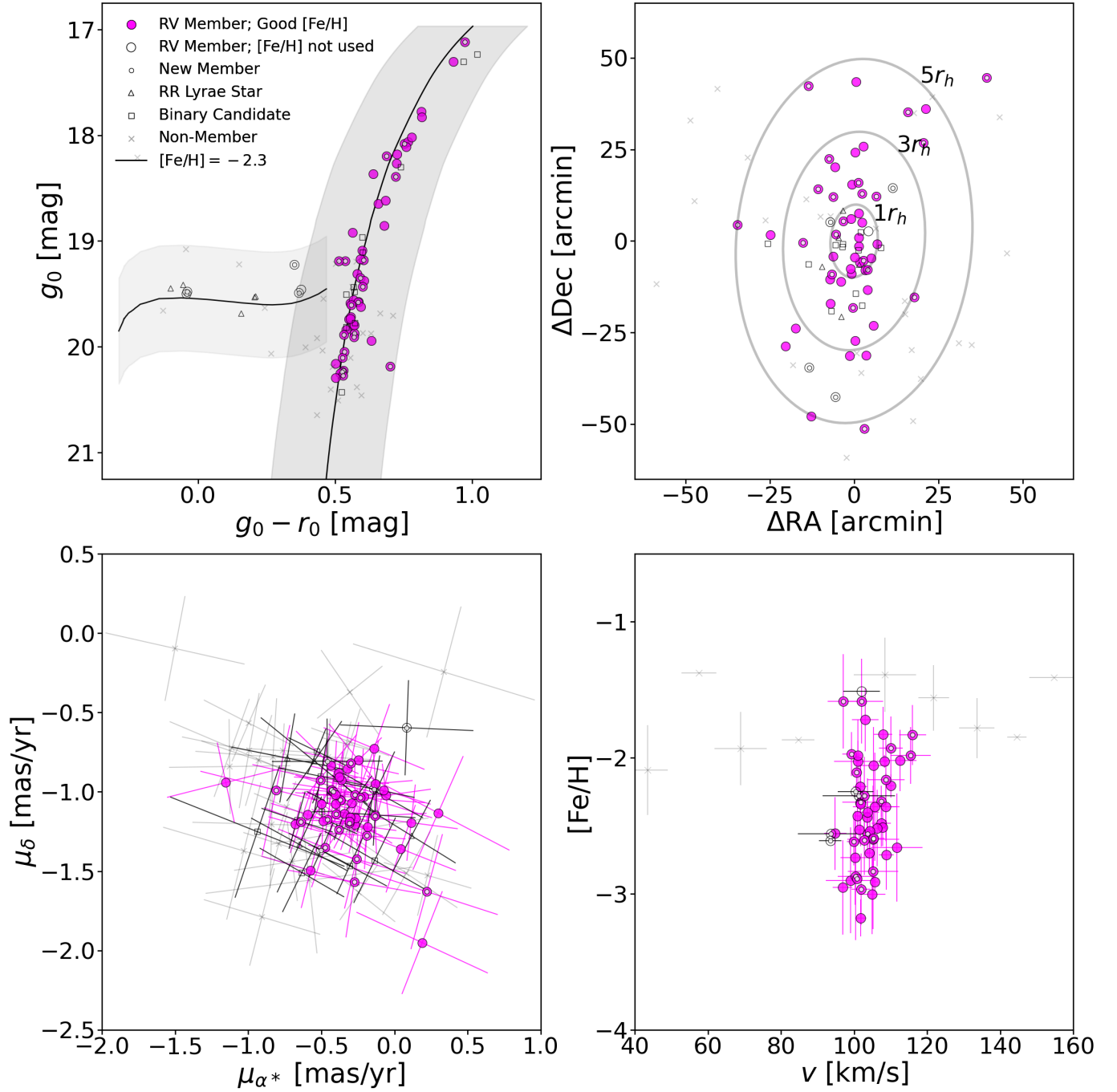


Figure 4. **Top Left.** Extinction-corrected CMD of the S^5 sample. High-probability Boo I members with good radial velocity (and $[\text{Fe}/\text{H}]$) measurements are represented by (filled) circles. Open triangle and square markers represent RRL stars and binary candidates respectively, while gray x's represent non-members. Smaller inset white circles denote new likely member stars, which were not identified in previous studies. **Top Right.** On-sky spatial distribution of the S^5 sample. Gray ellipses indicate the 1, 3, and 5 half-light radii of Boo I from Muñoz et al. (2018). **Bottom Left.** Proper motion distribution of the S^5 sample from *Gaia* DR3 (Gaia Collaboration et al. 2022). **Bottom Right.** Distribution of $[\text{Fe}/\text{H}]$ vs. radial velocity for the S^5 sample. Stars without reliable $[\text{Fe}/\text{H}]$ measurements (open circles) are included using the nominal $[\text{Fe}/\text{H}]$ value reported by RVSpecFit.

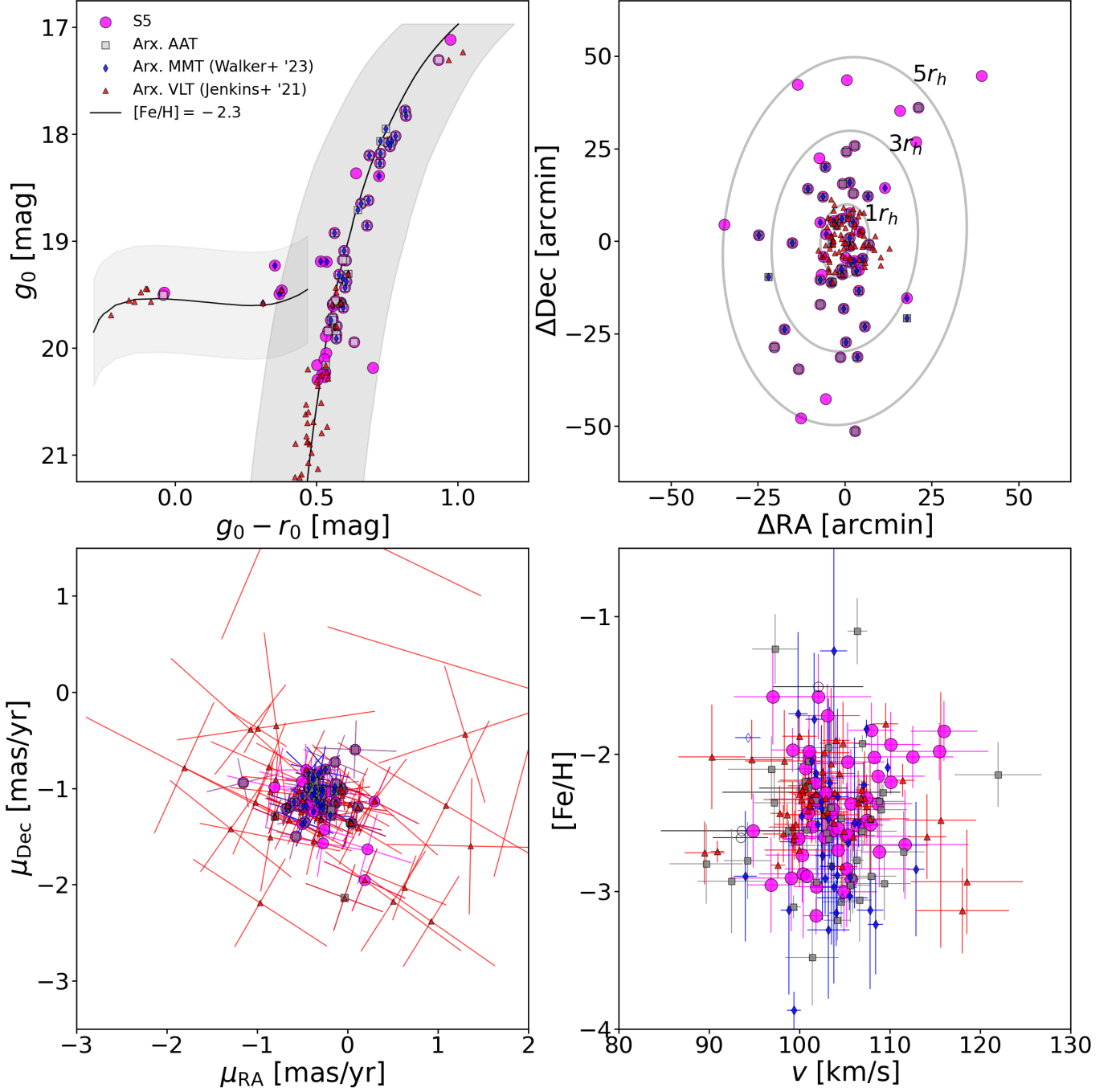


Figure 5. Same as Figure 4 except showing only likely Boo I member stars with good radial velocity measurements from the respective S^5 , archival AAT, archival MMT, and archival VLT datasets (magenta circles, gray squares, blue diamonds, and red triangles respectively).

From our combined dataset, we infer a marginally resolved heliocentric l.o.s. velocity gradient, which is oriented approximately along Boo I’s semi-minor axis. The components of the velocity gradient parallel and perpendicular to Boo I’s on-sky proper motion are $\Delta v_{1,B} = 0.02 \pm 0.03 \text{ km s}^{-1} \text{ arcmin}^{-1}$ and $\Delta v_{2,B} = -0.08 \pm 0.05 \text{ km s}^{-1} \text{ arcmin}^{-1}$ respectively—or equivalently $\Delta v_{1,B} = 0.2 \pm 0.3 \text{ km s}^{-1} r_h^{-1}$ and $\Delta v_{2,B} = -0.8 \pm 0.5 \text{ km s}^{-1}$

r_h^{-1} . This velocity gradient is consistent with the gradients found for the individual datasets in Appendix B. However, it is substantially shallower than and approximately perpendicular to the gradient reported by L22. Boo I’s velocity gradient is discussed in more detail in Section 5.1.

We infer the velocity dispersion of Boo I to be $\sigma_{v,B} = 4.0^{+0.4}_{-0.3}$. This is consistent with, though slightly smaller

than, the previous constraints from J21 and L22 of $5.1^{+0.7}_{-0.8}$ km s⁻¹ and $4.5^{+0.3}_{-0.3}$ km s⁻¹ respectively. The smaller velocity dispersion found in this work can likely be attributed to a more thorough exclusion of binary stars. For a discussion of a potential radial dependence of the velocity dispersion, see Section 5.2.

From our combined dataset, we infer the central metallicity of Boo I to be $[\text{Fe}/\text{H}]_{0,\text{B}} = -2.28 \pm 0.05$. The mean metallicity derived from the likely member stars is slightly lower, $\langle [\text{Fe}/\text{H}]_{\text{B}} \rangle = -2.43 \pm 0.04$, as would be expected in the presence of a negative metallicity gradient. Indeed, we infer a weak but clearly resolved metallicity gradient of $\Delta[\text{Fe}/\text{H}]_{\text{B}} = -0.010 \pm 0.003$ dex arcmin⁻¹ or -0.10 ± 0.03 dex r_h^{-1} (see Section 5.3 for additional discussion). We infer a metallicity dispersion of $\sigma_{[\text{Fe}/\text{H}],\text{B}} = 0.28 \pm 0.03$. The shape and physical interpretation of Boo I’s MDF is presented in Section 7.

Our inferred metallicity dispersion is in good agreement with the metallicity dispersions inferred by J21 and L22 of $\sigma_{[\text{Fe}/\text{H}],\text{B}} = 0.28^{+0.04}_{-0.03}$ and $0.26^{+0.04}_{-0.03}$ respectively. The metallicity gradient we infer is also consistent with the gradient reported by L22 ($\Delta[\text{Fe}/\text{H}]_{\text{B}} = -0.008^{+0.003}_{-0.003}$ dex arcmin⁻¹). However, the mean metallicity we infer is slightly lower than found by J21 (-2.34 ± 0.05) and slightly higher than found by L22 (-2.60 ± 0.03). The difference with J21 can easily be explained by the different spatial selection of the two datasets. The J21 sample is contained nearly entirely within Boo I’s inner half-light radius, and is thus expected to be more metal-rich given Boo I’s negative metallicity gradient. Differences in sample composition may also explain the difference with L22, as we find that the archival AAT (and MMT) datasets have mean metallicities that are 0.1 (and 0.2) dex lower than the combined dataset. We note that a mean metallicity of -2.43 that we find in this analysis would place Boo I squarely on the Local Group dwarf galaxy mass- and luminosity-metallicity relationships of Kirby et al. (2013), while a mean metallicity of -2.60 would place Boo I slightly below these relationships (though certainly still within the relationship’s intrinsic scatter).

5. POPULATION GRADIENTS

In this section, we discuss in greater detail the population gradients (or lack thereof) that we infer from our datasets, including the velocity gradient (Section 5.1), the velocity dispersion profile (Section 5.2), and the metallicity gradient and dispersion profile (Section 5.3).

5.1. Velocity Gradient

The presence, or lack thereof, of a velocity gradient in a galaxy provides clues as to its internal dynamics and dynamical evolution. For example, a velocity gradient oriented along a galaxy’s semi-major axis might indicate oblate (i.e., disk-like) rotation, while a velocity gradient oriented along a galaxy’s semi-minor axis as observed in

the M31 dwarf spheroidal (dSph) satellite, Andromeda II (Ho et al. 2012), the isolated dwarf irregular, Phoenix (Kacharov et al. 2017), and the MW dSph satellite, Ursa Minor (Pace et al. 2020) would be indicative of prolate rotation about its minor axis, perhaps as the result of a merger (e.g., Ebrova & Lokas 2017). On the other hand, a velocity gradient oriented along a galaxy’s orbit is potentially a sign of tidal disruption as reported in MW UFDs Hercules (Aden et al. 2009; Martin & Jin 2010; Kupper et al. 2017; Ou et al. 2024), Ursa Major II (Simon & Geha 2007; Smith et al. 2013), and Leo V (Collins et al. 2017), as well as diffuse MW satellites Antlia 2 and Crater 2 (Ji et al. 2021). However, due to small sample sizes and uncertain measurements, the detection of velocity gradients in most UFDs remains quite tenuous.

In the top two panels of Figure 6, we illustrate the observed velocity gradients inferred from the S^5 (top left) and combined (top right) Boo I datasets. The median and 1σ uncertainties on the observed heliocentric l.o.s. velocity gradient are represented by the yellow arrows and ellipses respectively. High-probability member stars are included as circles color-coded by their heliocentric l.o.s. velocity. The on-sky proper motion vector is included as a magenta arrow, while the galaxy’s orbit as calculated with Galpy¹⁰ (Bovy 2015) assuming the MWPotential2014 is denoted by the cyan line. We stress that the observed proper motion vector is not aligned with Boo I’s orbit because it has not been corrected for solar reflex motion (i.e., the Sun’s motion with respect to Boo I).

As discussed briefly in Section 4.4, we observe a shallow, marginally resolved heliocentric l.o.s. velocity gradient aligned roughly along Boo I’s semi-minor axis in both the combined and S^5 datasets. In the combined dataset, this gradient has a magnitude of $\Delta v_{\text{B}} = 0.09 \pm 0.05$ km s⁻¹ arcmin⁻¹ (0.9 ± 0.5 km s⁻¹ r_h^{-1}) and a position angle of $\theta_{\Delta v} = 86^{+28}_{-19}$ degrees. We find similar results in the individual archival datasets, though with considerably larger uncertainties (see Appendix B).

It is important to note that the reported velocity gradients above are the observed velocity gradient and not the intrinsic or internal velocity gradient of Boo I as we have not yet accounted for projection effects related to the galaxy’s relative motion. As discussed previously in the literature (see Feast et al. 1961; van der Marel et al. 2002; Kaplinghat & Strigari 2008; Walker et al. 2008; Pace et al. 2020), a satellite galaxy modeled as an extended solid body moving relative to the observer will exhibit an observed velocity gradient along its on-sky proper motion direction even in the absence of tidal disruption or intrinsic rotation simply because stars on one

¹⁰ <http://github.com/jobovy/galpy>

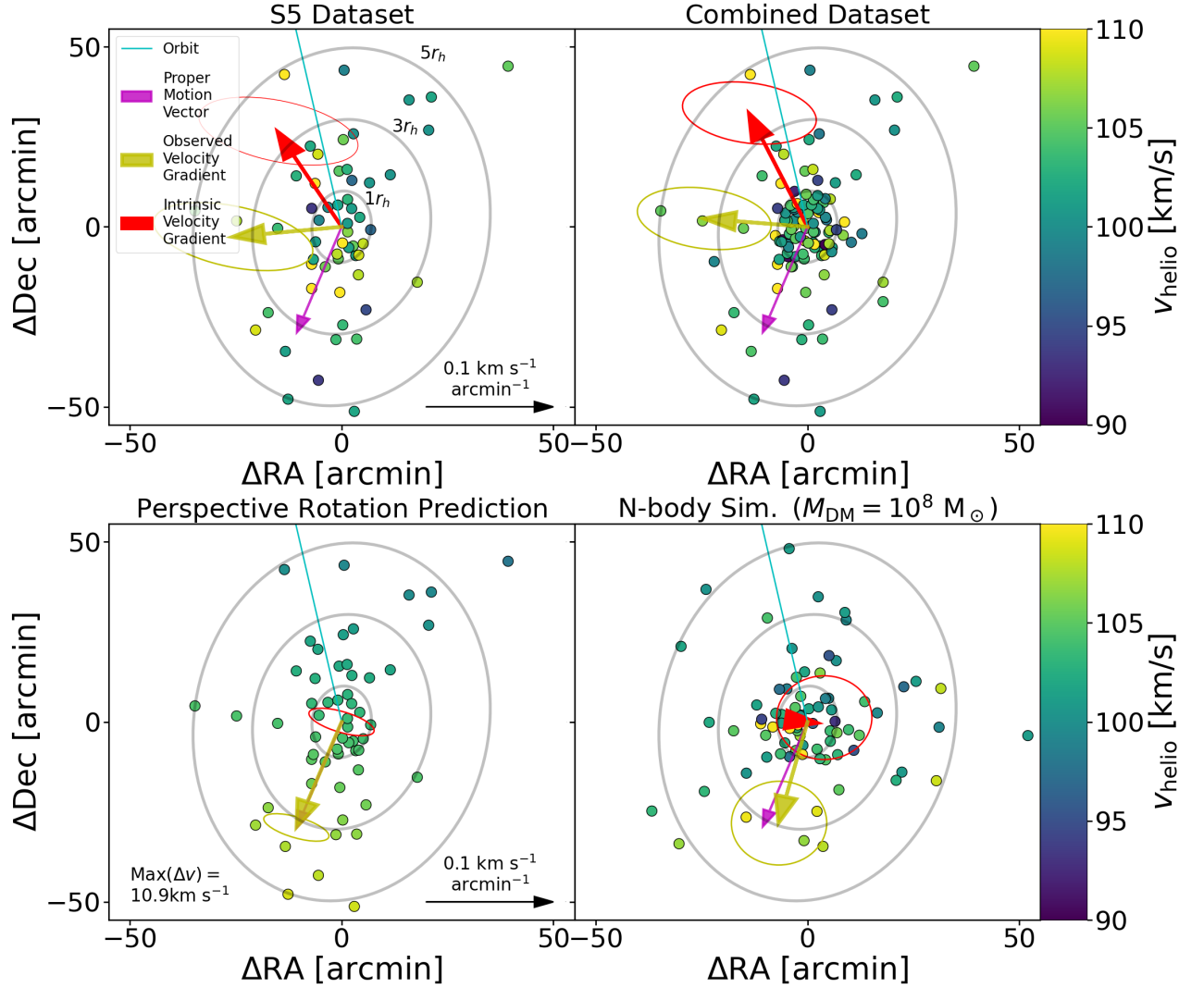


Figure 6. Each panel shows the on-sky spatial distribution of Boo I members colored by their heliocentric l.o.s. velocity. The orbit and proper motion vector of Boo I are represented in each panel by the cyan line and magenta arrow respectively, while the observed and intrinsic velocity gradient are represented by the yellow and red arrows respectively. Yellow and red ellipses show the 1σ uncertainties on the corresponding velocity gradient vectors. The top two panels show the member stars and inferred velocity gradients for the S^5 (left) and combined datasets (right). The bottom left panel illustrates the velocity gradients predicted from solid body perspective rotation in the absence of intrinsic velocity gradients. The bottom right panel illustrates the velocity gradients predicted by mock S^5 -like observations of an N-body simulation of Boo I.

side of the galaxy will be moving towards or away from the observer faster than stars on the other.

This “perspective rotation” is more pronounced for systems that are nearby, have higher proper motions, and are more extended on the sky. As a result, it has primarily been considered in the analysis of classical dSph satellites due to their larger sizes (e.g., Kaplinghat & Strigari 2008; Walker et al. 2008; Pace et al. 2020). Re-

cently, Ji et al. (2021) demonstrated the importance of accounting for perspective rotation when investigating the tidal disruption of the ultra diffuse galaxies Antlia 2 and Crater 2. At a distance of only ~ 66 kpc, the extent of our Boo I sample ($\sim 7r_h$) spans roughly 2° on the sky, which results in a non-negligible perspective rotation signature. Here we explore the impact of that effect on Boo I’s intrinsic velocity gradient. To our knowledge,

this is the first consideration of perspective rotation in any UFD.

In the bottom left panel of Figure 6, we illustrate the observed velocity gradient we would expect to observe in Boo I from this perspective rotation alone. As expected, this observed velocity gradient is oriented along Boo I’s proper motion vector. The magnitude of this effect in Boo I is $0.105 \pm 0.004 \text{ km s}^{-1} \text{ arcmin}^{-1}$, which results in a non-negligible 10.9 km s^{-1} difference in the heliocentric l.o.s. velocity over the 2-degree FoV of our sample. Indeed, we find from additional tests on bootstrapped data that in the absence of an intrinsic velocity gradient and given Boo I’s intrinsic velocity dispersion and S^5 ’s sample and velocity uncertainties, we would recover a non-zero gradient due to perspective rotation 99% of the time.

In each panel of Figure 6, we depict the intrinsic velocity gradients (i.e., with perspective rotation removed) and their uncertainties as red arrows and ellipses respectively. For the perspective rotation prediction (bottom left), the intrinsic velocity gradient is zero by construction. For the combined dataset, the intrinsic velocity gradient has a slope of $\Delta v_{B'} = 0.12^{+0.04}_{-0.03} \text{ km s}^{-1} \text{ arcmin}^{-1}$ ($1.2^{+0.4}_{-0.3} \text{ km s}^{-1} r_h^{-1}$) and a position angle of $\theta_{\Delta v'} = 34^{+9}_{-39}$ degrees. Similar, albeit less certain, intrinsic velocity gradients are found for the individual archival datasets (see Appendix B).

5.1.1. Comparison to Literature

Our results for the observed velocity gradient are in stark contrast with the observed velocity gradient reported by L22 of $\Delta v_B = 0.40 \pm 0.10 \text{ km s}^{-1} \text{ arcmin}^{-1}$ along Boo I’s semi-major axis, which is equivalent to $\Delta v_{1,B} = -0.39 \pm 0.10 \text{ km s}^{-1} \text{ arcmin}^{-1}$ and $\Delta v_{2,B} = -0.10 \pm 0.02 \text{ km s}^{-1} \text{ arcmin}^{-1}$ if decomposed into two components along ϕ_{1*} and ϕ_{2*} as in our model. Notably, their velocity gradient predicts a difference in the mean velocity from one end of our Boo I sample to the other of $\sim 40 \text{ km s}^{-1}$. Because L22 do not correct for perspective rotation, which acts opposite to their observed gradient, the intrinsic velocity gradient implied by their result would be even larger, $\Delta v'_B \sim 0.50 \text{ km s}^{-1} \text{ arcmin}^{-1}$.

We are unable to explain this disagreement as we cannot reproduce their reported velocity gradient when applying our methods to their provided catalog of member stars. We also find no evidence of the large change in mean velocity across either dataset that would be predicted by their gradient, though it should be easily detectable given the typical velocity uncertainty of the data and intrinsic velocity dispersion of Boo I.

It is possible that the inclusion of additional archival data sources (e.g., from Martin et al. 2007; Lai et al. 2011; Gilmore et al. 2013; Ishigaki et al. 2014; Frebel et al. 2016) or the presence of binary systems in the data analyzed by L22 is the source of the very steep

gradient they infer. It is also possible that the strength of their velocity gradient is biased by foreground stars in the outskirts of their sample. We note that the binned kinematic analysis of L22 appears consistent with a flat or shallow velocity gradient for $r/r_h \lesssim 2$ and only appears steeper in their outer-most radial bins, which are characterized by small sample sizes, substantially larger velocity dispersions than the inner radial bins (~ 10 vs. $\sim 4 \text{ km s}^{-1}$), and large $\sim 5\text{--}10 \text{ km s}^{-1}$ uncertainties on both the mean velocity and velocity dispersion.

5.1.2. Comparison to Simulations

In order to compare our observational results to expectations from dynamical simulations, we apply similar modeling techniques to an N -body simulation of Boo I. As described in Section 2.6, we adopt median S^5 observational velocity uncertainties ($\sim 4 \text{ km s}^{-1}$) and down-sample to match the spatial distribution of member stars in the S^5 dataset. We repeat our analysis with 10 bootstrapped samples in order to quantify the uncertainty of our inference on the sample size.

As shown in the bottom right panel of Figure 6, we infer an observed velocity gradient of $0.10 \pm 0.02 \text{ km s}^{-1} \text{ arcmin}^{-1}$ aligned with proper motion vector of Boo I. This matches our expectations for perspective rotation in the absence of an intrinsic velocity gradient (bottom left panel) but not what we infer for the observational data (top two panels). The lack of a detectable intrinsic velocity gradient, however, does not imply that the simulated Boo I has not experienced tidal disruption, nor does it imply that the simulated Boo I is without a velocity gradient. Indeed, when inspecting the full N -body simulation prior to down sampling (see Figure 1), there is evidence of tidal debris along the simulated orbit. These tidal features, however, are diffuse and located beyond the footprint of our dataset. This is consistent with our earlier finding that $r_t \gtrsim 8 \text{ kpc}$.

In Figure 7, we illustrate the line-of-sight velocity field of the N -body simulation. In the left panel, we show the median observed heliocentric l.o.s. velocity of N -body particles across the simulated Boo I. Here we can see that the velocity gradient within $5\text{--}10r_h$ is dominated by perspective rotation and oriented along the simulated galaxy’s proper motion vector. In the right panel, we show the median heliocentric l.o.s. velocity corrected for perspective rotation. With this correction applied, a clear velocity gradient aligned with the galaxy’s tidal features and orbital motion is visible. While the magnitude of this gradient at large radii is similar to what we infer from our observations of Boo I, the velocity field is approximately constant within the inner $\sim 7r_h$, which is why we do not detect it in our mock sample. We also do not find evidence of a tangential velocity gradient (i.e., in proper motions space) within the inner region of the simulated galaxy.

The difference between the results inferred from the observed dataset and the simulated dataset may suggest

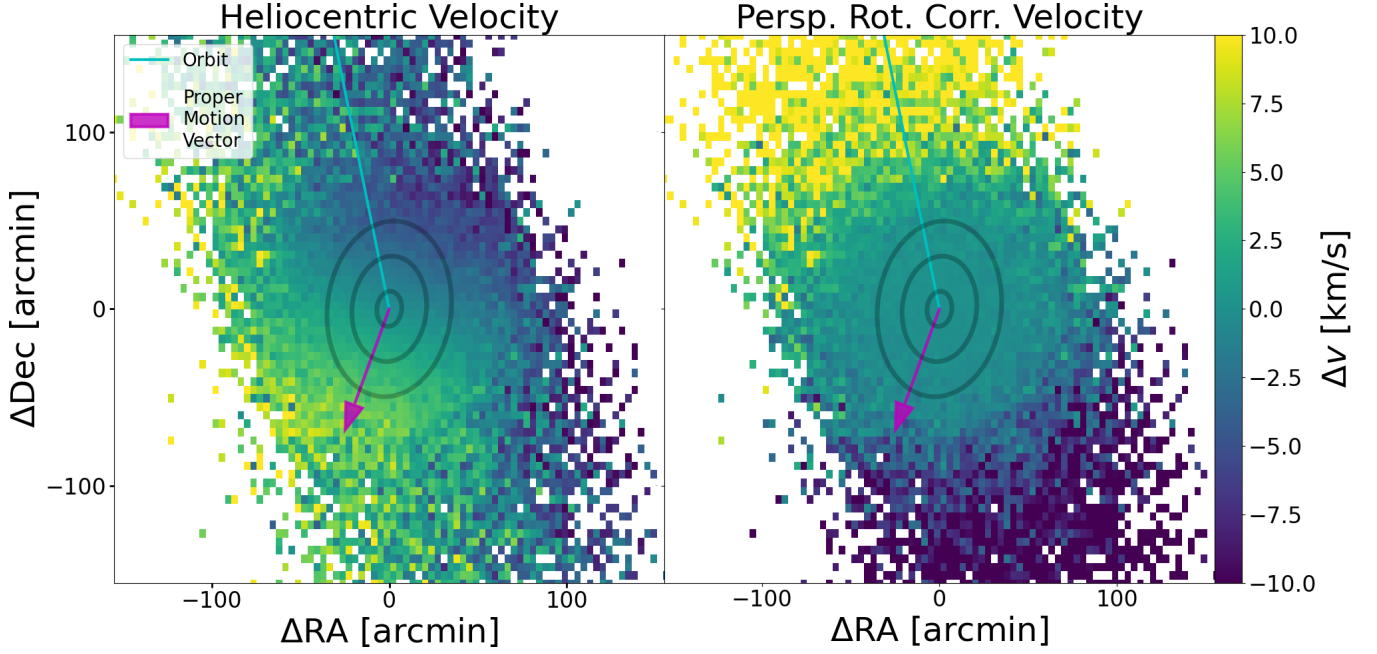


Figure 7. Velocity field of the Boo I N -body simulation without (left) and with (right) accounting for the effect of perspective rotation. In the left-hand panel, the velocity gradient is dominated by the perspective rotation, while in the right-hand panel the velocity gradient is dominated by tidal disruption at large radii and approximately flat within $7r_h$.

one or more of the following. It is possible that the intrinsic velocity gradient inferred from our observational data is not due to tidal disruption as initially expected but is instead evidence of rotation, either intrinsic or as the result of a dwarf-dwarf merger (e.g., Frebel et al. 2016). Alternatively, it is possible that the N -body simulation is less prone to disruption than Boo I, perhaps because it assumes a spherical rather than triaxial halo (e.g., Moore et al. 2004). To test these hypotheses, additional dynamical modeling is necessary, which we will undertake in a future study.

5.1.3. Tides vs. Rotation

As introduced previously, a velocity gradient may be the result of intrinsic disk-like rotation, merger-induced rotation, and/or tidal disruption. While the inferred intrinsic velocity gradient appears to be most closely aligned with Boo I’s orbit, the uncertainties on the direction of the intrinsic velocity gradient vector and the near alignment of Boo I’s semi-major axis and orbital motion make it difficult to confidently discriminate between a tidal or rotational origin of the gradient from the orientation alone. Of course, the alignment of Boo I’s semi-major axis with its orbit is itself an indication of potential tidal disruption as noted by previous studies (e.g., Muñoz et al. 2018; Pace et al. 2022; Longeard et al. 2022, see also Muñoz et al. 2008 for additional discussion of elongation and tides). Moreover, oblate rotation in UFDs is exceedingly rare, with only Hydrus 1 showing tentative signs of disk-like rotation (Koposov et al. 2018). Given Boo I’s early infall 7–10 Gyr ago (e.g.,

Rocha et al. 2012; Miyoshi & Chiba 2020; Barmantloo & Cautun 2023), it seems unlikely that it would have maintained any intrinsic disk-like morphology or rotation due to the effects of tidal stirring (e.g., Mayer et al. 2001; Kazantzidis et al. 2011).

On the other hand, the lack of a velocity gradient in the inner $\sim 7r_h$ of the simulated dataset complicates the conclusion that Boo I’s velocity gradient is of tidal origin. However, as discussed in Section 5.1.2, it is possible that the N -body simulation experiences less tidal disruption than Boo I as a result of modeling choices (e.g., a spherical NFW dark matter density profile). To further investigate the potential tidal origins of the velocity gradient, we calculate Boo I’s tidal radius at pericenter following the approach of Pace et al. (2025). Assuming a flat rotation curve for the MW and a circular orbit for Boo I, the tidal radius at pericentric passage can be estimated as $r_t = r_{\text{peri}}(M_{\text{BooI}}/2M_{\text{MW}})^{1/3}$, where r_{peri} , M_{BooI} , and M_{MW} are the pericentric distance, Boo I mass, and enclosed MW mass at pericenter respectively (King 1962). We adopt $r_{\text{peri}} = 35$ kpc from Battaglia et al. (2022) and estimate the enclosed MW mass using the `MWPotential2014` potential from Bovy (2015). For the mass of Boo I, we integrate the dark matter density profile inferred in Section 6 out to the scale radius of the dark matter halo (~ 1 kpc). This yields a tidal radius of $r_t \sim 2.4$ kpc, roughly 13 times Boo I’s half-light radius. Accounting for 1σ uncertainties in the dark matter density profile parameters, the tidal radius could be as small as $r_t = 1.5$ kpc or $7.9r_h$. A tidal radius of ~ 8 – $13r_h$ is approximately consistent with the

radius at which the velocity gradient becomes apparent in the simulated dataset (Figure 7). It thus seems unlikely that any of the Boo I members identified in this work are unbound, being actively stripped away, or are otherwise strongly affected by tidal forces. If this is true, then tides alone cannot explain Boo I’s velocity gradient. To more definitively test the potential tidal origins of Boo I’s velocity gradient, a dedicated search should be made for stripped extra-tidal member stars.

Another possibility is that Boo I’s elongation is the result of a past merger as argued by Frebel et al. (2016), which could have imparted a rotational signature in the galaxy’s outskirts. However, this scenario would require the chance alignment of the merger event with Boo I’s orbital motion. Nevertheless, it is difficult to rule out this scenario without either a larger sample of stars or additional measurements of stellar chemistry (e.g., α and/or neutron-capture elements) from high-resolution spectroscopy of stars in Boo I’s outskirts. Such observations would need to be sufficiently precise to distinguish between the presence of multiple stellar populations and the existence of smooth radial gradients in Boo I’s chemodynamic properties.

Unfortunately, even with the larger combined dataset presented in this work, Boo I’s velocity gradient remains enigmatic and of uncertain origin. To confidently discriminate between rotational (either intrinsic or merger-induced) and tidal origins additional observations of Boo I at large radii are required.

5.2. Velocity Dispersion Profile

The radial velocity dispersion profile of a dwarf galaxy provides valuable insight into its dynamical evolution, including the presence of multiple dynamic populations (e.g., Pace et al. 2020), the impacts of tidal disruption (e.g., Read et al. 2006; Peñarrubia et al. 2008), and the shape of its underlying dark matter halo (e.g., Lokas 2002; Walker et al. 2008; Hayashi et al. 2020). In this section, we perform a simple binned analysis to investigate Boo I’s empirical velocity dispersion profile. An un-binned analysis providing updated constraints on Boo I’s dark matter profile is presented in Section 6.

For each of our datasets, we separate our sample of likely member stars with good velocities into three radial bins: $r/r_h < 1$, $1 \leq r/r_h < 3$, and $r/r_h \geq 3$. In the S^5 dataset the number of stars in each bin is approximately equal with ~ 20 stars in each bin, whereas for the combined dataset, the number of stars decreases from ~ 60 in the inner bin to ~ 20 in the outer bin, owing to the large contribution of member stars within one half-light radius from archival VLT observations. From the sample of likely member stars, we subtract out the systemic velocity inferred from our GMM (including the observed velocity gradient), and fit for the velocity dispersion in each bin.

Figure 8 displays the results of this binned velocity dispersion analysis. The top two panels display the residual

heliocentric l.o.s. velocities of the S^5 (left) and combined (right) samples. In the bottom 2 panels, we plot the inferred velocity dispersion of each bin. The global velocity dispersions inferred from our GMM analysis (see Section 4.4) are included as horizontal lines for reference. Analogous results for the individual archival datasets are presented in appendix Figure B and discussed in Appendix B.

While a slightly lower global velocity dispersion is inferred from the S^5 dataset compared to the combined dataset ($3.2^{+0.6}_{-0.5}$ km s $^{-1}$ vs. $4.0^{+0.4}_{-0.3}$ km s $^{-1}$), both datasets exhibit a similarly shaped velocity dispersion profile. For the combined (S^5) dataset, the velocity dispersion within one half-light radius is $3.2^{+0.5}_{-0.4}$ km s $^{-1}$ ($2.7^{+0.8}_{-0.6}$ km s $^{-1}$). This increases to $5.3^{+0.9}_{-0.7}$ km s $^{-1}$ ($4.2^{+1.2}_{-0.8}$ km s $^{-1}$) between one and three half-light radii and decreases to $2.9^{+0.8}_{-0.6}$ km s $^{-1}$ ($2.2^{+0.8}_{-0.6}$ km s $^{-1}$) beyond three half-light radii.

The peak in the velocity dispersion profile between one and three r_h is qualitatively consistent with the radially increasing velocity dispersion reported by L22. L22, however, infers a much larger velocity dispersion ($\sim 10 \pm 5$ km s $^{-1}$) at $\sim 3 r_h$, perhaps due to the smaller number of members and increased foreground contamination or perhaps related to their treatment of the velocity gradient.

5.3. Metallicity Gradient and Dispersion Profile

The metallicity gradients of dwarf galaxies have long been a subject of interest as they are thought to encode a variety of physical processes, including secular inside-out evolution, stellar feedback-induced radial migration, mergers, and tidal stripping (e.g., Schroyen et al. 2013; Pontzen & Governato 2014; Benítez-Llambay et al. 2016; Revaz & Jablonka 2018; Mercado et al. 2021; Tarumi et al. 2021). While metallicity gradients are commonplace and varied in massive MW and M31 satellites, they have only been detected in four UFDs. Chiti et al. (2021) detected a gradient of $\Delta[\text{Fe}/\text{H}] \sim -0.1$ dex r_h^{-1} along with an extended stellar halo in Tucana II, which is thought to be the product of a major merger (e.g., Tarumi et al. 2021; Chiti et al. 2023). Fu et al. (2024) detected gradients of $\Delta[\text{Fe}/\text{H}] \sim -0.2$ dex r_h^{-1} and -0.5 dex r_h^{-1} in Andromeda XVI and XXVIII, which are consistent with radial migration driven by their extended star formation histories. Lastly, L22 detected a shallow gradient of $\Delta[\text{Fe}/\text{H}] \sim -0.08$ dex r_h^{-1} in Boo I.

In the top two panels of Figure 9, we illustrate the metallicity gradients inferred from the S^5 (top left) and combined (top right) Boo I datasets. As discussed briefly in Section 4.4, we recover a weak, but resolved, negative metallicity gradient of $\Delta[\text{Fe}/\text{H}]_{\text{B}} = -0.008 \pm 0.003$ dex arcmin $^{-1}$ for the S^5 dataset and $\Delta[\text{Fe}/\text{H}]_{\text{B}} = -0.010 \pm 0.003$ dex arcmin $^{-1}$ for the combined dataset. Measured in terms of Boo I’s half-light radii, these are equivalent to ~ -0.08 dex r_h^{-1} and

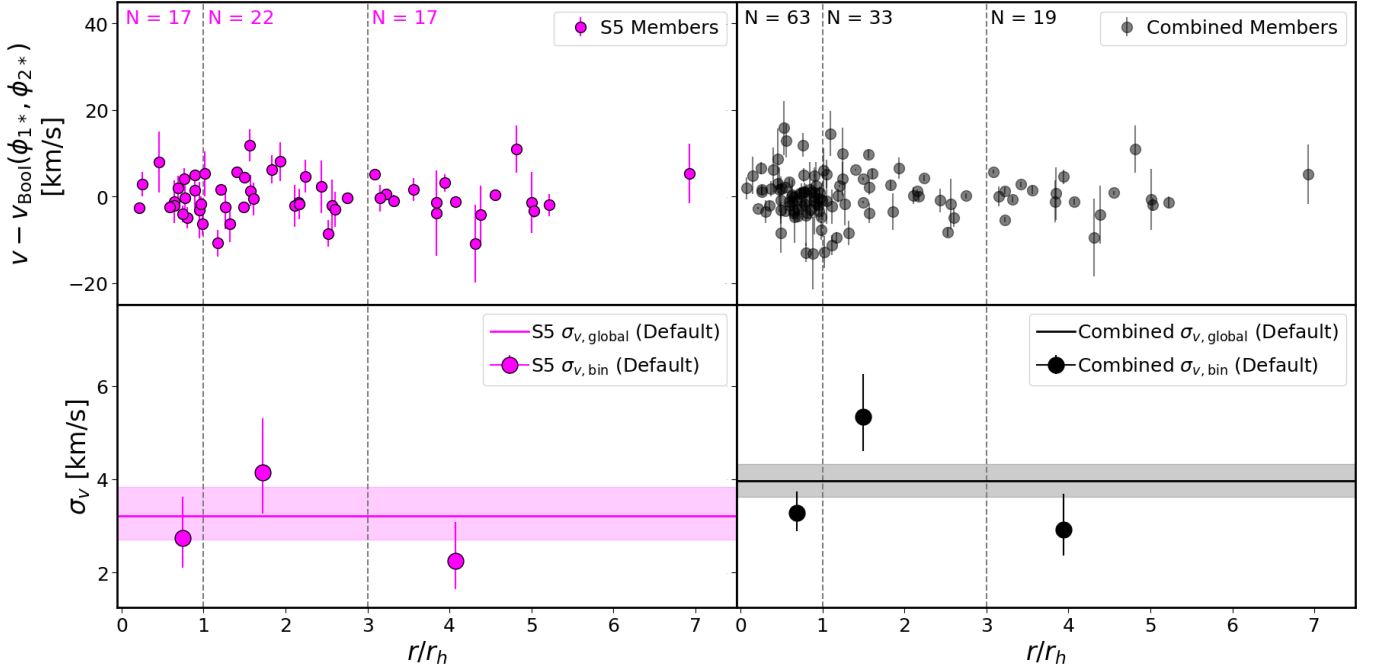


Figure 8. Top. Dispersion of heliocentric l.o.s. velocities around the inferred systemic velocity gradient as a function of radius for high probability Boo I members in the S^5 (left; magenta circles) and combined (right; black circles) datasets. **Bottom.** Velocity dispersion of Boo I members in radial bins of $r/r_h < 1$, $1 \leq r/r_h < 3$, and $r/r_h \geq 3$ for the S^5 (left; magenta circles) and combined (right; black circles) datasets. Markers are plotted at the median radius of the stars in each bin. For comparison, we include the global velocity dispersion inferred from the data (solid lines and shaded regions).

$\sim -0.10 \text{ dex } r_h^{-1}$ respectively, which is in good agreement with the gradient previously reported by L22. We find similar results for the individual archival datasets as well (see Appendix B).

In the bottom two panels of Figure 9, we display the binned metallicity dispersion profile of Boo I, following the same approach as done for the velocity dispersion profile in the previous section. We find that both the S^5 and combined datasets are consistent with a flat metallicity dispersion profile. The combined dataset hints at an increasing metallicity dispersion with radius, but the uncertainties are large enough to be 1σ consistent with the inferred global metallicity dispersion.

The similarity between Boo I and Tucana II in both metallicity gradient and extended stellar population, suggests that Boo I, like Tucana II, may have experienced a past major merger event as proposed by Frebel et al. 2016 and Tarumi et al. 2021. However, it is worth noting that when compared with more massive classical dwarfs of a similar age, Boo I’s metallicity gradient is similar to those without evidence of a major merger (e.g., Cetus, Draco, Tucana, Pegasus) and shallower than those that do (e.g., Phoenix, Sextans; Taibi et al. 2022). Of course, any number of confounding factors, including tidal stripping, could have played a subsequent role in flattening a merger-created gradient.

Whether the product of a merger or secular evolution, it is quite likely that the dearth of resolved metallicity

gradients in UFDs is at least in part driven by the limited samples of metallicity measurements at large radii. Determining the origin of these gradients will require additional high-precision metallicity and individual elemental abundance measurements beyond $\sim 3r_h$.

6. DARK MATTER DENSITY PROFILE

As a nearby dark matter-dominated galaxy, Boo I—like other UFDs—has been the subject of multiple dynamic studies concerned with the nature and distribution of dark matter (e.g., Pace & Strigari 2019; Hayashi et al. 2021b,a, 2023; Horigome et al. 2023). However, each of these past analyses have been limited to the archival VLT datasets of K11 or J21, which only trace the stellar dynamics within one half-light radius and feature higher contamination from binary systems. In this section, we revisit the dark matter content of Boo I, using our larger and more spatially extended S^5 and combined datasets.

Specifically, we apply the axisymmetric Jeans mass modeling methods developed in Hayashi & Chiba (2012), Hayashi & Chiba (2015), and Hayashi et al. (2020). These methods were previously applied to MW UFDs, including Boo I, in Hayashi et al. (2023). A detailed description and discussion of this methodology is provided in the aforementioned papers, and an abridged summary is provided in Appendix C. In short, this mass modeling assumes that Boo I resides in a dark matter halo with a generalized axisymmetric Hernquist profile

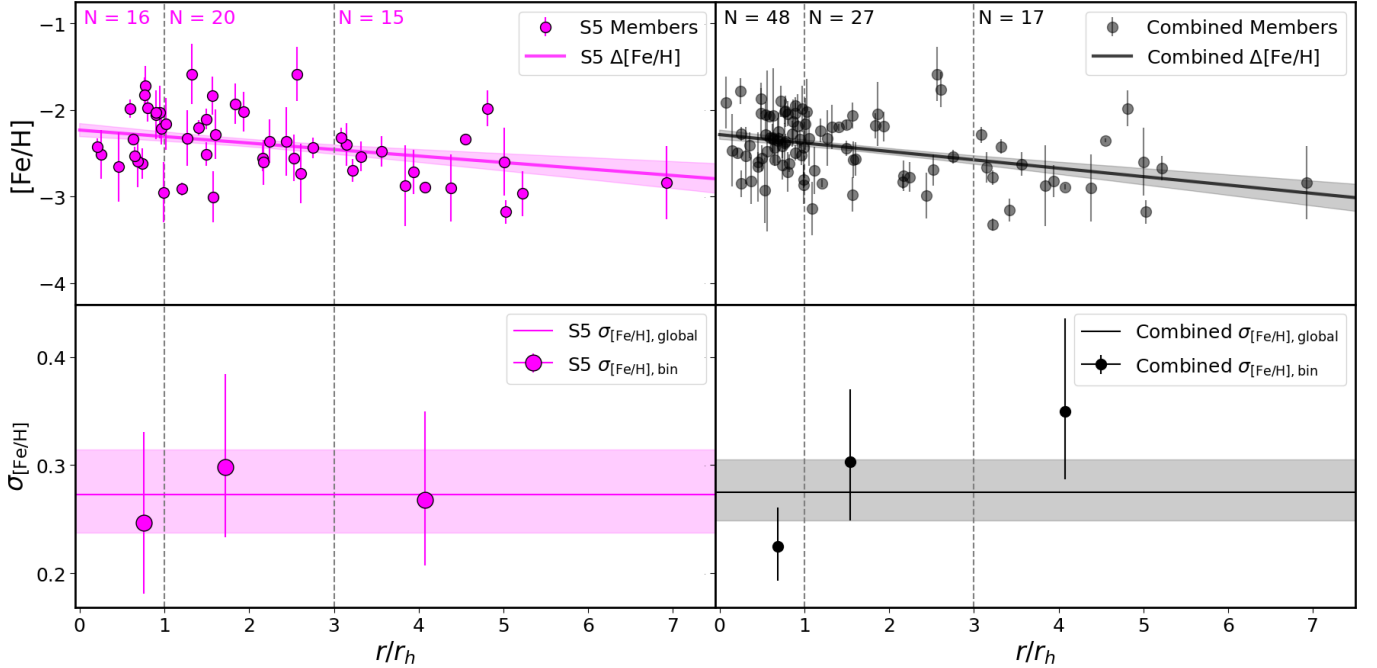


Figure 9. Top. Distribution of stellar metallicity as a function of radius for high probability Boo I members in the S^5 (left; magenta circles) and combined (right; black circles) datasets. The inferred metallicity gradients and their 1σ uncertainty are represented by the solid line and shaded region. **Bottom.** Metallicity dispersion of Boo I members in radial bins of $r/r_h < 1$, $1 \leq r/r_h < 3$, and $r/r_h \geq 3$ for the S^5 (left; magenta circles) and combined (right; black circles) datasets. For comparison, we include the global metallicity dispersions inferred from these datasets (solid lines and shaded regions).

(see Equations C6 and C7; Hernquist 1990; Zhao 1996) that is in dynamical equilibrium such that the motions of its stars can be described by the axisymmetric Jeans equations with a constant velocity anisotropy (see Equations C1–C3; e.g., Cappellari 2008). The stellar distribution is assumed to follow an axisymmetric Plummer profile (Plummer 1911, see Equations C4 and C5) that is aligned with the underlying dark matter halo. This mass model has 8 free parameters:

- Q , the axial ratio of the axisymmetric dark matter halo.
- b_{halo} , the scale radius of the dark matter halo.
- ρ_0 , the central density of the dark matter halo.
- β_z , the velocity anisotropy parameter.
- β , the outer slope of the dark matter halo.
- γ , the inner slope of the dark matter halo.
- α , the sharpness of the dark matter slope transition.
- i , the inclination angle.

We fit this model to the un-binned velocity dispersion profile of our data assuming a Gaussian line-of-sight velocity dispersion. We adopt broad uniform priors (see Table 4) and estimate the posterior distribution using

Markov chain Monte Carlo (MCMC) sampling. In our analysis, we consider only the 56 (115) Boo I member stars in our S^5 (combined) dataset that have good velocity measurements and are not flagged as RRL or binary stars.

The parameters inferred from our dynamical analysis are summarized in Tables 3 and 5. The posterior distributions are presented in Figure C3. Despite the expanded dataset, we find that Q , α , β , and i remain largely unconstrained and recover the well-known $b_{\text{halo}}-\rho_0$ and $Q-\beta_z$ degeneracies (e.g., Binney & Tremaine 2008; Cappellari 2008; Geringer-Sameth et al. 2015; Hayashi & Chiba 2015; Hayashi et al. 2020, 2023). Mild degeneracies are also found for γ with ρ_0 . Nevertheless, the combined dataset is able to reasonably constrain b_{halo} ($\log_{10} b_{\text{halo}} = 3.07^{+0.87}_{-0.45}$), ρ_0 ($\log_{10} \rho_0 = -1.88^{+0.90}_{-1.51}$), and β_z ($-\log_{10}(1-\beta_z) = 0.25^{+0.21}_{-0.21}$). Q , α , β , and i , however, remain largely unconstrained.

We find that the inner dark matter slope is weakly constrained by the combined (S^5) dataset to be $\gamma = 1.00^{+0.52}_{-0.60}$ ($1.27^{+0.48}_{-0.74}$). Though this result favors a cuspy dark matter profile ($\gamma \gtrsim 1$) consistent with expectations from cold dark matter cosmology and our current understanding of galaxy evolution (e.g., Bullock & Boylan-Kolchin 2017, and references therein), we are unable to completely rule out the presence of a core ($\gamma \sim 0$).

In Figure 10, we compare the dark matter profile inferred from our analysis of the S^5 (left) and combined datasets (right) to the dark matter profile previously inferred by Hayashi et al. (2023) using VLT data alone (gray line and shaded region). The size and spatial distribution of each sample is illustrated by the inset histograms in each panel. Though our inferred parameters are consistent within 1σ uncertainties of those reported by Hayashi et al. (2023), our analysis favors a cuspier and less spatial extended halo. This is in large part due to improved constraints on b_{halo} and β_z (see Table 5) enabled by our larger and more radially extended samples.

This analysis highlights that even with a doubling of the l.o.s. velocity measurements and one of the largest kinematics samples in any UFD, the shape of Boo I’s dark matter halo remains poorly constrained. This result is inline with several recent theoretical studies have concluded that much larger samples (i.e., $\mathcal{O}(10^3)$ – $\mathcal{O}(10^4)$ stars) are required to discriminating between cusped and cored dark matter halos with Jeans modeling (e.g., Chang & Necib 2021; Guerra et al. 2023).

6.1. Jeans Modeling Limitations

There are two primary factors that complicate the interpretation of the dynamical modeling presented above, both of which are related to presence of a velocity gradient discussed in Section 5.1. First, the model of Hayashi et al. (2023) used in this work adopts the steady-state Jeans equations, which assumes dynamical equilibrium. However, if the velocity gradient found in Boo I is indicative of tidal disruption, then this assumption is invalid. While the presence of tidal disruption does not necessarily bias or invalidate the results of dynamical modeling of dwarf galaxies, particularly if contamination from unbound stars is minimal as is likely the case for our dataset (e.g., Read et al. 2018; Genina et al. 2020; De Leo et al. 2024; Nguyen et al. 2025), we have not tested our model on simulations of galaxies impacted by tides. Thus we have not quantified what effects tides might have on the inferred dynamical parameters. Second, the model of Hayashi et al. (2023) used in this work assumes that the streaming motion of stars in UFDs is negligible and thus does not account for the possibility that Boo I may be rotating about its minor axis. In principle, this can be addressed by relaxing the assumption of zero streaming motion in the axisymmetric Jeans equations.

The results of our Jeans analysis are also limited by other modeling assumptions outlined in Hayashi et al. (2020) and Hayashi et al. (2023), including the choice of priors, shape of the stellar distribution, and Gaussian line-of-sight velocity distributions. As discussed in these works and in the literature (e.g., Read et al. 2021), these assumptions may bias our results to favor cuspier dark matter profiles. Lastly, the presence of binaries in our data can inflate the velocity dispersion of Boo I. Though

we have done our best to remove binaries, it is inevitable that there remain undetected binaries in our dataset.

In light of these limitations, we recommend that additional modeling of the Boo I mass profile be undertaken that more appropriately takes into account the potential presence of tidally induced disequilibrium and/or rotational motion. Additional radial velocity monitoring should also be undertaken to identify and confirm the binarity of stars in Boo I. Such analysis is beyond the scope of this paper.

7. CHEMICAL EVOLUTION MODELING

The stellar metallicity distribution function (MDF) of a galaxy encodes valuable insight into the physical processes governing the galaxy’s formation and chemical evolution (e.g., star formation, nucleosynthesis, stellar feedback, and gas in/outflows). As the most luminous nearby UFD, Boo I’s well-sampled MDF has been the subject of numerous qualitative and quantitative analyses (e.g., Lai et al. 2011; Gilmore et al. 2013; Vincenzo et al. 2014; Romano et al. 2015; Webster et al. 2015; Romano et al. 2019; Lacchin et al. 2020; Rossi et al. 2024). The additional member stars identified in this work yield a substantial increase to the number of stars in Boo I with well-measured $[\text{Fe}/\text{H}]$ abundances. With 51 $[\text{Fe}/\text{H}]$ measurements, the S^5 dataset is one of the largest homogeneous samples of $[\text{Fe}/\text{H}]$ in Boo I while the combined dataset of 92 $[\text{Fe}/\text{H}]$ measurements represent a $\sim 30\%$ increase over existing samples and the largest sample of spectroscopic metallicities in any UFD by a factor of ~ 2 . As such, a re-analysis of Boo I’s chemical evolution is warranted. Here, we only consider measurements of $[\text{Fe}/\text{H}]$ from our S^5 and combined datasets, saving a joint fit with other individual elemental abundances (e.g., $[\text{C}/\text{Fe}]$, $[\text{Mg}/\text{Fe}]$) measured from high-resolution observations (e.g., Norris et al. 2010b; Gilmore et al. 2013; Ishigaki et al. 2014; Waller et al. 2023) for a future analysis.

To constrain the chemical enrichment history of Boo I, we fit the MDF of Boo I with the analytic galactic chemical evolution (GCE) model of Weinberg et al. (2017) (hereafter WAF17), which was previously applied to the UFD Eridanus II by Sandford et al. (2024). We provide a brief summary of the model and fitting methods in Appendix D, and direct the reader to Weinberg et al. (2017) and Sandford et al. (2024) for a more detailed description and discussion of the model. In short, this GCE model tracks the time evolution of elements in a fully-mixed, one-zone system undergoing gas accretion, star formation, prompt enrichment from core-collapse supernovae (CC SNe), delayed enrichment from Type Ia supernovae (SN Ia), and stellar feedback-driven galactic outflows. It is parameterized in terms of 4 parameters:

- τ_{SFH} , the star formation history (SFH) timescale assuming a linear-exponential form for the SFH ($\dot{M}_* \propto e^{-t/\tau_{\text{SFH}}}$).

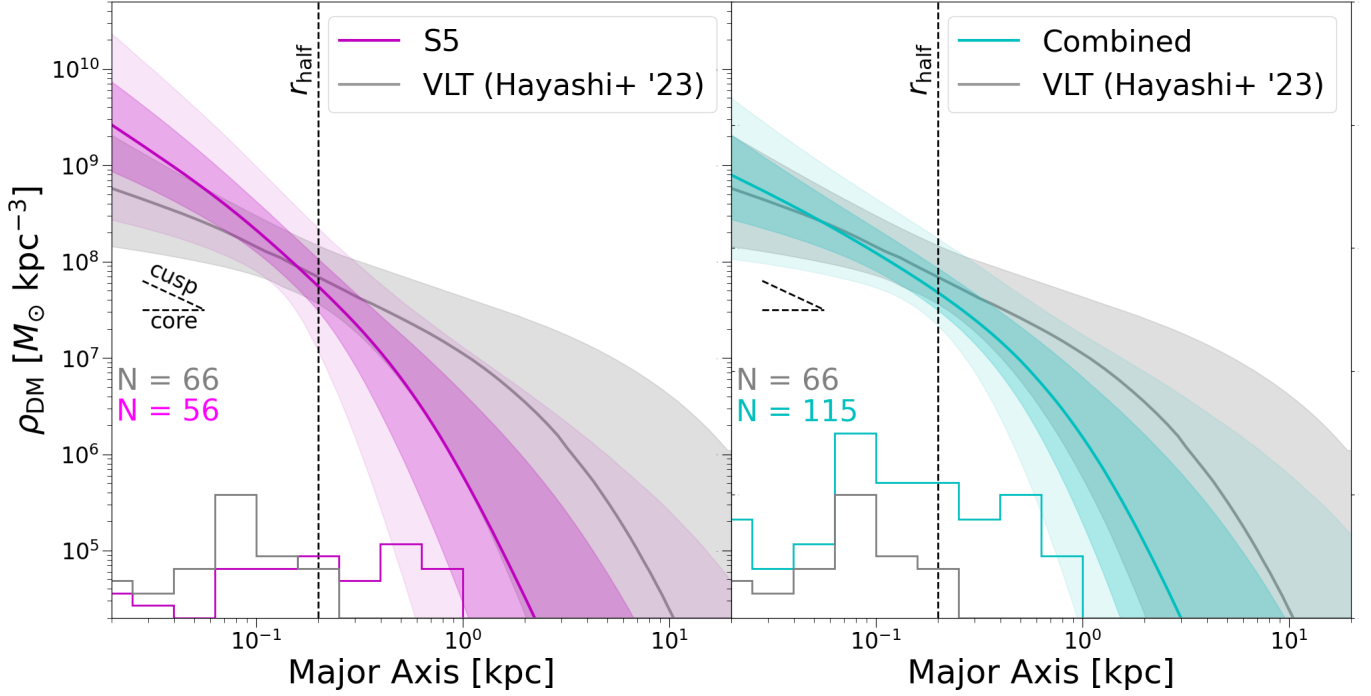


Figure 10. Inferred dark matter density profile along the major axis for the default S^5 (left) and combined (right) datasets. In each panel, the solid lines show the median value of posterior samples, while the dark and light shaded regions show the 68% and 95% confidence intervals respectively. The gray solid lines and shaded regions in each panel provide the median and 68% confidence intervals from Hayashi et al. (2023), which only uses the archival VLT data. The vertical dashed lines indicate the Boo I’s half-light radius from Muñoz et al. (2018). The inset histograms illustrate the spatial distribution of our samples (colored lines) along the semi-major axis compared to the previous VLT-only sample (gray line).

- t_{trunc} , the time at which the SFH truncates (e.g., due to abrupt quenching from ram-pressure stripping or reionization).
- τ_{SFE} , the star formation efficiency (SFE) timescale assuming a linear star formation law ($\tau_{\text{SFE}} = \text{SFE}^{-1} = \dot{M}_g / \dot{M}_*$).
- η , the mass-loading factor describing the ejection of gas from the interstellar medium, assuming a linear scaling with the SFR ($\eta = \dot{M}_{\text{outflow}} / \dot{M}_*$).

To infer the values of these parameters, we adopt the likelihood function given by Equation D13 and adopt weakly informative priors motivated by the CMD-based SFH from Durbin et al. (2025, see Table 4). Sampling is performed using `pocoMC` in the same manner as described in Section 4.2.

The GCE parameters of Boo I inferred from our analysis are summarized in Tables 3 and 5. Their posterior distributions are presented in Appendix D. In Figure 11, we present the results of our fit to the S^5 (top left; magenta) and combined (top right; black) MDFs. The red dashed line shows the “best-fit” model MDF predicted by the *maximum a posteriori* GCE parameters from the sampling. To better compare the continuous and noiseless model MDF to the observed MDF, we make mock MDFs by drawing models repeatedly from

the posterior distribution and sampling stars from their predicted MDF and the uncertainty distribution of the observed data. The median and 68%/95% confidence intervals of this posterior predictive check (PPC) are represented by the solid blue line and shaded regions. The bottom panels show the same data and models, except using the cumulative MDF (cMDF) to provide an alternative visualization. In both cases, we find excellent agreement between draws from our posteriors and the observed (c)MDFs.

From both the S^5 and combined MDFs, we infer the SFH timescale to be $\tau_{\text{SFH}} = 0.2 \pm 0.1$ Gyr. While the data is sufficient to disfavor the shortest SFH timescales (< 150 Myr), the inference of τ_{SFH} is dominated by the tight priors set by CMD-based SFH (80–350 Myr). We are also unable to recover a clear truncation of the SFH before 2 Gyr from either the S^5 or combined dataset, though we are able to place 95% confidence lower limits of $t_{\text{trunc}} > 0.4$ Gyr and > 0.5 Gyr from the respective datasets. As previously discussed in the context of Eridanus II by Sandford et al. (2024), the inability to detect or constrain a sharp truncation in the SFH is expected for systems with short SFH timescales as the abrupt cessation of star formation imprints only a subtle signature on the MDF after a few times the τ_{SFH} .

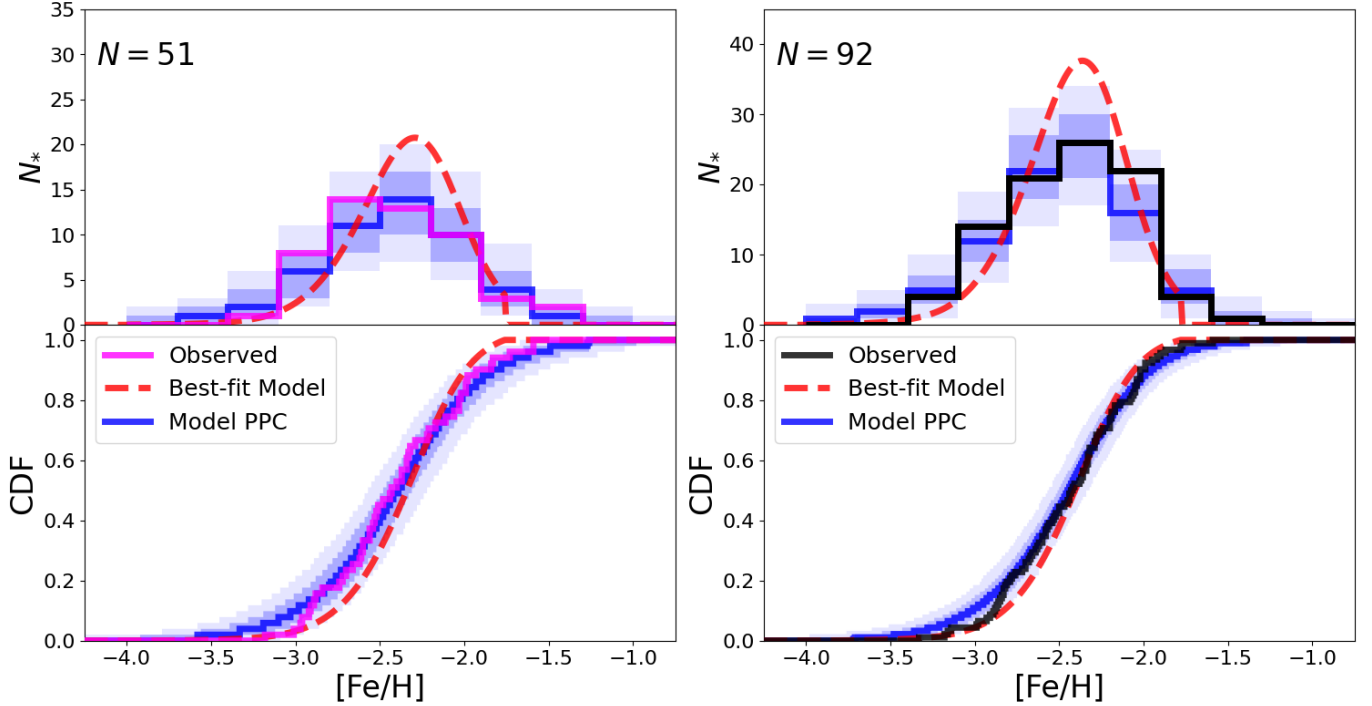


Figure 11. **Left.** MDF (top) and cMDF (bottom) of the S^5 dataset (magenta lines). The dashed red lines show the MDF and cMDF corresponding to the *maximum a posteriori* values from the GCE modeling, while the solid blue lines and shaded regions show the median and 68/95% confidence intervals of the posterior sample when adopting characteristic observational uncertainties. **Right.** Same for the combined dataset with the observed MDF and cMDF represented by black lines.

For the SFE timescale, we infer $\tau_{\text{SFE}} = 11.9^{+8.7}_{-5.1}$ Gyr and $13.9^{+7.6}_{-5.3}$ Gyr from the S^5 and combined datasets respectively. This is equivalent to constraints on the SFE (τ_{SFE}^{-1}) of $\text{SFE} = 0.08^{+0.06}_{-0.04} \text{ Gyr}^{-1}$ and $0.07^{+0.04}_{-0.03} \text{ Gyr}^{-1}$. As can be seen in Figure D4, the τ_{SFE} is mildly degenerate with τ_{SFH} such that a more extended period of star formation would require more inefficient star formation to match the data and vice versa.

Lastly, we infer a mass-loading factor of $\eta = 170^{+35}_{-46}$ from the S^5 MDF and 203^{+27}_{-36} from the combined MDF. In other words, for every $1 M_{\odot}$ of star formation, $\sim 200 M_{\odot}$ of gas is ejected from the ISM. We note that the S^5 MDF allows for a lower mass-loading factor if $t_{\text{trunc}} \lesssim 0.5$ Gyr, but this regime is strongly disfavored by the combined dataset.

7.1. Comparison to Previous GCE Studies of Boo I

Lai et al. (2011) and J21 previously analyzed MDFs of Boo I using three toy models: a “pristine” or “leaky box” model, a “pre-enriched” model, and an “extra gas” model (see Kirby et al. 2011 for details). Both studies found a slight preference for the extra gas model, indicating the importance of including the accretion of pristine gas over the star forming lifetime of Boo I. Due to the difference in parametrization of these models compared to the WAF17 model, it is difficult to draw direct quantitative comparisons between these analyses and our own. However, we note that the extra gas model

is the most qualitatively similar to the WAF17 GCE model. Additionally, both Lai et al. (2011) and J21 infer very low values for their models’ effective yield parameter, which is qualitatively consistent with the large mass-loading factor inferred in this work. A large degree of mass loss was also argued for by Gilmore et al. (2013).

More complex, semi-analytic and numerical models have also been used to study the chemical enrichment of Boo I (e.g., Vincenzo et al. 2014; Romano et al. 2015; Lacchin et al. 2020). However, unlike in Lai et al. (2011), J21, and our own analysis, these previous studies did not perform a statistical fit to the data, but rather investigate a coarse grid of model parameters to see which matched the observed data most closely. Vincenzo et al. (2014), Romano et al. (2015), and Lacchin et al. (2020) all fix the mass-loading factor to $\eta \sim 10$, which is much smaller than value we infer. For this fixed mass-loading factor, Vincenzo et al. (2014) and Lacchin et al. (2020) found that the stellar chemistry of Boo I was best reproduced with an SFE of 0.01 Gyr^{-1} , while Romano et al. (2015) found that slightly large SFE values between 0.013 and 0.053 Gyr^{-1} produced the best results. Our inferred SFE is higher, though still consistent with Romano et al. (2015), which we attribute to the higher mass-loading factor found in our analysis.

Our GCE model, like that of Romano et al. (2015), is unable to explain the absence of gas in Boo I at present

day, requiring that an external process like re-ionization or ram pressure stripping remove the gas. This is in contrast to the findings of Vincenzo et al. (2014), which found that stellar feedback is sufficient to expel Boo I’s remaining gas.

In an investigation of potential Pop III enrichment scenarios in Boo I, Rossi et al. (2024) reported a mass-loading factor of $\eta = 85 \pm 12$. The factor of ~ 2 difference can easily be explained by differences in the adopted nucleosynthetic yields or the treatment of direct ejection of supernova products (see Romano et al. 2019; Weinberg et al. 2023). Lastly, our constraints on τ_{SFH} and t_{trunc} are broadly consistent with previous analyses requiring the duration of star formation in Boo I to be at least 100 Myr (e.g., Gilmore et al. 2013; Webster et al. 2015).

7.2. Comparison to Other Galaxies and Simulations

Here we compare our inferences of Boo I’s SFE and mass-loading factor to values measured or inferred for other galaxies across a range in stellar mass. Though the methods underlying each of these values vary substantially, a cohesive picture of how these galaxy properties correlate with stellar mass nevertheless emerges.

In Figure 12, we compare the mass-loading factor we infer for Boo I from the S^5 and combined dataset (magenta and black stars respectively) to the mass-loading factor inferred by other dwarf galaxy chemical evolution studies (e.g., Limberg et al. 2022; Johnson et al. 2023; Kado-Fong et al. 2024; Sandford et al. 2024), as well the mass-loading factors inferred from direct observations of galactic outflows in nearby star forming galaxies (e.g., Heckman et al. 2015; Chisholm et al. 2017; McQuinn et al. 2019; Eggen et al. 2022). In addition, we include the scaling relation between stellar mass and mass-loading factor $\eta = 0.6 \times (M_*/10^{10} \text{ M}_\odot)^{-0.45}$ measured by Pandya et al. (2021) in FIRE-2 cosmological simulations (Hopkins et al. 2018).

As discussed in Sandford et al. (2024), drawing direct comparisons between mass-loading factors measured through direct observational indicators, those measured in hydrodynamic simulations, and those inferred from GCE models is challenging. This is in part because the parameterization of outflows in GCE models frequently does not map neatly to observable quantities tracing galactic outflows or to the quantities tracked in hydrodynamic simulations. For example, in the WAF17 model, η parameterizes gas that is permanently removed from the reservoir of gas available for star formation, but in both reality and hydrodynamic simulation, a portion of this gas may be retained by a galaxy in a hot-gas phase that is similarly unavailable for star formation even if it is not ejected.

Additionally, the strength of galactic outflows experienced by galaxies observed at $z = 0$ may not be representative of star formation rate-averaged outflows experienced by the same galaxy at high redshift. Furthermore, GCE-based mass-loading factors are strongly

degenerate with the adopted stellar yields, which are uncertain to a factor of ~ 2 (e.g., Griffith et al. 2021; Weinberg et al. 2023), and the degree to which metals are directly ejected from the galaxy by SN explosions. Propagating these uncertainties leads to an additional factor of ~ 2 – 3 uncertainty in the inferred mass-loading factor¹¹. Nevertheless, our result for Boo I is in good agreement with both the theoretical predictions from hydrodynamic simulations and the emerging trend of increasing mass-loading factor with decreasing stellar mass.

In Figure 13, we compare the SFE we infer for Boo I to the SFE reported by GCE analyses of 16 Local Group dwarf galaxies spanning a wide range in stellar masses (Lanfranchi & Matteucci 2004; Lanfranchi et al. 2006; Lanfranchi & Matteucci 2007, 2010; Vincenzo et al. 2014; Romano et al. 2015; Lacchin et al. 2020; Alexander et al. 2023; Sandford et al. 2024). Though the assumptions made by the included GCE models vary greatly, there is a clear trend between SFE and galaxy mass—albeit with appreciable scatter. While slightly high given Boo I’s mass, the SFE we infer is in reasonable agreement with expectations that less massive galaxies are less efficient at converting gas to stars.

8. SUMMARY

In this paper, we present a comprehensive analysis of new and archival spectroscopic observations in the ancient, dark matter-dominated UFD Boo I. Our key results when using the combined dataset are as follows:

- We create a combined dataset of 148 member stars extending our to $\sim 7r_h$, including 24 newly confirmed members, 18 binary candidates, and 15 RRL stars. Of these member stars, 115 have good non-variable radial velocities suitable for dynamical analyses, and 92 have good [Fe/H] measurements suitable for chemical evolution analyses.
- We leverage the 16-year time baseline of our dataset to identify 15 new binary candidates, which we remove from our dynamical analysis.
- We infer a mean systemic velocity of $\langle v \rangle = 103.0 \pm 0.4 \text{ km s}^{-1}$ and a velocity dispersion of $\sigma_v = 4.0^{+0.4}_{-0.3} \text{ km s}^{-1}$. Accounting for the effects of perspective rotation, we infer an intrinsic l.o.s. velocity gradient of $\Delta v = 0.12^{+0.04}_{-0.03} \text{ km s}^{-1} \text{ arcmin}^{-1}$ ($1.2^{+0.4}_{-0.3} \text{ km s}^{-1} r_h^{-1}$) aligned with Boo I’s orbit, which is significantly shallower than previously reported by L22.
- We infer a mean metallicity of $\langle [\text{Fe}/\text{H}] \rangle = -2.43 \pm 0.4$, a metallicity dispersion of $\sigma_{[\text{Fe}/\text{H}]} =$

¹¹ This may explain why the CGE results are systematically higher than the predictions of Pandya et al. (2021).

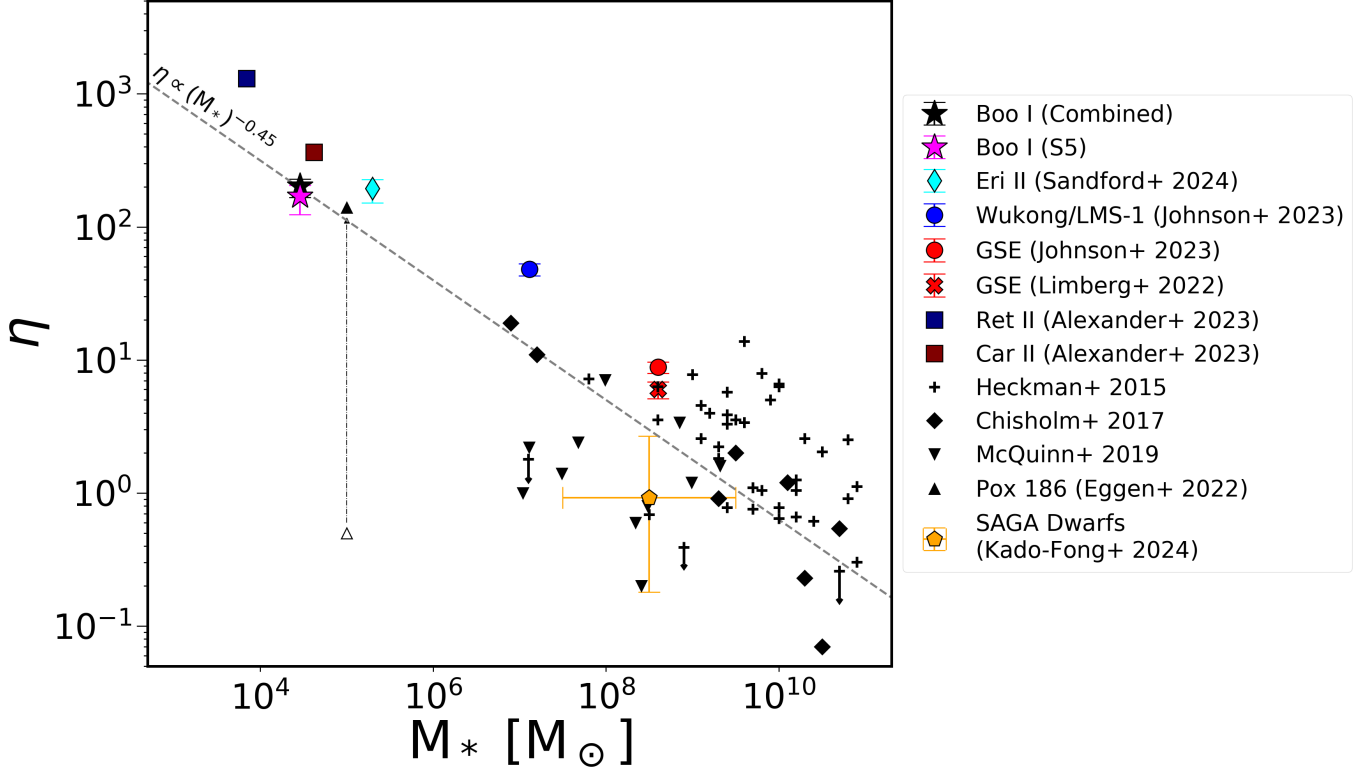


Figure 12. The inferred mass-loading factor of Boo I from the S^5 and combined datasets (magenta and black stars respectively) compared to the mass-loading factors inferred by the chemical evolution studies of Johnson et al. (2023) for Wukong/LMS-1 and GSE (blue and red circles respectively), Limberg et al. (2022) in GSE (red “x”), Alexander et al. (2023) for Carina II and Reticulum II (navy and maroon squares respectively), and Sandford et al. (2024) for Eridanus II (cyan diamond) as a function of stellar mass. The mass-loading factors inferred by the evolution of the mass-metallicity relation in the SAGA background dwarf galaxy sample by Kado-Fong et al. (2024) is included as an orange pentagon. Mass-loading factors for galaxies observed by Heckman et al. (2015), Chisholm et al. (2017), and McQuinn et al. (2019) are included as black pluses, diamonds, and triangles respectively. The current observed mass-loading factor of Pox 186 and its previous estimated mass-loading factor from Eggen et al. (2022) are represented by the open and filled black triangle respectively. The scaling found by Pandya et al. (2021) in FIRE-2 simulations indicative of energy-driven winds ($\eta \propto M_*^{-0.45}$) is included for reference as the dashed gray line.

0.28 ± 0.03 , and a weak but resolved radial metallicity gradient of $\Delta[\text{Fe}/\text{H}] = -0.010 \pm 0.003 \text{ dex arcmin}^{-1}$ ($-0.10 \pm 0.03 \text{ dex } r_h^{-1}$).

- We provide updated constraints on Boo I’s dark matter density profile using axisymmetric Jeans modeling. Our larger and more spatially extended dataset favors a cuspy dark matter halo ($\gamma = 1.0^{+0.52}_{-0.60}$) but still cannot rule out a cored profile.
- We find that Boo I’s MDF can be reproduced with a one-zone GCE featuring rapid ($\tau_{\text{SFH}} = 0.2 \pm 0.1 \text{ Gyr}$) and inefficient ($\text{SFE} = 0.07^{+0.04}_{-0.03} \text{ Gyr}^{-1}$) star formation and large stellar feedback-driven outflows ($\eta = 203^{+27}_{-36}$) in agreement with previous GCE modeling of other UFDs.

In addition to the above results, we discuss the implications of Boo I’s intrinsic velocity gradient, but are unable to conclusively rule out either rotational or tidal ori-

gins. The alignment of Boo I’s elongation, orbit, and velocity gradient, support previous arguments that Boo I is undergoing tidal disruption—or has at least experienced tidal deformation as a result of its repeated pericentric passages (e.g., Roderick et al. 2016; Muñoz et al. 2018; Longeard et al. 2022). We also find that despite Boo I’s rapid star formation, its metallicity dispersion can be explained by self-enrichment without requiring either mergers or inhomogeneous mixing. These results suggest that the extended stellar population is more likely the result of tidal effects than a dry merger. However, it is difficult with the current data to definitively confirm the presence of tidal disruption and rule out the alternative or additional scenario of a past merger. For example, our observations, though wide field, still do not extend beyond Boo I’s estimated tidal radius, precluding the detection of extra-tidal stars. Moreover, dynamical simulations of a Boo I-like galaxy on a Boo I-like orbit are unable to reproduce the observed velocity gradient, predicting instead that a tidally-induced ve-

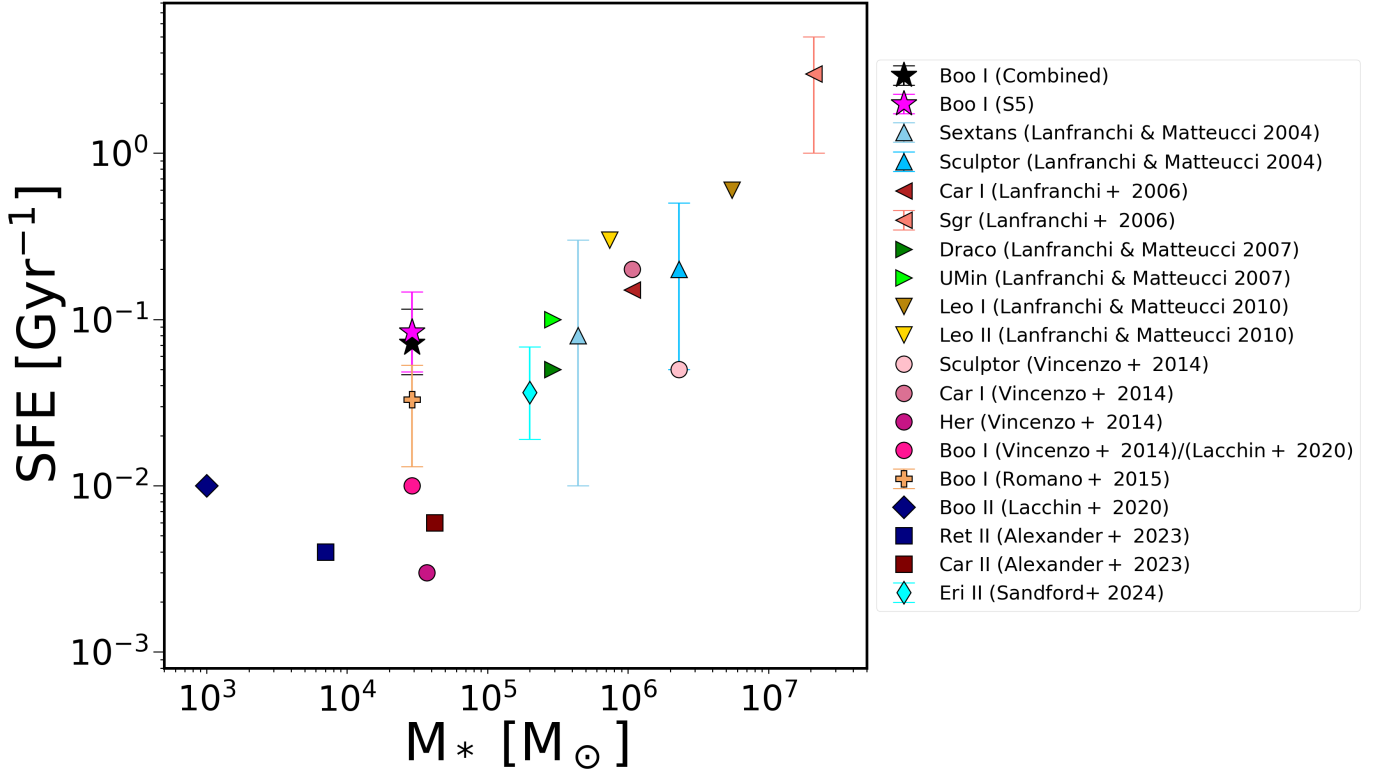


Figure 13. The inferred SFE of Boo I from the S^5 and combined datasets (magenta and black stars respectively) compared to the SFEs reported by previous chemical evolution studies of LG dwarf galaxies (Lanfranchi & Matteucci 2004; Lanfranchi et al. 2006; Lanfranchi & Matteucci 2007, 2010; Vincenzo et al. 2014; Romano et al. 2015; Lacchin et al. 2020; Alexander et al. 2023; Sandford et al. 2024).

licity gradient should only be observed at larger radii than our observations cover.

More conclusive statements will require a larger homogeneous dataset in which the selection function is well-characterized as will be the case from upcoming spectroscopic surveys (DESI; DESI Collaboration et al. 2016, PFS; Takada et al. 2014). In particular, datasets that will provide robust and homogeneous $[\alpha/\text{Fe}]$ (or neutron capture elements) both within one half-light radius and out beyond $5r_h$ will be needed to test whether the extended features are in fact chemically distinct. Detection of extra-tidal stars that have been stripped from Boo I will also provide valuable insight into Boo I’s dynamic history. In conjunction with additional spectroscopic data, more rigorous dynamical modeling will also aid in the interpretation of Boo I’s chemodynamic evolution. Nevertheless, the work presented in this paper firmly establishes Boo I as a premier astrophysical laboratory for studying dark matter and galaxy evolution in low-mass satellite galaxies.

ACKNOWLEDGMENTS

We thank Marla Geha for valuable feedback and discussion regarding this work. NRS acknowledges support from an Arts & Science Postdoctoral Fellowship at the University of Toronto. NRS, GEM and TSL acknowl-

edge financial support from Natural Sciences and Engineering Research Council of Canada (NSERC) through grant RGPIN-2022-04794. NRS and JB acknowledge financial support from NSERC (funding reference number RGPIN-2020-04712). SEK acknowledges support from the Science & Technology Facilities Council (STFC) grant ST/Y001001/1. KH acknowledges supports from Grant-in-Aid for Scientific Research from the Ministry of Education, Culture, Sports, Science, and Technology (MEXT), Japan, grant numbers JP24K00669 and JP25H01553.

This paper includes data obtained with the Anglo-Australian Telescope in Australia and hosted on AAO Data Central (datacentral.org.au). We acknowledge the traditional owners of the land on which the AAT stands, the Gamilaraay people, and pay our respects to elders past and present.

This work has made use of data from the European Space Agency (ESA) mission *Gaia* (<https://www.cosmos.esa.int/gaia>), processed by the *Gaia* Data Processing and Analysis Consortium (DPAC, <https://www.cosmos.esa.int/web/gaia/dpac/consortium>). Funding for the DPAC has been provided by national institutions, in particular the institutions participating in the *Gaia* Multilateral Agreement.

This work has also made use of data collected at the European Organisation for Astronomical Research in the Southern Hemisphere under ESO programs 82.B-0372(A), 185.B0946(A) and 185.B-0946(B).

Lastly, this work has made use of data in the Local Volume Database (Pace 2024).

For the purpose of open access, the authors have applied a Creative Commons Attribution (CC BY) license to any Author Accepted Manuscript version arising from this submission.

Facilities: AAT (AAOmega+2dF), MMT (Hectochelle), VLT (GIRAFFE), *Gaia*

Software: agama (Vasiliev 2019), astropy (Astropy Collaboration 2013; Astropy Collaboration et al. 2018, 2022), astroquery (Ginsburg et al. 2019), corner (Foreman-Mackey 2016), emcee (Foreman-Mackey et al. 2013), GADGET-3 (Springel 2005), galpy (Bovy 2015), matplotlib (Hunter 2007), numpy (Harris et al. 2020), pandas (McKinney 2010; Team 2024), pocoMC (Karamanis et al. 2022a,b), RVSpecFit (Koposov et al. 2011; Koposov 2019), scipy (Virtanen et al. 2020)

APPENDIX

A. CATALOG OF STARS

In Table A1, we provide a description of the columns for the the combined stellar catalog analyzed in this work. The dataset is made available in machine-readable format.

B. ANALYSIS OF ARCHIVAL DATASETS

In this section, we present the independent analysis of the archival AAT and MMT datasets and compare the results to the analysis of the S^5 -only and combined datasets. For each of the archival AAT and MMT datasets, we apply the same data quality cuts and GMM as described in Sections 4.1 and 4.2. Prior to fitting with the GMM, the velocity- and [Fe/H]-offsets presented in Table 2 are applied.

Using the same membership threshold of $p_{\text{mem}} > 0.8$ to identify likely members, we find 42 likely members with good velocities in the archival AAT dataset, of which 41 have good metallicities. In the archival MMT dataset, we find 37 likely members with good velocities, of which 33 have good metallicities. We find good agreement between the likely members between the S^5 , archival AAT, and archival MMT datasets—that is, all stars that are found to be members in one dataset are also found to be members in the other datasets in which they are present. The sample of likely Boo I members for each dataset is illustrated in Figure 5.

The systemic properties of Boo I inferred from our GMM analysis of the archival datasets are summarized in Table 5. For nearly all Boo I model parameters, we find the inferred values to be in good agreement between the individual and combined datasets. The only exceptions are the mean metallicity, which we infer to be ~ 0.1 and ~ 0.2 dex lower for the archival AAT and MMT datasets compared to the S^5 , archival VLT, and combined datasets, as well as the metallicity dispersion which we infer to be ~ 0.1 dex larger for the archival AAT and MMT datasets compared to the S^5 , archival VLT, and combined datasets. The MW foreground model parameters differ considerably between the datasets as a result of the different target selections employed by each observing campaign.

Figure B1 illustrates the velocity gradient inferred from the S^5 (top left), archival AAT (top right), archival MMT (bottom left), and archival VLT (bottom right) datasets. We find the velocity gradients in all of the archival datasets to be consistent within 1σ to the results from the S^5 and combined datasets (see Section 5.1). All datasets appear to independently support the existence of a velocity gradient aligned with Boo I’s orbit and/or semi-major axis. The velocity gradient inferred from the archival VLT dataset is very uncertain due to the limited spatial extent of the sample.

As in Section 5.2, we perform a binned velocity dispersion analysis for the individual datasets, which we present in the left panels of Figure B. We find general agreement between the velocity dispersion in each bin for each dataset. Both of the datasets with >10 stars beyond $3r_h$ (S^5 and archival AAT) exhibit a smaller velocity dispersion in the outer bin, in contrast to the increasing velocity dispersion reported by L22.

In the top right panel of Figure B, we present results for the metallicity gradient of the individual datasets. The S^5 , archival AAT, and archival MMT datasets all independently support the existence of a negative radial metallicity gradient with the archival MMT (AAT) dataset exhibiting the strongest (weakest) gradient. We do not attempt to fit a metallicity gradient to the archival VLT dataset due to its small spatial extent, instead we include the mean metallicity reported by J21 for reference. In the bottom right panel of Figure B, we present the binned metallicity

Table A1. Combined Catalog of Stars

Column	Units	Description
<code>gaia_id</code>	...	<i>Gaia</i> Source ID
<code>alt_id</code>	...	Source ID from K11 and J21
<code>RA</code>	deg	Right ascension
<code>Dec</code>	deg	Declination
<code>pmra</code>	mas yr ⁻¹	Proper motion (RA)
<code>pmra_err</code>	mas yr ⁻¹	Proper motion (RA)
<code>pmdec</code>	mas yr ⁻¹	Proper motion uncertainty (dec)
<code>pmdec_err</code>	mas yr ⁻¹	Proper motion uncertainty (dec)
<code>pmra_pmdec_corr</code>	...	Correlation coefficient between <code>pmra</code> and <code>pmdec</code>
<code>vel_avg</code>	kms s ⁻¹	Heliocentric l.o.s. velocity averaged over datasets
<code>vel_err_avg</code>	kms s ⁻¹	Uncertainty on <code>vel_avg</code>
<code>vel_s5</code>	kms s ⁻¹	Heliocentric l.o.s. velocity from the <i>S</i> ⁵ dataset
<code>vel_err_s5</code>	kms s ⁻¹	Uncertainty on <code>vel_err_s5</code>
<code>vel_q_s5</code>	...	Flag for velocities used in the dynamical analysis
<code>vel_aat</code>	kms s ⁻¹	Corrected heliocentric l.o.s. velocity from the archival AAT dataset
<code>vel_err_aat</code>	kms s ⁻¹	Uncertainty on <code>vel_err_aat</code>
<code>vel_q_aat</code>	...	Flag for velocities used in the dynamical analysis
<code>vel_mmt</code>	kms s ⁻¹	Corrected heliocentric l.o.s. velocity from the archival MMT dataset
<code>vel_err_mmt</code>	kms s ⁻¹	Uncertainty on <code>vel_err_mmt</code>
<code>vel_q_mmt</code>	...	Flag for velocities used in the dynamical analysis
<code>vel_vlt</code>	kms s ⁻¹	Corrected heliocentric l.o.s. velocity from the archival VLT dataset
<code>vel_err_vlt</code>	kms s ⁻¹	Uncertainty on <code>vel_err_vlt</code>
<code>vel_q_vlt</code>	...	Flag for velocities used in the dynamical analysis
<code>feh_avg</code>	dex	[Fe/H] averaged over datasets.
<code>feh_err_avg</code>	dex	Uncertainty on <code>feh_avg</code>
<code>feh_s5</code>	dex	[Fe/H] from the <i>S</i> ⁵ dataset.
<code>feh_err_s5</code>	dex	Uncertainty on <code>feh_err_s5</code>
<code>feh_q_s5</code>	...	Flag for [Fe/H] used in the chemical analysis
<code>feh_aat</code>	dex	Corrected [Fe/H] from the archival AAT dataset
<code>feh_err_aat</code>	dex	Uncertainty on <code>feh_err_aat</code>
<code>feh_q_aat</code>	...	Flag for [Fe/H] used in the chemical analysis
<code>feh_mmt</code>	dex	Corrected [Fe/H] from the archival MMT dataset
<code>feh_err_mmt</code>	dex	Uncertainty on <code>feh_err_mmt</code>
<code>feh_q_mmt</code>	...	Flag for [Fe/H] used in the chemical analysis
<code>feh_vlt</code>	dex	Corrected [Fe/H] from the archival VLT dataset
<code>feh_err_vlt</code>	dex	Uncertainty on <code>feh_err_vlt</code>
<code>feh_q_vlt</code>	...	Flag for [Fe/H] used in the chemical analysis
<code>pval</code>	...	<i>p</i> -value from null-hypothesis testing of RV variability
<code>binary</code>	...	Flag indicating binary candidate (<code>pval</code> < 0.1)
<code>mem_p_s5</code>	...	Membership probability in the <i>S</i> ⁵ GMM analysis
<code>mem_p_aat</code>	...	Membership probability in the archival AAT GMM analysis
<code>mem_p_mmt</code>	...	Membership probability in the archival MMT GMM analysis
<code>mem_p_vlt</code>	...	Membership probability from J21 archival VLT analysis
<code>member</code>	...	Flag indicating likely Boo I member

NOTE—Table A1 is published in its entirety in the electronic edition of the *Astrophysical Journal*.

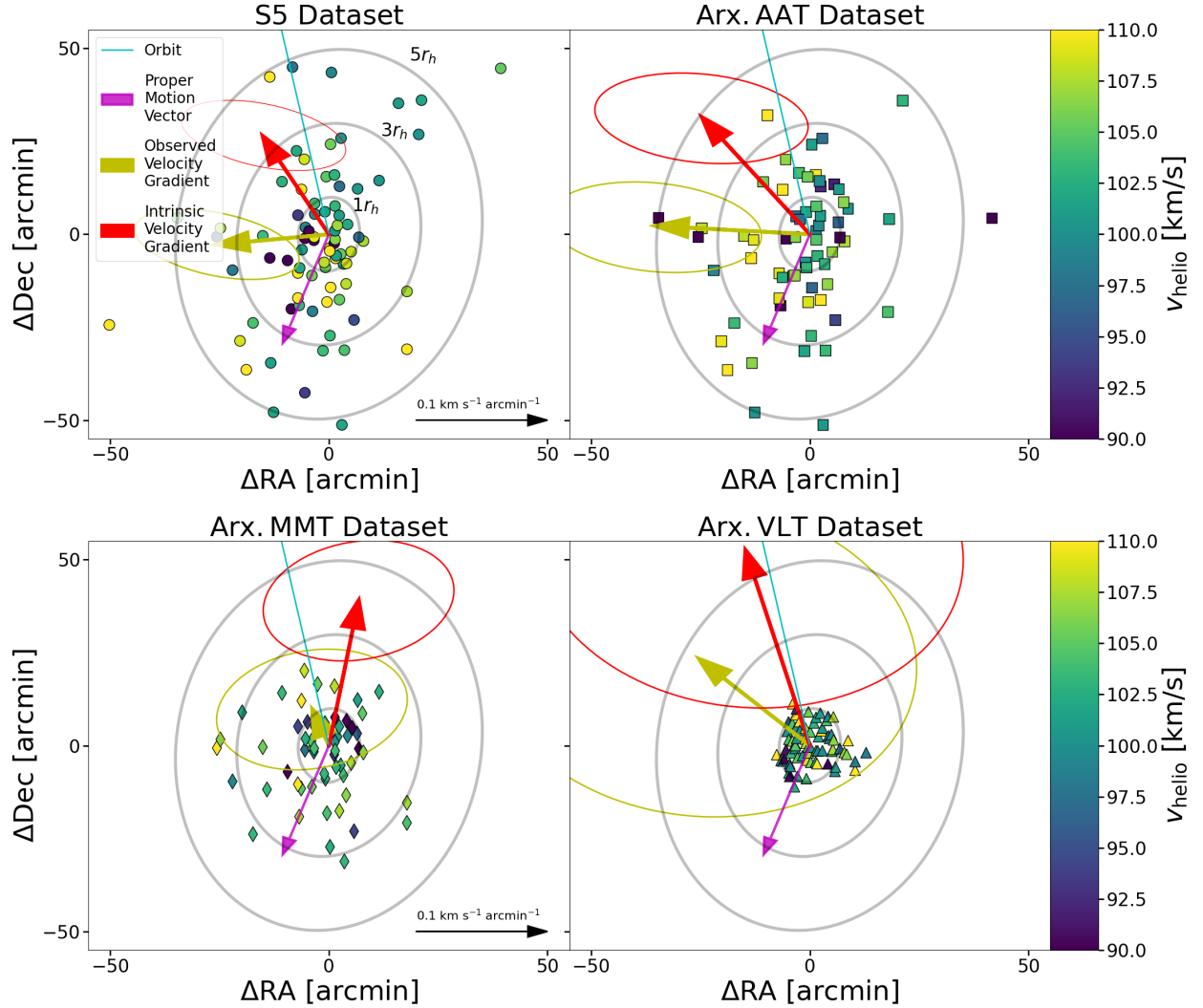


Figure B1. Same as Figure 6 for subsets of the combined dataset, including S^5 (top left), archival AAT (top right), archival MMT (bottom left), and archival VLT (bottom right). Velocity gradients for the S^5 , AAT, and MMT datasets are inferred from the GMM model described in Section 4 and Appendix B, while the velocity gradient for the VLT dataset is inferred directly from the high probability members found in J21.

dispersions of each dataset. We find no evidence for a radially increasing or decreasing metallicity dispersion in any of the datasets.

C. AXISYMMETRIC JEANS MODELING

Here, we provide a brief summary of the axisymmetric Jeans modeling performed in Section 6. For a more complete description of the development of this methodology and its limitations, see Hayashi & Chiba (2012), Hayashi & Chiba (2015), Hayashi et al. (2020) and Hayashi et al. (2023). In brief, we assume that Boo I is an axisymmetric dark matter-dominated system in dynamical equilibrium such that its stellar motions can be described by the axisymmetric

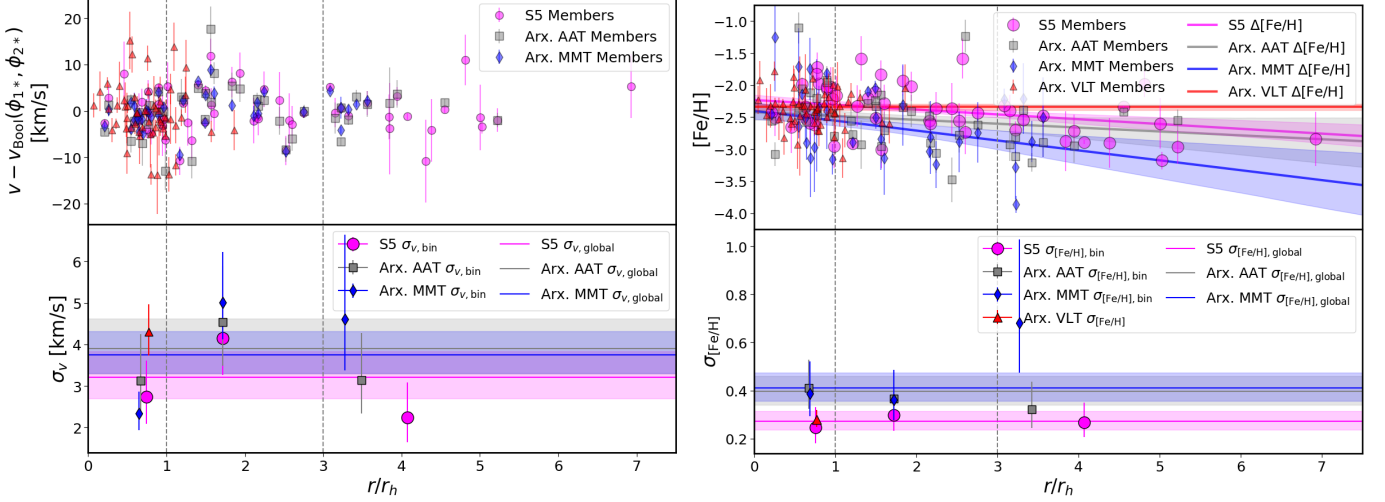


Figure B2. **Left.** Same as Figure 8 including Boo I members from S^5 , archival AAT, W23, J21 and combined datasets (magenta circles, gray squares, blue diamonds, red triangles, and black circles respectively respectively). **Right.** Same as Figure 9 including Boo I members from S^5 , archival AAT, W23, J21 and combined datasets (magenta circles, gray squares, blue diamonds, red triangles, and black circles respectively respectively).

Jeans equations:

$$\overline{v_z^2} = \frac{1}{\nu(R, Z)} \int_z^\infty \nu \frac{\partial \Phi_{\text{DM}}}{\partial z} dz \text{ and} \quad (\text{C1})$$

$$\overline{v_\phi^2} = \frac{1}{1 - \beta_z} \left[\overline{v_z^2} + \frac{R}{\nu} \frac{\partial(\nu \overline{v_z^2})}{\partial R} \right] + R \frac{\partial \Phi_{\text{DM}}}{\partial R}, \quad (\text{C2})$$

where

$$\beta_z = 1 - \overline{v_z^2} / \overline{v_R^2} \quad (\text{C3})$$

is the radially independent velocity anisotropy parameter introduced by Cappellari (2008), ν is the three-dimensional stellar density, and Φ_{DM} is the dark matter halo's gravitational potential.

We model the stellar density profile by with an axisymmetric Plummer model (Plummer 1911):

$$\nu(R, z) = (3/4\pi b_*^3) (1 + r_*^2/b_*^2)^{-5/2}, \quad (\text{C4})$$

where

$$r_*^2 = R^2 + z^2/q^2, \quad (\text{C5})$$

b_* is the half-light radius, and q is the axial ratio of the stellar distribution. This distribution is converted into a surface density profile using an Abel transform and the inclination angle, i , which we define to be the angle between the symmetry axis and the line of sight such that $i = 0^\circ$ corresponds to looking at the galaxy face-on. As in Hayashi et al. (2023), we leave the inclination angle as a free parameter and adopt the projected half-light radius and axial ratio for Boo I from Muñoz et al. (2018), where the intrinsic axial ratio, q , is related to the projected axial ratio, q' , as $q = \sqrt{q'^2 - \cos^2 i} / \sin i$ (Hubble 1926).

For the dark matter halo's gravitational potential, we adopt a generalized axisymmetric Hernquist profile (Hernquist 1990; Zhao 1996):

$$\rho_{\text{DM}}(R, z) = \rho_0 \left(\frac{r}{b_{\text{halo}}} \right)^{-\gamma} \left[1 + \left(\frac{r}{b_{\text{halo}}} \right)^\alpha \right]^{-\frac{\beta-\gamma}{\alpha}}, \quad (\text{C6})$$

where

$$r^2 = R^2 + z^2/Q^2. \quad (\text{C7})$$

Here, ρ_0 and b_{halo} are the scale density and radius of the dark matter halo, respectively; α describes the sharpness of the transition from the inner dark matter slope, γ , and the outer dark matter slope, β ; and Q is the dark matter halo's axial ratio. We assume that the dark matter halo has the same orientation and symmetry axis as the stellar distribution. In summary, this model has 8 free parameters, Q , ρ_0 , b_{halo} , β_z , α , β , γ , and i .

To fit this mass model to our datasets, we assume that the line-of-sight velocity distribution at the location of each star is a Gaussian centered on the mean velocity of the galaxy such that the likelihood function is given by

$$-2 \ln(\mathcal{L}) = \sum_i \left[\frac{(v_i - \langle v_B \rangle)^2}{\sigma_i^2} + \ln(2\pi\sigma_i^2) \right], \quad (\text{C8})$$

where σ_i is the quadrature sum of the velocity uncertainty of the star and the line-of-sight velocity dispersion predicted by the model at the star's position in the plane of the sky. The mean velocity of Boo I $\langle v_B \rangle$ is a nuisance parameter. We adopt the same flat or log-flat priors as Hayashi et al. (2023), which we present in Table 4. Posterior distributions are estimated with MCMC sampling using the Metropolis–Hastings algorithm (Metropolis et al. 1953; Hastings 1970). The resulting posterior distributions of the model parameters for the S^5 (left) and combined (right) are illustrated in Figure C3. Vertical dashed lines provide the median and 1σ confidence intervals for each parameter, while the black stars and vertical solid lines indicate the *maximum a posteriori* values. These results are summarized in Table 5.

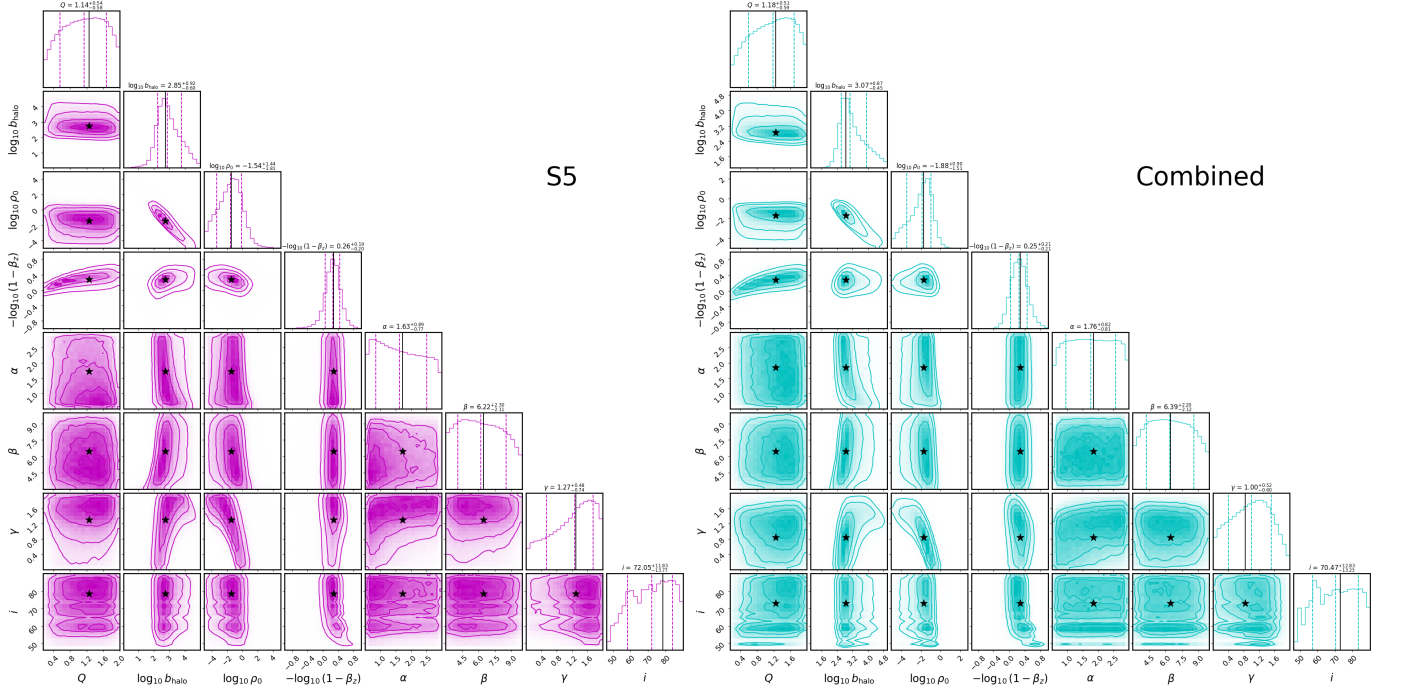


Figure C3. Posterior probability distributions for the dark matter profile parameters for the default S^5 (left) and combined (right) datasets. Vertical dashed lines provide the median and 1σ confidence intervals for each parameter. Black stars and vertical solid lines indicate the *maximum a posteriori* values.

D. CHEMICAL EVOLUTION MODELING

In this appendix, we provide a brief summary of the galactic chemical evolution (GCE) model from Weinberg et al. (2017) (hereafter WAF17) that we use in Section 7. For a more complete description of the model and its previous application to UFDs, see Weinberg et al. (2017) and Sandford et al. (2024) respectively.

In brief, the WAF17 model assumes that the SFR of Boo I can be approximated with a continuous analytic function. In this work, we adopt a linear-exponential functional form for the SFR:

$$\dot{M}_* \propto \begin{cases} t \exp(-t/\tau_{\text{SFH}}), & \text{if } t \leq t_{\text{trunc}} \\ 0, & \text{if } t > t_{\text{trunc}} \end{cases}, \quad (\text{D9})$$

where τ_{SFH} is the SFH timescale and t_{trunc} is the time at which all star formation ceases (e.g., from ram pressure stripping or reionization). Furthermore, the model assumes that star formation is governed by a linear star formation law parameterized by the star formation efficiency (SFE) timescale,

$$\tau_{\text{SFE}} \equiv \text{SFE}^{-1} \equiv M_g / \dot{M}_*, \quad (\text{D10})$$

where M_g and \dot{M}_* are the gas mass and star formation rate (SFR) respectively.

At each timestep, a fraction, r , of the mass formed into stars is immediately returned to the ISM unprocessed without chemical enrichment (e.g., by core-collapse supernovae and asymptotic giant branch stars). As in [Sandford et al. \(2024\)](#), we choose a mass recycling fraction of $r = 0.37$, which [WAF17](#) showed to be an appropriate approximation for the adopted [Kroupa \(2001\)](#) IMF. Additionally, at each timestep, gas is ejected from the ISM via stellar feedback according to a linear scaling with the SFR,

$$\eta = \dot{M}_{\text{outflow}} / \dot{M}_*, \quad (\text{D11})$$

where η is the mass loading factor. In the [WAF17](#) model, the rate of pristine gas accretion from the intergalactic medium is set implicitly such that the depletion of gas by star formation and galactic outflows is sufficiently balanced by gas recycling and galactic inflows:

$$\dot{M}_{\text{inf}} = (1 + \eta - r)\dot{M}_* + \tau_{\text{SFE}}\ddot{M}_* \quad (\text{D12})$$

(see Equation 9 in [WAF17](#)).

Enrichment from CC SNe is assumed to occur instantaneously following star formation, while the enrichment from SNe Ia is assumed to follow a $t^{-1.1}$ power-law delay time distribution with a minimum time delay of $t_D = 0.05$ Gyr as determined empirically by [Maoz et al. \(2012\)](#). We adopt the instantaneous mixing approximation, which has been shown to be a reasonable assumption for CC SNe and SNe Ia products in low-mass, ancient galaxies like Boo I (e.g., [Escala et al. 2018](#)). The [WAF17](#) model parametrizes chemical enrichment using dimensionless IMF-weighted metallicity-independent yield parameters, which represent the mass of elements produced per unit mass of star formation. We adopt the same empirically motivated values as [Sandford et al. \(2024\)](#): a CC SN Fe yield of $y_{\text{Fe}}^{\text{CC}} = 6.0 \times 10^{-4}$ and a SN Ia Fe yield of $y_{\text{Fe}}^{\text{Ia}} = 1.2 \times 10^{-3}$.

In summary, this model has 4 free parameters, τ_{SFH} , t_{trunc} , τ_{SFE} , and η . The priors adopted for each of these parameters are summarized in Table 4. For τ_{SFH} , we adopt a uniform prior from 0.08 to 0.35 Gyr, and for t_{trunc} , we adopt a uniform prior from 0 to 2 Gyr. These choices of priors are informed by [Durbin et al. \(2025\)](#) who derived a SFH for Boo I from deep *HST*/ACS photometry and determined that 50% (90%) of its stars formed by $13.49^{+0.00}_{-0.04}$ ($13.37^{+0.00}_{-1.03}$) Gyr ago. For both $\log(\tau_{\text{SFE}})$ and η , we adopt broad, uniform priors of $0 < \log(\tau_{\text{SFE}}) < 4$ and $0 < \eta < 10^4$ respectively.

As in previous analyses of dwarf galaxy MDFs (e.g., [Kirby et al. 2011](#)), we adopt the following likelihood function:

$$\ln \mathcal{L} = \sum_i \ln \int_{-\infty}^{\infty} \frac{dN}{d[\text{Fe}/\text{H}]} \frac{1}{\sqrt{2\pi}\sigma_{[\text{Fe}/\text{H}],i}} \exp\left(-\frac{([\text{Fe}/\text{H}] - [\text{Fe}/\text{H}]_i)^2}{2\sigma_{[\text{Fe}/\text{H}],i}^2}\right) d[\text{Fe}/\text{H}], \quad (\text{D13})$$

where $\frac{dN}{d[\text{Fe}/\text{H}]}$ is the normalized MDF predicted by the model. Here, $[\text{Fe}/\text{H}]_i$ and $\sigma_{[\text{Fe}/\text{H}],i}$ are once again the measured iron abundance and its uncertainty for each star. Simply put, this equation is the convolution of the model MDF with the observational Gaussian errors. For the [WAF17](#) model,

$$\frac{dN}{d[\text{Fe}/\text{H}]} \propto \frac{\dot{M}_*}{d[\text{Fe}/\text{H}]/dt}. \quad (\text{D14})$$

Sampling of the posterior distribution is performed [pocoMC](#) as described in Section 4.2.

Figure D4 illustrates the resulting posterior distributions of the GCE model parameters for the S^5 (magenta) and combined (black) datasets. The adopted prior distributions are included for reference as solid green lines.

REFERENCES

- | | |
|--|--|
| Abbott, T. M. C., Abdalla, F. B., Allam, S., et al. 2018,
The Astrophysical Journal Supplement Series, 239, 18,
doi: 10.3847/1538-4365/aae9f0 | Adén, D., Wilkinson, M. I., Read, J. I., et al. 2009, The
Astrophysical Journal, 706, L150,
doi: 10.1088/0004-637X/706/1/L150 |
|--|--|

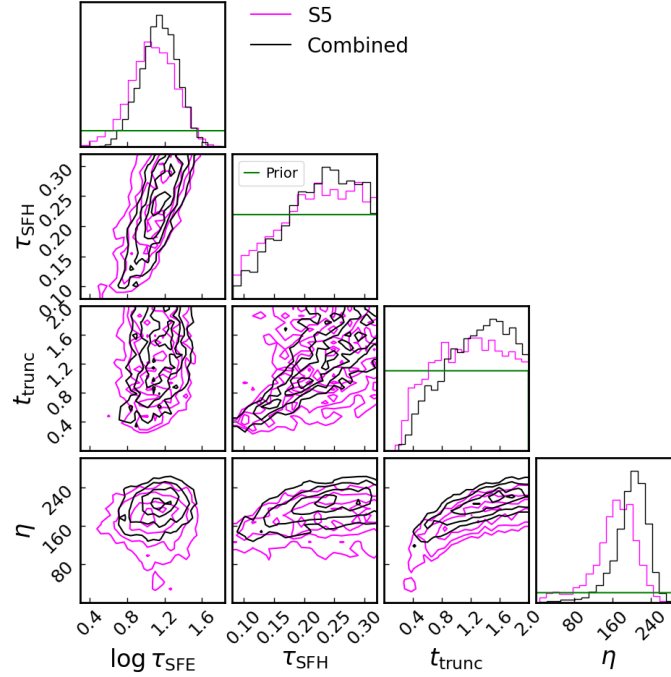


Figure D4. Posterior probability distribution for the galactic chemical evolution model parameters fit to the S^5 (magenta) and combined (black) datasets. The adopted prior distributions are included for reference as solid green lines.

Alexander, R. K., Vincenzo, F., Ji, A. P., et al. 2023, Monthly Notices of the Royal Astronomical Society, 522, 5415, doi: [10.1093/mnras/stad1312](https://doi.org/10.1093/mnras/stad1312)

Astropy Collaboration. 2013, Astronomy and Astrophysics, 558, A33, doi: [10.1051/0004-6361/201322068](https://doi.org/10.1051/0004-6361/201322068)

Astropy Collaboration, Price-Whelan, A. M., Sipőcz, B. M., et al. 2018, The Astronomical Journal, 156, 123, doi: [10.3847/1538-3881/aabc4f](https://doi.org/10.3847/1538-3881/aabc4f)

Astropy Collaboration, Price-Whelan, A. M., Lim, P. L., et al. 2022, The Astrophysical Journal, 935, 167, doi: [10.3847/1538-4357/ac7c74](https://doi.org/10.3847/1538-4357/ac7c74)

Awad, P., Li, T. S., Erkal, D., et al. 2025, Astronomy and Astrophysics, 693, A69, doi: [10.1051/0004-6361/202451930](https://doi.org/10.1051/0004-6361/202451930)

Barmantloo, S., & Cautun, M. 2023, Monthly Notices of the Royal Astronomical Society, 520, 1704, doi: [10.1093/mnras/stad222](https://doi.org/10.1093/mnras/stad222)

Battaglia, G., & Nipoti, C. 2022, Nature Astronomy, 6, 659, doi: [10.1038/s41550-022-01638-7](https://doi.org/10.1038/s41550-022-01638-7)

Battaglia, G., Taibi, S., Thomas, G. F., & Fritz, T. K. 2022, Astronomy and Astrophysics, 657, A54, doi: [10.1051/0004-6361/202141528](https://doi.org/10.1051/0004-6361/202141528)

Bechtol, K., Drlica-Wagner, A., Balbinot, E., et al. 2015, The Astrophysical Journal, 807, 50, doi: [10.1088/0004-637X/807/1/50](https://doi.org/10.1088/0004-637X/807/1/50)

Belokurov, V., Zucker, D. B., Evans, N. W., et al. 2006, The Astrophysical Journal, 647, L111, doi: [10.1086/507324](https://doi.org/10.1086/507324)

—. 2007, The Astrophysical Journal, 654, 897, doi: [10.1086/509718](https://doi.org/10.1086/509718)

Benítez-Llambay, A., Navarro, J. F., Abadi, M. G., et al. 2016, Monthly Notices of the Royal Astronomical Society, 456, 1185, doi: [10.1093/mnras/stv2722](https://doi.org/10.1093/mnras/stv2722)

Binney, J., & Tremaine, S. 2008, Galactic Dynamics: Second Edition

Bovy, J. 2015, The Astrophysical Journal Supplement Series, 216, 29, doi: [10.1088/0067-0049/216/2/29](https://doi.org/10.1088/0067-0049/216/2/29)

Brown, T. M., Tumlinson, J., Geha, M., et al. 2014, The Astrophysical Journal, 796, 91, doi: [10.1088/0004-637X/796/2/91](https://doi.org/10.1088/0004-637X/796/2/91)

Bullock, J. S., & Boylan-Kolchin, M. 2017, Annual Review of Astronomy and Astrophysics, 55, 343, doi: [10.1146/annurev-astro-091916-055313](https://doi.org/10.1146/annurev-astro-091916-055313)

Caldwell, N., Walker, M. G., Mateo, M., et al. 2017, The Astrophysical Journal, 839, 20, doi: [10.3847/1538-4357/aa688e](https://doi.org/10.3847/1538-4357/aa688e)

Cappellari, M. 2008, Monthly Notices of the Royal Astronomical Society, 390, 71, doi: [10.1111/j.1365-2966.2008.13754.x](https://doi.org/10.1111/j.1365-2966.2008.13754.x)

Cerny, W., Martínez-Vázquez, C. E., Drlica-Wagner, A., et al. 2023, The Astrophysical Journal, 953, 1, doi: [10.3847/1538-4357/acdd78](https://doi.org/10.3847/1538-4357/acdd78)

Chang, L. J., & Necib, L. 2021, Monthly Notices of the Royal Astronomical Society, 507, 4715, doi: [10.1093/mnras/stab2440](https://doi.org/10.1093/mnras/stab2440)

- Chisholm, J., Tremonti, C. A., Leitherer, C., & Chen, Y. 2017, *Monthly Notices of the Royal Astronomical Society*, 469, 4831, doi: [10.1093/mnras/stx1164](https://doi.org/10.1093/mnras/stx1164)
- Chiti, A., Frebel, A., Simon, J. D., et al. 2021, *Nature Astronomy*, 5, 392, doi: [10.1038/s41550-020-01285-w](https://doi.org/10.1038/s41550-020-01285-w)
- Chiti, A., Frebel, A., Ji, A. P., et al. 2023, *The Astronomical Journal*, 165, 55, doi: [10.3847/1538-3881/aca416](https://doi.org/10.3847/1538-3881/aca416)
- Clementini, G., Ripepi, V., Garofalo, A., et al. 2023, *Astronomy & Astrophysics*, Volume 674, id.A18, <NUMPAGES>42</NUMPAGES> pp., 674, A18, doi: [10.1051/0004-6361/202243964](https://doi.org/10.1051/0004-6361/202243964)
- Collins, M. L. M., Charles, E. J. E., Martínez-Delgado, D., et al. 2022, *Monthly Notices of the Royal Astronomical Society*, 515, L72, doi: [10.1093/mnrasl/slac063](https://doi.org/10.1093/mnrasl/slac063)
- Collins, M. L. M., & Read, J. I. 2022, *Nature Astronomy*, 6, 647, doi: [10.1038/s41550-022-01657-4](https://doi.org/10.1038/s41550-022-01657-4)
- Collins, M. L. M., Tollerud, E. J., Sand, D. J., et al. 2017, *Monthly Notices of the Royal Astronomical Society*, 467, 573, doi: [10.1093/mnras/stx067](https://doi.org/10.1093/mnras/stx067)
- Dall’Ora, M., Clementini, G., Kinemuchi, K., et al. 2006, *The Astrophysical Journal*, 653, L109, doi: [10.1086/510665](https://doi.org/10.1086/510665)
- De Leo, M., Read, J. I., Noël, N. E. D., et al. 2024, *Monthly Notices of the Royal Astronomical Society*, 535, 1015, doi: [10.1093/mnras/stae2428](https://doi.org/10.1093/mnras/stae2428)
- DESI Collaboration, Aguilar, J., Ahlen, S., et al. 2016, *arXiv e-prints*, arXiv:1611.00036
- Dey, A., Schlegel, D. J., Lang, D., et al. 2019, *The Astronomical Journal*, 157, 168, doi: [10.3847/1538-3881/ab089d](https://doi.org/10.3847/1538-3881/ab089d)
- Dotter, A. 2016, *The Astrophysical Journal Supplement Series*, 222, 8, doi: [10.3847/0067-0049/222/1/8](https://doi.org/10.3847/0067-0049/222/1/8)
- Drlica-Wagner, A., Carlin, J. L., Nidever, D. L., et al. 2021, *The Astrophysical Journal Supplement Series*, 256, 2, doi: [10.3847/1538-4365/ac079d](https://doi.org/10.3847/1538-4365/ac079d)
- Durbin, M. J., Choi, Y., Savino, A., et al. 2025, *The HST Legacy Archival Uniform Reduction of Local Group Imaging (LAURELIN). I. Photometry and Star Formation Histories for 36 Ultra-faint Dwarf Galaxies*, arXiv, doi: [10.48550/arXiv.2505.18252](https://doi.org/10.48550/arXiv.2505.18252)
- Dutton, A. A., & Macciò, A. V. 2014, *Monthly Notices of the Royal Astronomical Society*, 441, 3359, doi: [10.1093/mnras/stu742](https://doi.org/10.1093/mnras/stu742)
- Ebrov, I., & Lokas, E. L. 2017, *The Astrophysical Journal*, 850, 144, doi: [10.3847/1538-4357/aa96ff](https://doi.org/10.3847/1538-4357/aa96ff)
- Eggen, N. R., Scarlata, C., Skillman, E., & Jaskot, A. 2022, *Blow-Away in the Extreme Low-Mass Starburst Galaxy Pox~186*, arXiv, doi: [10.48550/arXiv.2207.02245](https://doi.org/10.48550/arXiv.2207.02245)
- Erkal, D., Belokurov, V., Laporte, C. F. P., et al. 2019, *Monthly Notices of the Royal Astronomical Society*, 487, 2685, doi: [10.1093/mnras/stz1371](https://doi.org/10.1093/mnras/stz1371)
- Escala, I., Wetzel, A., Kirby, E. N., et al. 2018, *Monthly Notices of the Royal Astronomical Society*, 474, 2194, doi: [10.1093/mnras/stx2858](https://doi.org/10.1093/mnras/stx2858)
- Feast, M. W., Thackeray, A. D., & Wesselink, A. J. 1961, *Monthly Notices of the Royal Astronomical Society*, 122, 433, doi: [10.1093/mnras/122.5.433](https://doi.org/10.1093/mnras/122.5.433)
- Filion, C., Kozhurina-Platais, V., Avila, R. J., Platais, I., & Wyse, R. F. G. 2020, *The Astrophysical Journal*, 901, 82, doi: [10.3847/1538-4357/abafb6](https://doi.org/10.3847/1538-4357/abafb6)
- Filion, C., Platais, I., Wyse, R. F. G., & Kozhurina-Platais, V. 2022, *The Astrophysical Journal*, 939, 38, doi: [10.3847/1538-4357/ac9383](https://doi.org/10.3847/1538-4357/ac9383)
- Fillingham, S. P. 2019, PhD thesis
- Foreman-Mackey, D. 2016, *Journal of Open Source Software*, 1, 24, doi: [10.21105/joss.00024](https://doi.org/10.21105/joss.00024)
- Foreman-Mackey, D., Hogg, D. W., Lang, D., & Goodman, J. 2013, *Publications of the Astronomical Society of the Pacific*, 125, 306, doi: [10.1086/670067](https://doi.org/10.1086/670067)
- Frebel, A., & Norris, J. E. 2015, *Annual Review of Astronomy and Astrophysics*, 53, 631, doi: [10.1146/annurev-astro-082214-122423](https://doi.org/10.1146/annurev-astro-082214-122423)
- Frebel, A., Norris, J. E., Gilmore, G., & Wyse, R. F. G. 2016, *The Astrophysical Journal*, 826, 110, doi: [10.3847/0004-637X/826/2/110](https://doi.org/10.3847/0004-637X/826/2/110)
- Frebel, A., Simon, J. D., Geha, M., & Willman, B. 2010, *The Astrophysical Journal*, 708, 560, doi: [10.1088/0004-637X/708/1/560](https://doi.org/10.1088/0004-637X/708/1/560)
- Fu, S. W., Weisz, D. R., Starkenburg, E., et al. 2024, *The Astrophysical Journal*, 975, 2, doi: [10.3847/1538-4357/ad76a2](https://doi.org/10.3847/1538-4357/ad76a2)
- Gaia Collaboration, Vallenari, A., Brown, A. G. A., et al. 2022, *Gaia Data Release 3: Summary of the Content and Survey Properties*
- Genina, A., Read, J. I., Frenk, C. S., et al. 2020, *Monthly Notices of the Royal Astronomical Society*, 498, 144, doi: [10.1093/mnras/staa2352](https://doi.org/10.1093/mnras/staa2352)
- Geringer-Sameth, A., Koushiappas, S. M., & Walker, M. 2015, *The Astrophysical Journal*, 801, 74, doi: [10.1088/0004-637X/801/2/74](https://doi.org/10.1088/0004-637X/801/2/74)
- Gilmore, G., Norris, J. E., Monaco, L., et al. 2013, *The Astrophysical Journal*, 763, 61, doi: [10.1088/0004-637X/763/1/61](https://doi.org/10.1088/0004-637X/763/1/61)
- Ginsburg, A., Sipocz, B. M., Brasseur, C. E., et al. 2019, *The Astronomical Journal*, 157, 98, doi: [10.3847/1538-3881/aafc33](https://doi.org/10.3847/1538-3881/aafc33)

- Griffith, E. J., Sukhbold, T., Weinberg, D. H., et al. 2021, *The Astrophysical Journal*, 921, 73, doi: [10.3847/1538-4357/ac1bac](https://doi.org/10.3847/1538-4357/ac1bac)
- Guerra, J., Geha, M., & Strigari, L. E. 2023, *The Astrophysical Journal*, 943, 121, doi: [10.3847/1538-4357/aca8a5](https://doi.org/10.3847/1538-4357/aca8a5)
- Harris, C. R., Millman, K. J., van der Walt, S. J., et al. 2020, *Nature*, 585, 357, doi: [10.1038/s41586-020-2649-2](https://doi.org/10.1038/s41586-020-2649-2)
- Hastings, W. K. 1970, *Biometrika*, 57, 97, doi: [10.1093/biomet/57.1.97](https://doi.org/10.1093/biomet/57.1.97)
- Hayashi, K., & Chiba, M. 2012, *The Astrophysical Journal*, 755, 145, doi: [10.1088/0004-637X/755/2/145](https://doi.org/10.1088/0004-637X/755/2/145)
- . 2015, *The Astrophysical Journal*, 810, 22, doi: [10.1088/0004-637X/810/1/22](https://doi.org/10.1088/0004-637X/810/1/22)
- Hayashi, K., Chiba, M., & Ishiyama, T. 2020, *The Astrophysical Journal*, 904, 45, doi: [10.3847/1538-4357/abbe0a](https://doi.org/10.3847/1538-4357/abbe0a)
- Hayashi, K., Ferreira, E. G. M., & Chan, H. Y. J. 2021a, *The Astrophysical Journal*, 912, L3, doi: [10.3847/2041-8213/abf501](https://doi.org/10.3847/2041-8213/abf501)
- Hayashi, K., Hirai, Y., Chiba, M., & Ishiyama, T. 2023, *The Astrophysical Journal*, 953, 185, doi: [10.3847/1538-4357/ace33e](https://doi.org/10.3847/1538-4357/ace33e)
- Hayashi, K., Ibe, M., Kobayashi, S., Nakayama, Y., & Shirai, S. 2021b, *Physical Review D*, 103, 023017, doi: [10.1103/PhysRevD.103.023017](https://doi.org/10.1103/PhysRevD.103.023017)
- Heckman, T. M., Alexandroff, R. M., Borthakur, S., Overzier, R., & Leitherer, C. 2015, *The Astrophysical Journal*, 809, 147, doi: [10.1088/0004-637X/809/2/147](https://doi.org/10.1088/0004-637X/809/2/147)
- Hernquist, L. 1990, *The Astrophysical Journal*, 356, 359, doi: [10.1086/168845](https://doi.org/10.1086/168845)
- Ho, N., Geha, M., Munoz, R. R., et al. 2012, *The Astrophysical Journal*, 758, 124, doi: [10.1088/0004-637X/758/2/124](https://doi.org/10.1088/0004-637X/758/2/124)
- Hopkins, P. F., Wetzel, A., Kereš, D., et al. 2018, *Monthly Notices of the Royal Astronomical Society*, 480, 800, doi: [10.1093/mnras/sty1690](https://doi.org/10.1093/mnras/sty1690)
- Horigome, S., Hayashi, K., & Ando, S. 2023, *Physical Review D*, 108, 083530, doi: [10.1103/PhysRevD.108.083530](https://doi.org/10.1103/PhysRevD.108.083530)
- Hubble, E. P. 1926, *The Astrophysical Journal*, 64, 321, doi: [10.1086/143018](https://doi.org/10.1086/143018)
- Hunter, J. D. 2007, *Computing in Science & Engineering*, 9, 90, doi: [10.1109/MCSE.2007.55](https://doi.org/10.1109/MCSE.2007.55)
- Husser, T. O., Wende-von Berg, S., Dreizler, S., et al. 2013, *Astronomy and Astrophysics*, 553, A6, doi: [10.1051/0004-6361/201219058](https://doi.org/10.1051/0004-6361/201219058)
- Ibata, R. A., McConnachie, A., Cuillandre, J.-C., et al. 2017, *The Astrophysical Journal*, 848, 128, doi: [10.3847/1538-4357/aa855c](https://doi.org/10.3847/1538-4357/aa855c)
- Ishigaki, M. N., Aoki, W., Arimoto, N., & Okamoto, S. 2014, *Astronomy and Astrophysics*, 562, A146, doi: [10.1051/0004-6361/201322796](https://doi.org/10.1051/0004-6361/201322796)
- Jenkins, S. A., Li, T. S., Pace, A. B., et al. 2021, *The Astrophysical Journal*, 920, 92, doi: [10.3847/1538-4357/ac1353](https://doi.org/10.3847/1538-4357/ac1353)
- Jensen, J., Hayes, C. R., Sestito, F., et al. 2024, *Monthly Notices of the Royal Astronomical Society*, 527, 4209, doi: [10.1093/mnras/stad3322](https://doi.org/10.1093/mnras/stad3322)
- Jethwa, P., Erkal, D., & Belokurov, V. 2016, *Monthly Notices of the Royal Astronomical Society*, 461, 2212, doi: [10.1093/mnras/stw1343](https://doi.org/10.1093/mnras/stw1343)
- Ji, A. P., Koposov, S. E., Li, T. S., et al. 2021, *The Astrophysical Journal*, 921, 32, doi: [10.3847/1538-4357/ac1869](https://doi.org/10.3847/1538-4357/ac1869)
- Johnson, J. W., Conroy, C., Johnson, B. D., et al. 2023, *Monthly Notices of the Royal Astronomical Society*, 526, 5084, doi: [10.1093/mnras/stad2985](https://doi.org/10.1093/mnras/stad2985)
- Kacharov, N., Battaglia, G., Rejkuba, M., et al. 2017, *Monthly Notices of the Royal Astronomical Society*, 466, 2006, doi: [10.1093/mnras/stw3188](https://doi.org/10.1093/mnras/stw3188)
- Kado-Fong, E., Geha, M., Mao, Y.-Y., et al. 2024, *The Astrophysical Journal*, 966, 129, doi: [10.3847/1538-4357/ad3042](https://doi.org/10.3847/1538-4357/ad3042)
- Kallivayalil, N., van der Marel, R. P., Besla, G., Anderson, J., & Alcock, C. 2013, *The Astrophysical Journal*, 764, 161, doi: [10.1088/0004-637X/764/2/161](https://doi.org/10.1088/0004-637X/764/2/161)
- Kaplinghat, M., & Strigari, L. E. 2008, *The Astrophysical Journal*, 682, L93, doi: [10.1086/591052](https://doi.org/10.1086/591052)
- Karamanis, M., Beutler, F., Peacock, J. A., Nabergoj, D., & Seljak, U. 2022a, *Monthly Notices of the Royal Astronomical Society*, 516, 1644, doi: [10.1093/mnras/stac2272](https://doi.org/10.1093/mnras/stac2272)
- Karamanis, M., Nabergoj, D., Beutler, F., Peacock, J., & Seljak, U. 2022b, *The Journal of Open Source Software*, 7, 4634, doi: [10.21105/joss.04634](https://doi.org/10.21105/joss.04634)
- Kazantzidis, S., Lokas, E. L., Callegari, S., Mayer, L., & Moustakas, L. A. 2011, *The Astrophysical Journal*, 726, 98, doi: [10.1088/0004-637X/726/2/98](https://doi.org/10.1088/0004-637X/726/2/98)
- King, I. 1962, *The Astronomical Journal*, 67, 471, doi: [10.1086/108756](https://doi.org/10.1086/108756)
- Kirby, E. N., Cohen, J. G., Guhathakurta, P., et al. 2013, *The Astrophysical Journal*, 779, 102, doi: [10.1088/0004-637X/779/2/102](https://doi.org/10.1088/0004-637X/779/2/102)
- Kirby, E. N., Lanfranchi, G. A., Simon, J. D., Cohen, J. G., & Guhathakurta, P. 2011, *The Astrophysical Journal*, 727, 78, doi: [10.1088/0004-637X/727/2/78](https://doi.org/10.1088/0004-637X/727/2/78)
- Koposov, S. E. 2019, *Astrophysics Source Code Library*, ascl:1907.013

- Koposov, S. E., Gilmore, G., Walker, M. G., et al. 2011, *The Astrophysical Journal*, 736, 146, doi: [10.1088/0004-637X/736/2/146](https://doi.org/10.1088/0004-637X/736/2/146)
- Koposov, S. E., Walker, M. G., Belokurov, V., et al. 2018, *Monthly Notices of the Royal Astronomical Society*, 479, 5343, doi: [10.1093/mnras/sty1772](https://doi.org/10.1093/mnras/sty1772)
- Koposov, S. E., Erkal, D., Li, T. S., et al. 2023, *Monthly Notices of the Royal Astronomical Society*, 521, 4936, doi: [10.1093/mnras/stad551](https://doi.org/10.1093/mnras/stad551)
- Kroupa, P. 2001, *Monthly Notices of the Royal Astronomical Society*, 322, 231, doi: [10.1046/j.1365-8711.2001.04022.x](https://doi.org/10.1046/j.1365-8711.2001.04022.x)
- Küpper, A. H. W., Johnston, K. V., Mieske, S., Collins, M. L. M., & Tollerud, E. J. 2017, *The Astrophysical Journal*, 834, 112, doi: [10.3847/1538-4357/834/2/112](https://doi.org/10.3847/1538-4357/834/2/112)
- Lacchin, E., Matteucci, F., Vincenzo, F., & Palla, M. 2020, *Monthly Notices of the Royal Astronomical Society*, 495, 3276, doi: [10.1093/mnras/staa585](https://doi.org/10.1093/mnras/staa585)
- Lai, D. K., Lee, Y. S., Bolte, M., et al. 2011, *The Astrophysical Journal*, 738, 51, doi: [10.1088/0004-637X/738/1/51](https://doi.org/10.1088/0004-637X/738/1/51)
- Lanfranchi, G. A., & Matteucci, F. 2004, *Monthly Notices of the Royal Astronomical Society*, 351, 1338, doi: [10.1111/j.1365-2966.2004.07877.x](https://doi.org/10.1111/j.1365-2966.2004.07877.x)
- . 2007, *Astronomy and Astrophysics*, 468, 927, doi: [10.1051/0004-6361:20066576](https://doi.org/10.1051/0004-6361:20066576)
- . 2010, *Astronomy and Astrophysics*, 512, A85, doi: [10.1051/0004-6361/200913045](https://doi.org/10.1051/0004-6361/200913045)
- Lanfranchi, G. A., Matteucci, F., & Cescutti, G. 2006, *Astronomy and Astrophysics*, 453, 67, doi: [10.1051/0004-6361:20054627](https://doi.org/10.1051/0004-6361:20054627)
- Lewis, I., Balogh, M., De Propriis, R., et al. 2002, *Monthly Notices of the Royal Astronomical Society*, 334, 673, doi: [10.1046/j.1365-8711.2002.05558.x](https://doi.org/10.1046/j.1365-8711.2002.05558.x)
- Li, H., Hammer, F., Babusiaux, C., et al. 2021, *The Astrophysical Journal*, 916, 8, doi: [10.3847/1538-4357/ac0436](https://doi.org/10.3847/1538-4357/ac0436)
- Li, T. S., Koposov, S. E., Zucker, D. B., et al. 2019, *Monthly Notices of the Royal Astronomical Society*, 490, 3508, doi: [10.1093/mnras/stz2731](https://doi.org/10.1093/mnras/stz2731)
- Li, T. S., Ji, A. P., Pace, A. B., et al. 2022, *The Astrophysical Journal*, 928, 30, doi: [10.3847/1538-4357/ac46d3](https://doi.org/10.3847/1538-4357/ac46d3)
- Limberg, G., Souza, S. O., Pérez-Villegas, A., et al. 2022, *The Astrophysical Journal*, 935, 109, doi: [10.3847/1538-4357/ac8159](https://doi.org/10.3847/1538-4357/ac8159)
- Lokas, E. L. 2002, *Monthly Notices of the Royal Astronomical Society*, 333, 697, doi: [10.1046/j.1365-8711.2002.05457.x](https://doi.org/10.1046/j.1365-8711.2002.05457.x)
- Longeard, N., Jablonka, P., Arentsen, A., et al. 2022, *Monthly Notices of the Royal Astronomical Society*, 516, 2348, doi: [10.1093/mnras/stac1827](https://doi.org/10.1093/mnras/stac1827)
- Maoz, D., Mannucci, F., & Brandt, T. D. 2012, *Monthly Notices of the Royal Astronomical Society*, 426, 3282, doi: [10.1111/j.1365-2966.2012.21871.x](https://doi.org/10.1111/j.1365-2966.2012.21871.x)
- Martin, N. F., Ibata, R. A., Chapman, S. C., Irwin, M., & Lewis, G. F. 2007, *Monthly Notices of the Royal Astronomical Society*, 380, 281, doi: [10.1111/j.1365-2966.2007.12055.x](https://doi.org/10.1111/j.1365-2966.2007.12055.x)
- Martin, N. F., & Jin, S. 2010, *The Astrophysical Journal*, 721, 1333, doi: [10.1088/0004-637X/721/2/1333](https://doi.org/10.1088/0004-637X/721/2/1333)
- Martinez, G. D., Minor, Q. E., Bullock, J., et al. 2011, *The Astrophysical Journal*, 738, 55, doi: [10.1088/0004-637X/738/1/55](https://doi.org/10.1088/0004-637X/738/1/55)
- Martínez-García, A. M., del Pino, A., Aparicio, A., van der Marel, R. P., & Watkins, L. L. 2021, *Monthly Notices of the Royal Astronomical Society*, 505, 5884, doi: [10.1093/mnras/stab1568](https://doi.org/10.1093/mnras/stab1568)
- Mayer, L., Governato, F., Colpi, M., et al. 2001, *The Astrophysical Journal*, 559, 754, doi: [10.1086/322356](https://doi.org/10.1086/322356)
- McConnachie, A. W., & Venn, K. A. 2020, *Research Notes of the American Astronomical Society*, 4, 229, doi: [10.3847/2515-5172/abd18b](https://doi.org/10.3847/2515-5172/abd18b)
- McKinney, W. 2010, in *Proceedings of the 9th Python in Science Conference*, ed. S. van der Walt & J. Millman, 56–61, doi: [10.25080/Majora-92bf1922-00a](https://doi.org/10.25080/Majora-92bf1922-00a)
- McQuinn, Kristen. B. W., van Zee, L., & Skillman, E. D. 2019, *The Astrophysical Journal*, 886, 74, doi: [10.3847/1538-4357/ab4c37](https://doi.org/10.3847/1538-4357/ab4c37)
- Mercado, F. J., Bullock, J. S., Boylan-Kolchin, M., et al. 2021, *Monthly Notices of the Royal Astronomical Society*, 501, 5121, doi: [10.1093/mnras/staa3958](https://doi.org/10.1093/mnras/staa3958)
- Metropolis, N., Rosenbluth, A. W., Rosenbluth, M. N., Teller, A. H., & Teller, E. 1953, *Journal of Chemical Physics*, 21, 1087, doi: [10.1063/1.1699114](https://doi.org/10.1063/1.1699114)
- Miszalski, B., Shortridge, K., Saunders, W., Parker, Q. A., & Croom, S. M. 2006, *Monthly Notices of the Royal Astronomical Society*, 371, 1537, doi: [10.1111/j.1365-2966.2006.10777.x](https://doi.org/10.1111/j.1365-2966.2006.10777.x)
- Miyoshi, T., & Chiba, M. 2020, *The Astrophysical Journal*, 905, 109, doi: [10.3847/1538-4357/abc486](https://doi.org/10.3847/1538-4357/abc486)
- Moore, B., Kazantzidis, S., Diemand, J., & Stadel, J. 2004, *Monthly Notices of the Royal Astronomical Society*, 354, 522, doi: [10.1111/j.1365-2966.2004.08211.x](https://doi.org/10.1111/j.1365-2966.2004.08211.x)
- Muñoz, R. R., Carlin, J. L., Frinchaboy, P. M., et al. 2006, *The Astrophysical Journal*, 650, L51, doi: [10.1086/508685](https://doi.org/10.1086/508685)
- Muñoz, R. R., Côté, P., Santana, F. A., et al. 2018, *The Astrophysical Journal*, 860, 66, doi: [10.3847/1538-4357/aac16b](https://doi.org/10.3847/1538-4357/aac16b)

- Muñoz, R. R., Majewski, S. R., & Johnston, K. V. 2008, *The Astrophysical Journal*, 679, 346, doi: [10.1086/587125](https://doi.org/10.1086/587125)
- Nguyen, T., Read, J., Necib, L., et al. 2025, *Trial by FIRE: Probing the Dark Matter Density Profile of Dwarf Galaxies with GraphNPE*, arXiv, doi: [10.48550/arXiv.2503.03812](https://doi.org/10.48550/arXiv.2503.03812)
- Norris, J. E., Gilmore, G., Wyse, R. F. G., et al. 2008, *The Astrophysical Journal Letters*, 689, L113, doi: [10.1086/595962](https://doi.org/10.1086/595962)
- Norris, J. E., Wyse, R. F. G., Gilmore, G., et al. 2010a, *The Astrophysical Journal*, Volume 723, Issue 2, pp. 1632-1650 (2010), 723, 1632, doi: [10.1088/0004-637X/723/2/1632](https://doi.org/10.1088/0004-637X/723/2/1632)
- Norris, J. E., Yong, D., Gilmore, G., & Wyse, R. F. G. 2010b, *The Astrophysical Journal*, 711, 350, doi: [10.1088/0004-637X/711/1/350](https://doi.org/10.1088/0004-637X/711/1/350)
- Okamoto, S., Arimoto, N., Yamada, Y., & Onodera, M. 2012, *The Astrophysical Journal*, 744, 96, doi: [10.1088/0004-637X/744/2/96](https://doi.org/10.1088/0004-637X/744/2/96)
- Ou, X., Chiti, A., Shipp, N., et al. 2024, *The Astrophysical Journal*, 966, 33, doi: [10.3847/1538-4357/ad2f27](https://doi.org/10.3847/1538-4357/ad2f27)
- Pace, A. B. 2024, *The Local Volume Database: A Library of the Observed Properties of Nearby Dwarf Galaxies and Star Clusters*, arXiv, doi: [10.48550/arXiv.2411.07424](https://doi.org/10.48550/arXiv.2411.07424)
- Pace, A. B., Erkal, D., & Li, T. S. 2022, *The Astrophysical Journal*, 940, 136, doi: [10.3847/1538-4357/ac997b](https://doi.org/10.3847/1538-4357/ac997b)
- Pace, A. B., Martinez, G. D., Kaplinghat, M., & Muñoz, R. R. 2014, *Monthly Notices of the Royal Astronomical Society*, 442, 1718, doi: [10.1093/mnras/stu938](https://doi.org/10.1093/mnras/stu938)
- Pace, A. B., & Strigari, L. E. 2019, *Monthly Notices of the Royal Astronomical Society*, 482, 3480, doi: [10.1093/mnras/sty2839](https://doi.org/10.1093/mnras/sty2839)
- Pace, A. B., Kaplinghat, M., Kirby, E., et al. 2020, *Monthly Notices of the Royal Astronomical Society*, 495, 3022, doi: [10.1093/mnras/staa1419](https://doi.org/10.1093/mnras/staa1419)
- Pace, A. B., Li, T. S., Ji, A. P., et al. 2025, *Spectroscopic Analysis of Pictor II: A Very Low Metallicity Ultra-Faint Dwarf Galaxy Bound to the Large Magellanic Cloud*, arXiv, doi: [10.48550/arXiv.2506.21841](https://doi.org/10.48550/arXiv.2506.21841)
- Pan, Y., Chiti, A., Drlica-Wagner, A., et al. 2025, *The Astrophysical Journal*, 978, 39, doi: [10.3847/1538-4357/ad9820](https://doi.org/10.3847/1538-4357/ad9820)
- Pandya, V., Fielding, D. B., Anglés-Alcázar, D., et al. 2021, *Monthly Notices of the Royal Astronomical Society*, 508, 2979, doi: [10.1093/mnras/stab2714](https://doi.org/10.1093/mnras/stab2714)
- Peñarrubia, J., Navarro, J. F., & McConnachie, A. W. 2008, *The Astrophysical Journal*, 673, 226, doi: [10.1086/523686](https://doi.org/10.1086/523686)
- Pietrzyński, G., Graczyk, D., Gallenne, A., et al. 2019, *Nature*, 567, 200, doi: [10.1038/s41586-019-0999-4](https://doi.org/10.1038/s41586-019-0999-4)
- Planck Collaboration, Aghanim, N., Akrami, Y., et al. 2020, *Astronomy and Astrophysics*, 641, A6, doi: [10.1051/0004-6361/201833910](https://doi.org/10.1051/0004-6361/201833910)
- Plummer, H. C. 1911, *Monthly Notices of the Royal Astronomical Society*, 71, 460, doi: [10.1093/mnras/71.5.460](https://doi.org/10.1093/mnras/71.5.460)
- Pontzen, A., & Governato, F. 2014, *Nature*, 506, 171, doi: [10.1038/nature12953](https://doi.org/10.1038/nature12953)
- Price-Whelan, A. M., Hogg, D. W., Foreman-Mackey, D., & Rix, H.-W. 2017, *The Astrophysical Journal*, 837, 20, doi: [10.3847/1538-4357/aa5e50](https://doi.org/10.3847/1538-4357/aa5e50)
- Read, J. I., Walker, M. G., & Steger, P. 2018, *Monthly Notices of the Royal Astronomical Society*, 481, 860, doi: [10.1093/mnras/sty2286](https://doi.org/10.1093/mnras/sty2286)
- Read, J. I., Wilkinson, M. I., Evans, N. W., Gilmore, G., & Kleyna, J. T. 2006, *Monthly Notices of the Royal Astronomical Society*, 367, 387, doi: [10.1111/j.1365-2966.2005.09959.x](https://doi.org/10.1111/j.1365-2966.2005.09959.x)
- Read, J. I., Mamon, G. A., Vasiliev, E., et al. 2021, *Monthly Notices of the Royal Astronomical Society*, 501, 978, doi: [10.1093/mnras/staa3663](https://doi.org/10.1093/mnras/staa3663)
- Revaz, Y., & Jablonka, P. 2018, *Astronomy and Astrophysics*, 616, A96, doi: [10.1051/0004-6361/201832669](https://doi.org/10.1051/0004-6361/201832669)
- Rocha, M., Peter, A. H. G., & Bullock, J. 2012, *Monthly Notices of the Royal Astronomical Society*, 425, 231, doi: [10.1111/j.1365-2966.2012.21432.x](https://doi.org/10.1111/j.1365-2966.2012.21432.x)
- Roderick, T. A., Jerjen, H., Da Costa, G. S., & Mackey, A. D. 2016, *Monthly Notices of the Royal Astronomical Society*, 460, 30, doi: [10.1093/mnras/stw949](https://doi.org/10.1093/mnras/stw949)
- Romano, D., Bellazzini, M., Starkenburg, E., & Leaman, R. 2015, *Monthly Notices of the Royal Astronomical Society*, 446, 4220, doi: [10.1093/mnras/stu2427](https://doi.org/10.1093/mnras/stu2427)
- Romano, D., Calura, F., D’Ercole, A., & Few, C. G. 2019, *Astronomy and Astrophysics*, 630, A140, doi: [10.1051/0004-6361/201935328](https://doi.org/10.1051/0004-6361/201935328)
- Rossi, M., Salvadori, S., Skúladóttir, Á., Vanni, I., & Koutsouridou, I. 2024, *Hidden Population III Descendants in Ultra-Faint Dwarf Galaxies*, arXiv, doi: [10.48550/arXiv.2406.12960](https://doi.org/10.48550/arXiv.2406.12960)
- Sandford, N. R., Weinberg, D. H., Weisz, D. R., & Fu, S. W. 2024, *Monthly Notices of the Royal Astronomical Society*, 530, 2315, doi: [10.1093/mnras/stae1010](https://doi.org/10.1093/mnras/stae1010)
- Schroyen, J., De Rijcke, S., Koleva, M., Cloet-Osselaer, A., & Vandenbroucke, B. 2013, *Monthly Notices of the Royal Astronomical Society*, 434, 888, doi: [10.1093/mnras/stt1084](https://doi.org/10.1093/mnras/stt1084)

- Sharp, R., Saunders, W., Smith, G., et al. 2006, in *Ground-Based and Airborne Instrumentation for Astronomy*, Vol. 6269 (SPIE), 152–164, doi: [10.1117/12.671022](https://doi.org/10.1117/12.671022)
- Shipp, N., Erkal, D., Drlica-Wagner, A., et al. 2021, *The Astrophysical Journal*, 923, 149, doi: [10.3847/1538-4357/ac2e93](https://doi.org/10.3847/1538-4357/ac2e93)
- Simon, J. D. 2019, *Annual Review of Astronomy and Astrophysics*, 57, 375, doi: [10.1146/annurev-astro-091918-104453](https://doi.org/10.1146/annurev-astro-091918-104453)
- Simon, J. D., & Geha, M. 2007, *The Astrophysical Journal*, 670, 313, doi: [10.1086/521816](https://doi.org/10.1086/521816)
- Smith, R., Fellhauer, M., Candlish, G. N., et al. 2013, *Monthly Notices of the Royal Astronomical Society*, 433, 2529, doi: [10.1093/mnras/stt925](https://doi.org/10.1093/mnras/stt925)
- Smith, S. E. T., Jensen, J., Roediger, J., et al. 2023, *The Astronomical Journal*, 166, 76, doi: [10.3847/1538-3881/acdd77](https://doi.org/10.3847/1538-3881/acdd77)
- Spencer, M. E., Mateo, M., Olszewski, E. W., et al. 2018, *The Astronomical Journal*, 156, 257, doi: [10.3847/1538-3881/aae3e4](https://doi.org/10.3847/1538-3881/aae3e4)
- Spencer, M. E., Mateo, M., Walker, M. G., et al. 2017, *The Astronomical Journal*, 153, 254, doi: [10.3847/1538-3881/aa6d51](https://doi.org/10.3847/1538-3881/aa6d51)
- Springel, V. 2005, *Monthly Notices of the Royal Astronomical Society*, 364, 1105, doi: [10.1111/j.1365-2966.2005.09655.x](https://doi.org/10.1111/j.1365-2966.2005.09655.x)
- Taibi, S., Battaglia, G., Leaman, R., et al. 2022, *Astronomy and Astrophysics*, 665, A92, doi: [10.1051/0004-6361/202243508](https://doi.org/10.1051/0004-6361/202243508)
- Takada, M., Ellis, R. S., Chiba, M., et al. 2014, *Publications of the Astronomical Society of Japan*, 66, R1, doi: [10.1093/pasj/pst019](https://doi.org/10.1093/pasj/pst019)
- Tarumi, Y., Yoshida, N., & Frebel, A. 2021, *The Astrophysical Journal*, 914, L10, doi: [10.3847/2041-8213/ac024e](https://doi.org/10.3847/2041-8213/ac024e)
- Tau, E. A., Vivas, A. K., & Martínez-Vázquez, C. E. 2024, *The Astronomical Journal*, 167, 57, doi: [10.3847/1538-3881/ad1509](https://doi.org/10.3847/1538-3881/ad1509)
- Team, T. P. D. 2024, *Pandas-Dev/Pandas: Pandas*, Zenodo, doi: [10.5281/zenodo.10957263](https://doi.org/10.5281/zenodo.10957263)
- van der Marel, R. P., Alves, D. R., Hardy, E., & Suntzeff, N. B. 2002, *The Astronomical Journal*, 124, 2639, doi: [10.1086/343775](https://doi.org/10.1086/343775)
- van der Marel, R. P., & Kallivayalil, N. 2014, *The Astrophysical Journal*, 781, 121, doi: [10.1088/0004-637X/781/2/121](https://doi.org/10.1088/0004-637X/781/2/121)
- Vasiliev, E. 2019, *Monthly Notices of the Royal Astronomical Society*, 482, 1525, doi: [10.1093/mnras/sty2672](https://doi.org/10.1093/mnras/sty2672)
- Vasiliev, E., Belokurov, V., & Erkal, D. 2021, *Monthly Notices of the Royal Astronomical Society*, 501, 2279, doi: [10.1093/mnras/staa3673](https://doi.org/10.1093/mnras/staa3673)
- Vincenzo, F., Matteucci, F., Vattakunnel, S., & Lanfranchi, G. A. 2014, *Monthly Notices of the Royal Astronomical Society*, 441, 2815, doi: [10.1093/mnras/stu710](https://doi.org/10.1093/mnras/stu710)
- Virtanen, P., Gommers, R., Oliphant, T. E., et al. 2020, *Nature Methods*, 17, 261, doi: [10.1038/s41592-019-0686-2](https://doi.org/10.1038/s41592-019-0686-2)
- Vivas, A. K., Martínez-Vázquez, C., & Walker, A. R. 2020, *The Astrophysical Journal Supplement Series*, 247, 35, doi: [10.3847/1538-4365/ab67c0](https://doi.org/10.3847/1538-4365/ab67c0)
- Walker, M. G., Caldwell, N., Mateo, M., et al. 2023, *The Astrophysical Journal Supplement Series*, 268, 19, doi: [10.3847/1538-4365/acdd79](https://doi.org/10.3847/1538-4365/acdd79)
- Walker, M. G., Mateo, M., & Olszewski, E. W. 2008, *The Astrophysical Journal*, 688, L75, doi: [10.1086/595586](https://doi.org/10.1086/595586)
- Walker, M. G., & Peñarrubia, J. 2011, *The Astrophysical Journal*, 742, 20, doi: [10.1088/0004-637X/742/1/20](https://doi.org/10.1088/0004-637X/742/1/20)
- Walker, M. G., Mateo, M., Olszewski, E. W., et al. 2016, *The Astrophysical Journal*, 819, 53, doi: [10.3847/0004-637X/819/1/53](https://doi.org/10.3847/0004-637X/819/1/53)
- Waller, F., Venn, K. A., Sestito, F., et al. 2023, *Monthly Notices of the Royal Astronomical Society*, 519, 1349, doi: [10.1093/mnras/stac3563](https://doi.org/10.1093/mnras/stac3563)
- Webster, D., Bland-Hawthorn, J., & Sutherland, R. 2015, *The Astrophysical Journal*, 799, L21, doi: [10.1088/2041-8205/799/2/L21](https://doi.org/10.1088/2041-8205/799/2/L21)
- Weinberg, D. H., Andrews, B. H., & Freudenburg, J. 2017, *The Astrophysical Journal*, 837, 183, doi: [10.3847/1538-4357/837/2/183](https://doi.org/10.3847/1538-4357/837/2/183)
- Weinberg, D. H., Griffith, E. J., Johnson, J. W., & Thompson, T. A. 2023, *The Scale of Stellar Yields: Implications of the Measured Mean Iron Yield of Core Collapse Supernovae*, doi: [10.48550/arXiv.2309.05719](https://doi.org/10.48550/arXiv.2309.05719)
- Yang, Y., Lewis, G. F., Erkal, D., et al. 2025, *The Astrophysical Journal*, 984, 189, doi: [10.3847/1538-4357/adc57c](https://doi.org/10.3847/1538-4357/adc57c)
- York, D. G., Adelman, J., Anderson, Jr., J. E., et al. 2000, *The Astronomical Journal*, 120, 1579, doi: [10.1086/301513](https://doi.org/10.1086/301513)
- Zhao, H. 1996, *Monthly Notices of the Royal Astronomical Society*, 278, 488, doi: [10.1093/mnras/278.2.488](https://doi.org/10.1093/mnras/278.2.488)